Université catholique de Louvain

faculté des sciences, école de physique
earth and life institute
georges lemaître centre for earth and climate research

Van Allen radiation belts dynamics revealed from PROBA-V/EPT observations

Graciela López Rosson

A thesis submitted to the Université catholique de Louvain in partial fulfillment of the requirements for the degree of Doctor in Science.

Examination committee:

Prof. Viviane Pierrard (Supervisor)	UCL/BIRA-IASB
Prof. Véronique Dehant (Supervisor)	UCL/ROB
Prof. Marie-Laurence De Keersmaecker (Chair)	UCL
Prof. Hugues Goosse (Secretary)	UCL
Dr. Sylvie Benck	UCL
Prof. Iannis Dandouras	IRAP, France
Dr. Fabien Darrouzet	BIRA-IASB
Dr. Johan De Keyser	BIRA-IASB
Prof. Rony Keppens	KULeuven

October 2018
Louvain la Neuve – Belgium

"Remember to look up at the stars and not down at your feet. Try to make sense of what you see and wonder about what makes the Universe exist. Be curious. And however difficult life may seem, there is always something you can do and succeed at. It matters that you don't just give up "

– Stephen Hawking

Preface

Now more than ever before, our society is extremely dependent on all kinds of satellite systems. Telecommunications, GPS, weather forecasting, research-oriented observations of geophysical parameters can be listed among our most important satellite applications. However, they are all inherently exposed to geomagnetic phenomena induced by fluctuations of the solar activity. Geomagnetic storms and the entrapment of any particle species in the magnetosphere can have consequences as serious as power-line breakdowns or radio communication disruptions, not to mention the direct hazard these particles represent for human activities in space.

Van Allen radiation belts –toroidal structures populated of energetic particles trapped in the Earth's magnetic field –have been studied extensively since their discovery, in the late 1950's. The sources from which particles in the distinct regions of these belts originate are manifold and the physical processes driving their dynamics are complex. Even so, despite of the theoretical knowledge accumulated over time, or even the very recent Van Allen Probes mission specifically designed to study the radiation belts, important uncertainties remain on the physics-based mechanisms underpinning both the temporal and spatial evolution of the distributions of trapped energetic particles. More specifically, the sensitivity of particle distributions in the belt to changes in geomagnetic conditions, such as storms or SEP events, are still not fully understood.

This context constitutes the crux of the motivation for the present thesis, which provides a comprehensive review of the theoretical bases behind radiation belt dynamics beforehand, subse-

quently addressing a few of the aforementioned physical uncertainties. Through the study of a new satellite observation dataset, this work shows specifically how geomagnetic conditions affect the particle fluxes and especially reveals more accurate insight in assessing the presence of high energy electrons in the inner belt, a still-open question in this field of research. As such, this thesis tackles these issues and represents a contribution towards both consolidating the theory behind trapped particles in the Earth magnetic field and improving our current space weather forecast capabilities, ultimately vital for all satellite-reliant human activities.

Acknowledgments

It has been a long journey to get here (I even had to cross the ocean!), thus I've met lots of incredible people who I should thank...

I wish to express my sincere thanks to everyone I came in contact with, during the last five years, and one way or another helped me, having a positive impact on the work presented here.

Foremost, I wish to thank my advisor prof. Viviane Pierrard for giving me the opportunity to work with her at the Belgian Institute of Space Aeronomy. Thank you for your support, guidance and help during all these years. I must acknowledge too all the jury members for their useful remarks that helped to improve this manuscript.

I had the luck to work at IASB-BIRA, where I met wonderful people who made it a pleasure to go to work. First, I have to mention Kris, who introduced me to IDL and radiation belts research. Without his help, my hours debugging IDL would have been certainly worse. I'm indebted to the IT group, specially Fred (who could help even when I was at the other side of the planet!), and Vincent L. for all his patience and assistance every time I needed a hand.

I spent the last months as a teaching assistant at UCL. Je dois remercier à mes collègues du Mercator, spécialement Sylvain, et Monique pour sa gentillesse et pour m'avoir aidée chaque fois que j'en ai eu besoin. C'est là où j'ai rencontré Oli, qui est devenu plus qu'un collègue mais un ami. Oli "oli", on en a déjà discuté et tu sais que je n'ai pas les mots pour te remercier... Sans ton aide, la fin de thèse aurait été presque impossible.

The warmest thank to my friends, who helped to stay sane, and

to never give up. Most importantly Ward, for his unconditional support the last years. Last but not least, my family. They have always been the pillar that supported me. Vicente, por toda tu paciencia cada vez que no tuve el tiempo para estar a tu lado (por culpa del trabajo), y tu espontánea sonrisa que me subió el ánimo incontables veces. Pato, gracias por tus palabras y haber estado allí cada vez que lo necesité. Finalmente mis padres, que siempre me han apoyado e insistido en la importancia de seguir mis sueños, aunque eso me llevara a estar lejos de ellos. I cannot forget Rayo and Spotty, who loyally stayed next to me even during late hours when I was finishing my manuscript.

Contents

1 Introduction **1**
1.1 Magnetosphere 1
1.1.1 Geomagnetic storms 3
1.1.2 Solar Energetic Particle (SEP) events . . . 5
1.2 Space Weather 5
1.3 Trapped particles motion 7
1.3.1 Gyration 7
1.3.2 Bounce 9
1.3.3 Drift 10
1.3.4 Adiabatic Invariants 14
1.4 Coordinates system 18
1.5 Van Allen radiation belts 21
1.5.1 History 21
1.5.2 Structure 21
1.5.3 The South Atlantic Anomaly (SAA) 23
1.6 Physical processes in the radiation belts 24
1.6.1 Inner belt 25
1.6.2 Outer belt 26
1.7 Proba-V satellite and operations 30
1.8 Energetic Particle Telescope (EPT) 31
1.9 Satellites 33
1.10 Models 36
1.11 Motivation to study the radiation belts 37

2 First results **39**
2.1 Introduction 39
2.2 Electrons 41
2.2.1 Spectra 51
2.3 Protons 52
2.4 Helium ions 60
2.5 Discussion and conclusions 62

3 Geomagnetic Storms **67**
3.1 Introduction 67
3.2 Data and analysis of the observations 68
3.2.1 The 17 March 2015 event 68
3.2.2 Electrons 70
3.2.3 Electron spectra 77
3.2.4 World maps 79
3.2.5 Protons 83
3.2.6 5 years of EPT observations 85
3.3 L parameter and the plasmapause 86
3.4 Conclusions 95

4 Particle spectra in the SAA **97**
4.1 Introduction 97
4.2 Spectra in different bins 98
4.3 Electron spectra 101
4.4 Proton spectra 109
4.5 Temporal variations 117
4.6 Conclusions 121

5 Conclusion and Perspectives **125**

A Relativistic particles motion **129**

Bibliography **132**

List of Figures

1.1 The Earth's magnetosphere diagram (modified from Kivelson and Russell (1995)) 2
1.2 Example of a large geomagnetic storm (starting on 20 June 2015) represented as Dst variation. 4
1.3 Space weather effects (Credits: NASA). 6
1.4 Three components of the motion of a charged particle in a magnetic field: gyration, bounce and drift (adapted from Hess (1968)) 8
1.5 Gyration motion (on top) and drift in different types of fields, where the magnetic field $\vec{B}$ is upward through the paper, and **Eq.** indicates the equation that describes the motion. Ions are shown in red and electrons in blue (adapted from Kallenrode (2001)). . . 11
1.6 Curvature drift, where $\vec{F}_{cf}$ is the centrifugal force acting on the particle, and R_c is the curvature radius. 14
1.7 Dipolar magnetic field lines of the Earth. For a particle located at point X, the different variables are: L (in Earth radii) is the magnetic-drift shell, λ is the magnetic latitude, θ is the colatitude, R is the radial distance to the X point on the field line, r_0 is the distance to the equatorial crossing of the field line and Λ represents the invariant latitude (adapted from Kivelson and Russell (1995)). From here, it is clear that $\lambda = \Lambda$ for a particle located at the surface of the Earth. 19

1.8 Artist conception of the Van Allen radiation belts (Credits: NASA/T. Benesch, J. Carns). 22
1.9 Detailed view of the radiation belts, showing the inner and outer belts, the South Atlantic Anomaly and L-shells (taken from Fennelly et al. (2015)). The blue lines represents the rotational axis of the Earth while the yellow one is the dipole axis. 23
1.10 CRAND mechanism (Hess (1968)) 25
1.11 Possible explanation of the outer belt dynamics by Horne (2007): 1. Radial diffusion and substorms inject medium-energy electrons from a reservoir in the outer region and excite plasma wave instabilities. 2. Gyro-resonant wave–particle interactions accelerate a fraction of the electrons to relativistic energies (MeV). Acceleration is most efficient in regions of low density. 3. Radial diffusion re-distributes relativistic electrons to fill up the entire outer radiation belt. . 27
1.12 Spatial distribution of waves in the inner magnetosphere, in relation to the plasmasphere and the drift-paths of ring-current (10–100 keV) electrons and ions and relativistic ($\geqslant$ 0.3 MeV) electrons (Thorne, 2010). 28
1.13 Satellite PROBA-V, showing the position of the EPT instrument. 30
1.14 Upper panel: Sketch of the Energetic Particle telescope. Bottom panel: cross section of the instrument showing the S1, S2 and S3 detectors. The HES or High Energy Section is defined by 10 DAM (Digital and Absorber Module) detectors (Cyamukungu et al., 2014). 32
1.15 Virtual channels and energy ranges for electrons, protons and Helium ions. 34

2.1 Data collected during 6 July 2013 along the PROBA-V LEO orbit at 820 km. The electron flux in channel 1 (0.5-0.6 MeV) is color-coded. 41

2.2 Electron flux in channel 1 (0.5-0.6 MeV) over one month of observations. Top panel: June 2013. Here it is possible to see the South Atlantic Anomaly (SAA), as well as the penetration of the outer belt at high latitudes or the so-called 'horns'. Bottom panel: July 2013. The fluxes are higher in June because this month was more geomagnetically active (one SEP and two geomagnetic storms with Dst $< -100\ nT$) than July (only one storm, Dst=-87 nT). 43
2.3 AE8-max world map at 820 km for > 0.5 MeV electrons. It is possible to clearly distinguish the north and south horn, and the SAA as well. 44
2.4 Electron flux measured by EPT in channel 5 (1-2.4 MeV) during one month of observations. Top panel: June 2013. Bottom panel: July 2013 45
2.5 EPT electron fluxes from 21 May 2013 up to 15 January 2014 as function of McIlwain L parameter (vertical axis) and time (horizontal axis) for channel 1 (upper panel) and channel 3 (middle panel) using the same color scale. Dst (Disturbed Storm Time) index measured for the same time period is given in the lower panel. Red dots and triangles in the upper panel represent the dates of the SEP events occurred during this period. 46
2.6 Electron fluxes at 600 keV (upper panel) and 742.5 keV (middle panel) in function of L and time from MagEIS observations, from 21 May 2013 to 15 January 2014. Lower panel shows the Dst index for the same time period. 49
2.7 GOES15/MAGED (telescope 1) in situ observations for electrons at E=475 keV (red) compared with EPT electrons in channel 1 (0.5-0.6 MeV, in black), for the same time period between $L = 6.5$ and $L = 7$. . . . 50
2.8 Electron spectra during June 2013 for three different locations: South Atlantic Anomaly (black), North horn (red) and South horn (green). 52

2.9 Proton fluxes measured in channel 1 (9.5-13 MeV) along the orbit of PROBA-V satellite on 23 May 2013 during the SEP event that started the 22 May 2013. 53

2.10 Proton flux in channel 1 (9.5–13 MeV) observed during one month of observations. Upper panel: June 2013, lower panel: September 2013 55

2.11 POES proton flux for energies higher than 16 MeV from 20 May 2013 up to 31 January 2014 (S. Bourdarie, private communication). 56

2.12 Proton flux from POES during January 2002 for E> 16 MeV. 57

2.13 Proton flux in channel 4 (61-92 MeV) observed during the month of June 2013, only with pitch angles between 80° and 100°. 58

2.14 Proton fluxes observed from 21 May 2013 up to 15 January 2014, as a function of L (vertical axis) and time (horizontal axis) for channel 1 corresponding to 9.5-13 MeV (first panel) and channel 3 corresponding to 29-61 MeV (second panel). Note that different color scales are used for both panels. 61

2.15 Helium fluxes observed in channel 1 (38-51 MeV) when accumulated from 16 May to 21 October 2013. 62

2.16 Helium fluxes observed from 21 May 2013 to 15 January 2014 as a function of time (horizontal axis) and L (vertical axis) for channel 1. 63

3.1 Solar wind parameters measured by ACE. From bottom to top: Bz (the z component of IMF in nT), N or the solar wind density, solar wind pressure in nPa, bulk velocity u in $km\ s^{-1}$ and geomagnetic activity indices (respectively Kp and Dst in nT) observed between January to June 2015. 69

3.2 GOES13 proton flux for different energies (data from `https://www.solarmonitor.org/`). The threshold for being considered as an SEP events is 10 protons per $[cm^2 s\ sr]$ for energies higher than 10 MeV. This is why the event was not considered as such, but it is clear that it almost reached the limit. 71

3.3 Electron fluxes observed by PROBA-V/EPT in channel 1 (0.5–0.6 MeV) as a function of McIlwain L between 28 February and 13 April 2015. 72

3.4 Electron fluxes observed by PROBA-V/EPT in channel 1 (0.5–0.6 MeV), in bin $4.6 < L < 4.8$; $0.25 < B < 0.3$G as a function of time between 1 and 31 March 2015. A dropout is clearly visible during the main phase of the 17 March storm. 73

3.5 Electron fluxes observed by PROBA-V/EPT in channel 5 (1-2.4 MeV) as a function of L between 28 February and 13 April 2015. 74

3.6 EPT electron fluxes in channel 6 (2.4–8 MeV) as a function of L between 28 February and 13 April 2015, and Dst index for the same time period. 75

3.7 Corrected electron fluxes observed in channel 742.5 keV of Van Allen Probe/MagEIS as a function of L between 28 February and 31 March 2015. 76

3.8 Spectra for two different (L, B) bins observed by EPT on 16, 17 and 18 March 2015, corresponding respectively to the day before, during and after the storm. The upper panel shows the bin $L = 5.2-5.4$, $B = 0.2-0.25$. The lowest fluxes are observed during the storm, but for the 3 days, the spectra shape is the same. The bottom panel shows the bin $L = 4.0-4.2$, $B = 0.2 - 0.25$. For this bin, 17 March has also the lowest fluxes, but only the energies > 0.8 MeV show a dropout. 78

3.9 Map of the electron fluxes observed by EPT in channel 1 (0.5-0.6 MeV) between 15 February and 15 March 2015 (before the event). 80
3.10 Channel 1 (0.5-0.6 MeV) EPT electron fluxes as a function of L between 1 January and 30 June 2015. Bottom panel shows the Dst index during the same period. 81
3.11 Map of the electron fluxes observed by EPT in channel 1 (0.5-0.6 MeV) between 16 March and 13 April 2015 (after the event). 82
3.12 Map of the electron fluxe measured by EPT in channel 1 (0.5-0.6 MeV) from 28 March up to 10 April 2015 (10 days after the event). 83
3.13 Proton fluxes observed by EPT in channel 1 (9.5–13 MeV) as a function of L between 1 January and 30 June 2015 (upper panel) and focused between 28 February and 13 April 2015 (bottom panel) to emphasize that the March proton injection starts on 15 March 2015 due to the arrival of solar energetic protons (SEP event). 84
3.14 Map of the proton fluxes observed in channel 2 by PROBA-V/EPT from 16 March until 13 April 2015. 86
3.15 EPT electron fluxes: upper panel, in channel 1 (0.5-0.6 MeV) from 21 May 2013 to 1 January 2018. The middle panel shows channel 5 (1-2.4 MeV). The Dst index is also shown in the lower panel for the same period. 87
3.16 EPT electron fluxes in channel 6 (2.4-8 MeV) from 21 May 2013 to 1 January 2018. Dst index is also shown for the same period. 88
3.17 EPT proton fluxes in channel 2 (13-29 MeV) from 1 January 2015 to 1 January 2018. Red dots mark the SEP events. 89
3.18 EPT Proton fluxes in channel 4 (61-92 MeV) from 21 May 2013 to 1 January 2018. 90

3.19 EPT electron fluxes for channel 5 (1.0-2.4 MeV). The black curve represents the plasmapause location calculated as a function of Dst index, according to equation (3.1), from O'Brien and Moldwin (2003). . . . 91

3.20 Plasmapause location comparison of Van Allen Probes (5.6 MeV, top panel from Baker et al. (2014)) and EPT electrons (2.4-8 MeV, bottom panel), using the equation derived by O'Brien and Moldwin (2003) as function of Dst index. 92

3.21 Plasmapause location computed using Kp index as presented by Carpenter and Anderson (1992), superimposed on EPT electron channels 5 (1.0-2.4 MeV) and 6 (2.4-8.0 MeV). 93

3.22 Plasmapause location plotted with channels 5 (1.0-2.4 MeV, upper panel) and 6 (2.4-8.0 MeV, lower panel) of EPT. In red is the calculation performed with Dst method (O'Brien and Moldwin, 2003), while in black is the plasmapause location as function of Kp index (Carpenter and Anderson, 1992). 94

4.1 Map of the electron fluxes in channel 1 (0.5–0.6 MeV) observed by EPT during October 2013, including the five bins that are studied. 99

4.2 Proton fluxes measured by EPT in channel 2 (13–29 MeV) during November 2013. The used measurements have pitch angles between 80° and 100°. The five bins used for the study are also illustrated. . . . 100

4.3 Zoom of the SAA showing electron fluxes in channel (1.0-2.4 MeV) observed by EPT during October 2013, including the five bins that will be studied, the L shells corresponding to the bins center, and the border of the SAA for channel 1 at $L = 2.2$. . . 102

4.4 Average electron spectra observed by EPT in October 2013 in the SAA for the 5 bins color coded. The upper panel shows the differential flux, while the bottom panel shows the integral flux. 103

4.5 Map for electrons flux observed by EPT during April 2015 in channel 1 with energies between 0.5 and 0.6 MeV, and channel 5 with energies between 1.0 and 2.4 MeV. The fluxes in channel 5 still remain very high in the SAA, mostly in the south part. 105

4.6 Omnidirectional integral flux of electrons spectra for the five bins during April 2015. 106

4.7 Average integral electron spectra observed by EPT in October 2013 in bins 1 and 4 of the SAA and comparison with models AE8-MAX on the same bins. 107

4.8 Average integral electron spectra observed by EPT in October 2013 and April 2015 in bin 1 of the SAA and comparison with predictions for bin 1 of AE8-MAX. 109

4.9 Zoom of the SAA during November 2013. The five bins are shown as their L position. 110

4.10 Zoom of the SAA during November 2013. The upper panel shows channel 2 (13-29 MeV) and the L-shell that crosses the south limit of the SAA. Lower panel shows channel 7 (155-182 MeV) and the L-shells for channel 7 and channel 2. We can see that for high energy there are no particles between $L = 1.7$ and $L = 2.23$. 111

4.11 Average differential proton spectra observed by EPT from October to December 2013 from 13 to 248 MeV in the five different bins of the SAA. Error bars are shown for bin 1. The other four bins have similar error bars, but are not shown to avoid confusion. The average was calculated as the mean of the flux for a determined energy channel during three months, and the errors as the standard deviation of the mean for the same period. 113
4.12 Integral proton spectra during October until December 2013. 114
4.13 Averaged proton spectra using integral flux measured by EPT from April to June 2015, for the same five bins used from October to December 2013 in Figure 4.12. 115
4.14 EPT spectra on bin 1 (black) between October and December 2013, compared with AP8-min (blue) and AP8-max (red). 116
4.15 Electrons temporal evolution during 31 months, for bins 1 and 3. The curve in black represents channel 1 (0.5-0.6 MeV) while the red one shows channel 5 (1-2.4 MeV). The vertical dotted lines show the SEP events for this period. 118
4.16 Same as Figure 4.15 but for bin 5. 119
4.17 Temporal evolution of the proton flux during the period of EPT from June 2013 to April 2016, for channel 2 (13–29 MeV) in black and ch7 (155–182 MeV) in red. Bin 1 is shown on the upper panel, bin 4 in the middle, while bin 5 can be seen on the lower panel. The gray rectangle masks the period when the instrument was off due to recalibration. 120

List of Tables

1.1 Characteristic periods of the three types of motion and the gyroradius r_L for 1 MeV electrons and 1 MeV protons at 2000 km altitude, near the equator (Hess, 1968). 15
1.2 Summary of source and loss processes for particle in the radiation belts. 24

2.1 List of SEP events during the studied period (21 May 2013 to 15 January 2014). This information is available at `https://umbra.nascom.nasa.gov/SEP/` . . 47

List of Acronyms

ACE	Advanced Composition Explorer
ADC	Analogue to Digital Converter
B.USOC	Belgian User Support and Operation Centre
CME	Coronal Mass Ejection
CNRS	Centre national de la recherche scientifique (France)
CRAND	Cosmic Ray Albedo Neutron Decay
CSR	Center for Space Radiations
DAM	Digital and Absorber Module
Dst	Disturbance storm time index
EPT	Energetic Particle Telescope
ESA	European Space Agency
FoV	Field of View
GEO	Geostationary Earth Orbit
GTO	Geostationary Transfer orbit
GOES	Geostationary Operational Environmental Satellites
HES	High Energy Section
IASB-BIRA	Institut royal d'Aéronomie Spatiale de Belgique/ Koninklijk Belgisch Instituut voor Ruimte-Aeronomie
IGRF	International Geomagnetic Reference Field
IMF	Interplanetary Magnetic Field

LEO	Low Earth Orbit
LES	Low Energy Section
NOAA	National Oceanic and Atmospheric Administration
ONERA	Office National d'Études et de Recherches Aérospatiales (France)
PA	Pitch Angle
POES	Polar Orbiting Environmental Satellites
PROBA-V	PRoject for On-Board Autonomy Vegetation
RBSP	Radiation Belts Storm Probes
SAA	South Atlantic Anomaly
SAMPEX	Solar, Anomalous, and Magnetospheric Particle Explorer
SEE	Single Event Effects
SEP	Solar Energetic Particle event
SPAND	Solar Proton Albedo Neutron Decay
SPENVIS	SPace ENvironment Information System
TOP model	Transient Observation-based Particle model
UCL	Université Catholique de Louvain
USSR	Union of Soviet Socialist Republics
UTC	Coordinated Universal Time
VAP	Van Allen Probes (also known as RBSP)

Chapter 1

Introduction

1.1 Magnetosphere

The magnetic field of the Sun is called the Interplanetary Magnetic Field (IMF). The IMF is transported with the solar wind, which is the flow of supersonic plasma (mainly electrons and protons) ejected by the Sun with an average speed of 400 km/s in the equatorial plane (Pierrard, 2009). The magnetosphere (see Figure 1.1) is the region where the Earth's dipole magnetic field interacts with solar wind particles.It extends from around ten Earth radii in the direction of the Sun to more than hundred Earth radii on the tail side (Kallenrode, 2001). The boundary between the IMF and the terrestrial magnetic field is called the magnetopause. In front of it we find the bow shock, a shock wave created by the encounter of the solar wind (supersonic speeds) with the Earth's magnetic field. At the same time the solar wind will compress the sunward side of the Earth's dipole field and it will stretch the field lines in the anti-sunward direction, creating the magnetotail. At the equatorial plane there is a region of closed field lines filled with hot plasma called plasmasheet, which separates the opposite direction magnetic fields. In the inner magnetosphere we find particles trapped along the closed field lines. There is cold, dense plasma in the plasmasphere, whose outer boundary, the plasmapause, interfaces it to

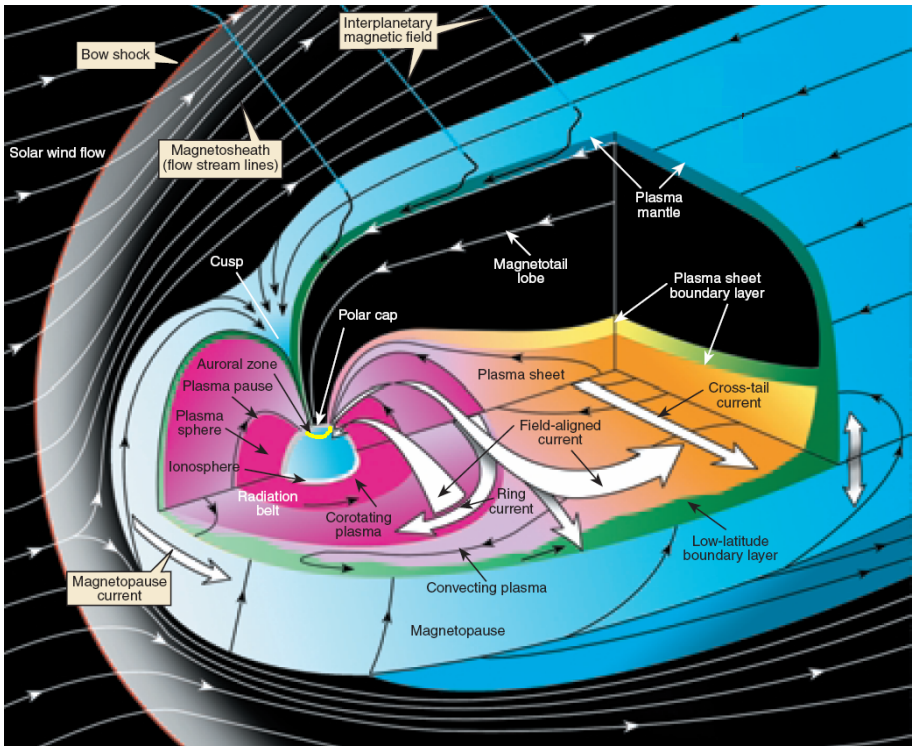

Figure 1.1: The Earth's magnetosphere diagram (modified from Kivelson and Russell (1995))

a lower density plasma region called the plasmatrough. Energetic particles forming the Van Allen radiation belts (explained in section 1.5) are also part of the inner magnetosphere.

The particles circulating in the magnetosphere come from different origins: (i) solar wind particles that can penetrate via the magnetotail, or (ii) through the polar cusps as done by solar energetic particles. There are also (iii) galactic cosmic rays, (iv) particles generated by the interaction of the magnetosphere with the ionosphere (Kallenrode, 2001), and (v) ionospheric particles can move up into the magnetosphere as they are energized by solar UV radiation.

1.1.1 Geomagnetic storms

Geomagnetic storms are geomagnetic disturbances caused by fast solar wind streams or interplanetary shocks. During big storms particles can be injected into the radiation belts: the increment on the solar wind flux will inject particles from the plasmasheet in the magnetotail, reaching later the Van Allen belts. The time scales can be very short, and the density of the belts can be enhanced by more than one order of magnitude, as it will be shown in Chapter 3.

The storms can be quantified by the Dst index or Disturbance Storm Time index, which is the globally hourly averaged change of the horizontal component of the Earth's magnetic field at the magnetic equator (Kallenrode, 2001). The Dst index is computed with measurements from four observatories[1]: Hermanus (South Africa), Kakioka (Japan), Honolulu (Hawaii), and San Juan (Puerto Rico) in units of nano tesla nT. The geomagnetic storms can be described in 3 phases as shown in Figure 1.2:

- Initial phase or sudden commencement (SC): there is an increment in the magnetic field strength due to the compression of the frontside of the magnetosphere, and the magnetopause is pushed inward by the increased solar wind speed.

- Main phase: it is when the Dst index rapidly drops to negative values, reaching a minimum. The magnetic field strength decreases as a consequence of the increase in the ring current, which will create a magnetic field opposite to the Earth's magnetic field.

- Recovery phase: finally the Dst will recover and the magnetic field will go back to its original configuration.

[1] More information about these stations can be found at `http://wdc.kugi.kyoto-u.ac.jp/dstdir/dst2/onDstindex.html`, as well as the Dst values since 1957.

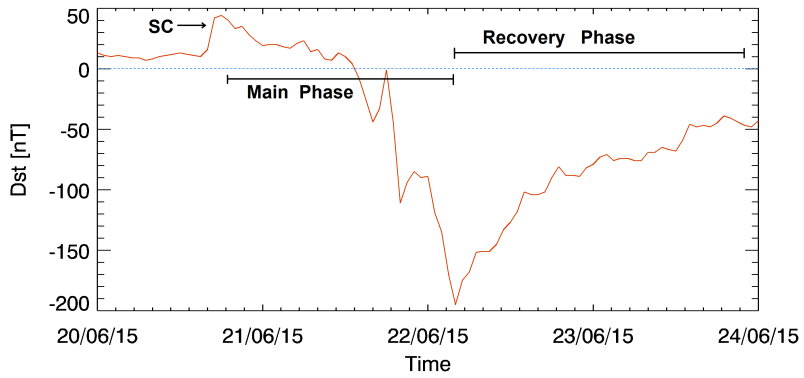

Figure 1.2: Example of a large geomagnetic storm (starting on 20 June 2015) represented as Dst variation.

The duration of a storm can be between one to five days, where the initial phase can last up to one day, the main phase also takes around one day and the recovery phase several days (Kallenrode, 2001). The occurrence of these events depends on the intensity (in nT): storms which reach a Dst minimum of Dst=[-150,-50] occur on average once a month, storms with Dst=[-300,-150] only a few times in a year. Storms with even lower Dst values, as Dst=[-500,-300] occur more rarely.

Other geomagnetic indices exist like AE (Auroral Electrojet (Davis and Sugiura, 1966), which quantifies the ionospheric currents in the auroral zone), and Kp (or Bartels planetary geomagnetic index, see second panel in Figure 3.1). The last one was defined by Bartels et al. (1939) and represents the disturbance levels of the horizontal component of the Earth's magnetic field, measured in 13 subauroral ground observatories[2], and then averaged every three hours, in a logarithmic scale from 0 to 9, and a scale of thirds (-,o,+), thus the Kp values can be 0o,0+,1-,1o,1+,...,9-,9o. During

[2]For more information about the observatories and nowcast of Kp visit `https://www.gfz-potsdam.de/en/kp-index/`

a geomagnetic storm, while Dst will decrease to negative values, Kp index will increase up to the maximum disturbance, when $Kp = 9o$.

Smaller perturbations are called substorms. In contrast to the long disturbances of the magnetic field caused by the geomagnetic storms, substorms last only a few hours, and they are the result of magnetic reconnection in the plasmasheet (Kallenrode, 2001).

1.1.2 Solar Energetic Particle (SEP) events

SEP events are energetic particles emitted by the Sun, and accelerated due to solar flares or shocks associated with Coronal Mass Ejections or CMEs. The energies of these particles can range between some tens to hundreds of MeV, and the events can last some hours up to a few days (Kallenrode, 2001).

Solar Energetic Particle events are measured by the GOES spacecraft at geosynchronous orbit (more details about GOES are given in section 1.9). An SEP is defined when the proton integral flux for energies higher than 10 MeV reaches at least 10 particles per $cm^2 sr\ s$ at GEO orbit (Figure 3.2). A detailed list of events since 1976 is provided by NOAA Space Environment Services Center at `https://umbra.nascom.nasa.gov/SEP/`

1.2 Space Weather

During the last half of the past century our society has become more and more dependent on satellite systems: telecommunications, GPS, weather forecasting, etc...The exposure of those satellites to the harsh space environment and how to deal with it, has always been a challenge for scientists and engineers.

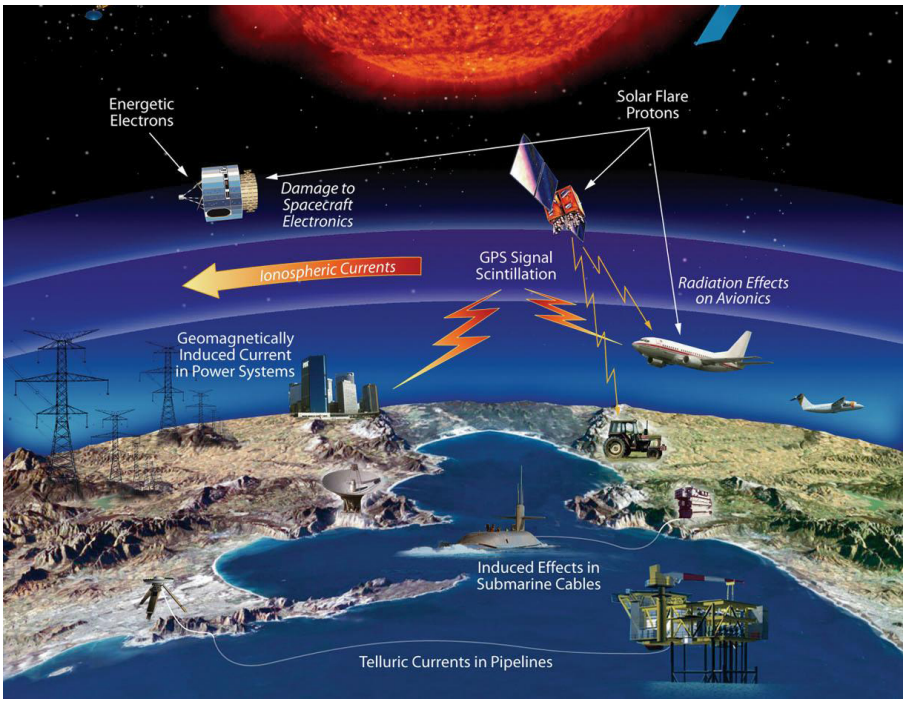

Figure 1.3: Space weather effects (Credits: NASA).

Even more relevant is the hazard that energetic particles can pose to human activity in space.

Geomagnetic phenomena as result of the solar activity, such as storms or different particle species arriving to the magnetosphere and our atmosphere can have a large impact on our technologies, for instance power-line breakdowns or disruption of radio communication (Horne et al., 2013). That is why space weather forecast and the prediction of these phenomena are a key point for scientists. The radiation belts play an important role in this big system, thus a better understanding of them is fundamental to achieve this goal and be able to protect us and our planet.

1.3 Trapped particles motion

In order to understand the dynamics of particles forming the radiation belts, it is necessary to first explain the physics behind trapped particles motion.

A charged particle immersed in an electromagnetic field will be governed by the Lorentz force:

$$\vec{F} = q(\vec{E} + \vec{v} \times \vec{B}), \tag{1.1}$$

where q is the charge of the particle, $\vec{v}$ its velocity vector, $\vec{E}$ is the electric field vector and $\vec{B}$ is the magnetic field vector.

The equation of motion of a charged particle trapped in the Earth's magnetic field is

$$m\frac{d\vec{v}}{dt} = q(\vec{E} + \vec{v} \times \vec{B}) + m\vec{g}. \tag{1.2}$$

The gravitational term $m\vec{g}$ is negligible for particles with energies higher than 10 keV, as well as the electric force $q\vec{E}$ assuming a strong magnetic field and high energy particles (thus high speed, for energies $>$ 100 keV) (Pierrard, 2009). Under these considerations we can break down the radiation belts particles movements in three periodic motions, described next and shown in Figure 1.4. The relativistic counterparts of the main equations shown here, are presented in the Appendix A.

1.3.1 Gyration

For a charged particle in an uniform magnetic field, and no external forces, the motion can be decoupled in a gyration motion perpendicular to the magnetic field, around the center of the orbit or guiding center, and a movement parallel to the magnetic field vector, as $\vec{v} = \vec{v}_\perp + \vec{v}_\parallel$.

The pitch angle α is defined as the angle between the velocity vector $\vec{v}$ and the magnetic field vector $\vec{B}$, thus

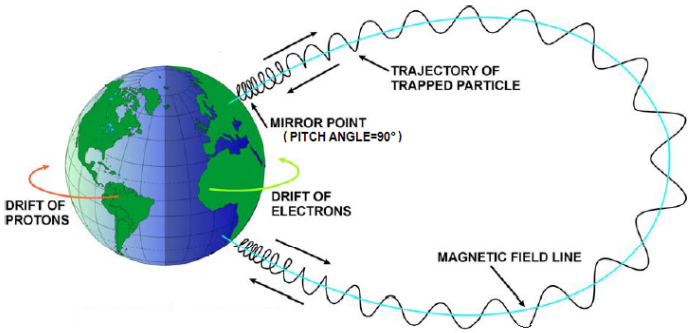

Figure 1.4: Three components of the motion of a charged particle in a magnetic field: gyration, bounce and drift (adapted from Hess (1968))

$$\alpha = \arctan\left(\frac{v_\perp}{v_\parallel}\right), \tag{1.3}$$

from where we see that the perpendicular and parallel components are respectively $v_\perp = v\,\sin\alpha$ and $v_\parallel = v\,\cos\alpha$.

From the balance between the Lorentz force and the centripetal force we can obtain the gyroradius (also called Larmor radius r_L) and gyrofrequency (ω_L) of the particle around the magnetic field line:

$$m\frac{v_\perp^2}{r_L} = |q|v_\perp B, \tag{1.4}$$

$$r_L = \frac{mv_\perp}{|q|B}, \tag{1.5}$$

$$\omega_L = \frac{|q|B}{m}. \tag{1.6}$$

The gyroperiod or Larmor gyration period is

$$T_L = \frac{2\pi}{\omega_L} = \frac{2\pi m}{|q|B} \tag{1.7}$$

Equation (1.5) shows us that if $\vec{B}$ is weak, the gyration radius is bigger, as we can see in Figure 1.4 where the gyroradius r_L is larger at the equator. Note also that electrons and ions will gyrate in opposite directions (ions clockwise while electrons anticlockwise, as illustrated in Figure 1.4) because the acceleration of the particles depends on the charge (see equation (1.2)). For 1 MeV particles, the gyroradius is 0.32 km for an electron and 10 km for a proton, as shown in Table 1.1.

1.3.2 Bounce

According to Faraday's law, the magnetic flux Φ in a circle is constant,

$$\Phi = B\pi r_L^2, \tag{1.8}$$

substituting the gyroradius from equation (1.5):

$$\Phi = B\pi \left(\frac{mv_\perp}{qB}\right)^2 = \frac{\pi m^2}{q^2}\frac{v_\perp^2}{B}. \tag{1.9}$$

As π, q, m are constants, it follows that

$$\frac{v_\perp^2}{B} = constant. \tag{1.10}$$

Using the definition of pitch angle α (equation (1.3))

$$\frac{v^2 \sin^2 \alpha}{B} = constant. \tag{1.11}$$

If this is valid, the ratio is the same at the equator as at higher position (let's call it at point M), hence

$$\frac{\sin^2 \alpha_{eq}}{B_{eq}} = \frac{\sin^2 \alpha_M}{B_M}. \tag{1.12}$$

Consequently, a particle moving along a field line from the equator, where B is minimal, towards an increasing magnetic field region, will have to increase its pitch angle too. However, this increment can go only up to 90°, where B is equal to B_M, and the particle's velocity is $v = v_\perp$, thus perpendicular to the magnetic field. This point previously named 'M' is called the mirror point, where the parallel velocity component of the guiding center is zero. Because the particle cannot go further, it will bounce back to a region with a lower magnetic field strength.

1.3.3 Drift

This motion is related with the external forces acting on the charged particle. The force is perpendicular to the magnetic field, and the particle velocity can be decomposed as a gyration motion around the guiding center $\vec{v}_L$ and a drift of the guiding center $\vec{v}_D$, thus $\vec{v} = \vec{v}_L + \vec{v}_D$ (Pierrard, 2009).

From equation (1.2) we can derive the drift velocity $\vec{v}_D$ related with an external force, which can be written as

$$\vec{v}_D = \frac{\vec{F}_{ext} \times \vec{B}}{qB^2}. \tag{1.13}$$

Due to the drift velocity being perpendicular to the external force $\vec{F}_{ext}$ and the magnetic field, the particle will drift azimuthally.

Thus the drift velocities depending on the different external forces are:

- for the gravitational force, $\vec{F} = m\vec{g}$, where the gravitational field is perpendicular to the homogeneous magnetic field,

$$\vec{v}_g = \frac{m}{q}\frac{\vec{g} \times \vec{B}}{B^2}. \tag{1.14}$$

  In this case, the drift velocity depends on the particle's charge, therefore electrons drift West ($q < 0$) and ions drift East

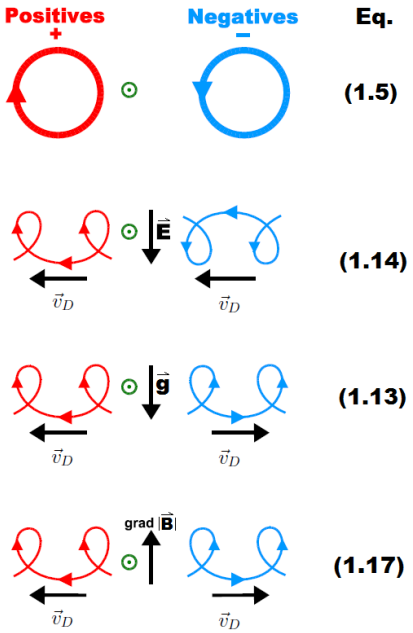

Figure 1.5: Gyration motion (on top) and drift in different types of fields, where the magnetic field $\vec{B}$ is upward through the paper, and **Eq.** indicates the equation that describes the motion. Ions are shown in red and electrons in blue (adapted from Kallenrode (2001)).

($q > 0$). It is important to also notice that for ions $\vec{v}_g$ is much bigger due to the particle's mass.

- For an electric force or Coulomb force, $\vec{F}_E = q\vec{E}$, where the electric field $\vec{E}$ is uniform and perpendicular to $\vec{B}$,

$$\vec{v}_E = \frac{\vec{E} \times \vec{B}}{B^2}. \tag{1.15}$$

Because equation (1.15) is independent of the mass and the charge of the particle, both particle species, electrons and ions drift in the same direction, as shown in Figure 1.5, and with the same velocity.

- In an inhomogeneous magnetic field, the magnetic force created by the gradient of the field is $\vec{F} = -\mu_B \vec{\nabla} B$, where μ_B is the magnetic moment of the dipole, defined as:

$$\mu_B = \frac{m v_\perp^2}{2B}, \tag{1.16}$$

replacing the force in equation (1.13), we obtain:

$$\vec{v}_\nabla = \frac{m v_\perp^2}{2qB^3}(\vec{B} \times \vec{\nabla} B). \tag{1.17}$$

Using equation (1.5) we can rewrite this expression as:

$$\vec{v}_\nabla = \frac{v_\perp r_L}{2B^2}(\vec{B} \times \vec{\nabla} B). \tag{1.18}$$

Equations (1.17) and (1.18) show us that the drift velocity is dependent on the charge of the particle so ions and electrons will drift in opposite directions as can be seen at the bottom of Figure 1.5, where ions drift West and electrons drift East. For the guiding center approximation to be valid the gyroradius r_L must be much smaller than the variation of the magnetic field:

$$r_L \ll \frac{B}{\nabla B} \Longleftrightarrow \frac{mv_\perp}{qB} \ll \frac{B}{\nabla B} \Longrightarrow v_\nabla \ll v_\perp \tag{1.19}$$

The drift of particles (electrons and ions) between 1 to 100 keV due to the magnetic field gradient contributes to the ring current, which is responsible for the decrease of the Earth's magnetic field during geomagnetic storms (Pierrard, 2009).

- If we consider the same inhomogeneous magnetic field, a new drift is introduced if the magnetic field lines are curved, called curvature drift (see Figure 1.6). Here the centrifugal force experienced by the particle having a velocity component parallel to the field $v_\parallel$ is

$$\vec{F}_c = \frac{mv_\parallel^2}{R_c}\vec{n}, \tag{1.20}$$

here $R_c = \dfrac{B}{\nabla B}$ is the curvature radius of the field lines (assuming $\nabla \times \vec{B} = 0$) and $\vec{n} = -\dfrac{R_c(\vec{\nabla}B)_\perp}{B}$ is the unit vector. Replacing in equation (1.13), the curvature drifts is:

$$\vec{v}_{R_c} = \frac{mv_\parallel^2(\vec{\nabla}B)_\perp \times \vec{B}}{qB^3}. \tag{1.21}$$

Again because the charge of the particle is present in the velocity equation, ions and electrons drift in opposite directions.

It is often used to combine both drifts –the one due to the magnetic force, and the curvature drift– and call it the gradient-curvature drift. This can be written as:

$$\vec{v}_{(\nabla+R_c)} = \frac{m}{2qB^3}(v_\perp^2 + 2v_\parallel^2)\vec{B} \times \vec{\nabla}B. \tag{1.22}$$

In this case electrons drift East and ions West.

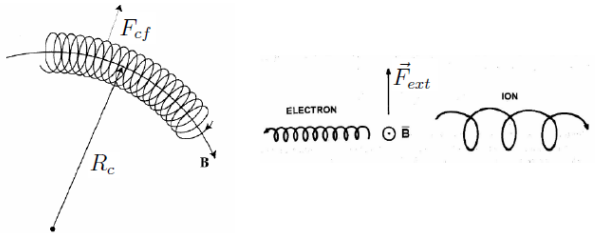

Figure 1.6: Curvature drift, where $\vec{F}_{cf}$ is the centrifugal force acting on the particle, and R_c is the curvature radius.

- When the drift velocity of the guiding center is not constant, there is an inertia force $\vec{F} = -m\dfrac{d\vec{v}_D}{dt}$. For a time dependent electric field $\vec{E}$, this force will be

$$\vec{F} = -m\frac{d\vec{E}}{dt}. \tag{1.23}$$

  Inserting this force in equation (1.13), we obtain what is called the polarization drift:

$$\vec{v}_P = -\frac{m\frac{d\vec{E}}{dt} \times \vec{B}}{qB^2} = -\frac{m}{qB^2}\frac{d\vec{E}}{dt}. \tag{1.24}$$

The total drift of the particles is the superposition of all the components mentioned above: $\vec{v}_D = \vec{v}_g + \vec{v}_E + \vec{v}_\nabla + \vec{v}_{R_c} + \vec{v}_P$. The importance of each term depends on the particle's energy, the intensity and gradient of the magnetic and electric field, and their temporal variations (Pierrard, 2009).

Table 1.1 presents the periods associated with each motion for electrons and protons.

1.3.4 Adiabatic Invariants

Each of the motions described in the preceding sections can be associated with a constant of motion or an adiabatic invariant. This

	1 MeV Electrons	**1 MeV Protons**
r_L	0.32 km	10 km
Gyration	7×10^{-6} s	4×10^{-6} s
Bounce	0.1 s	2.2 s
Drift	53 min	32 min

Table 1.1: Characteristic periods of the three types of motion and the gyroradius r_L for 1 MeV electrons and 1 MeV protons at 2000 km altitude, near the equator (Hess, 1968).

means that for a very slow change of one of the variables involved, the motion remains approximately constant. For the specific case of the radiation belts particles the system remains approximately constant under the effect of a slowly and weakly varying field, compared to the gyroradius and period of the particle. Nonetheless, some physical processes can sometimes lead to the violation of the adiabatic invariants (Northrop and Teller, 1960). In general the motion can be described with the action integral, for the variables (q_i, p_i) where q_i is the position of the particle and p_i is the particle's momentum:

$$J_i = \oint p_i dq_i. \tag{1.25}$$

- **First adiabatic invariant (gyration):**

  Equation (1.16) shows that the magnetic moment of a particle rotating around a line of force in a static magnetic field depends of the mass, the velocity and the magnetic field. Now if the magnetic field slowly varies with the time, we can consider that μ remains constant:

$$\mu = \frac{p_\perp^2}{2mB} = constant. \tag{1.26}$$

This implies that when B increases, the velocity $v_\perp$ must also increase.

In reality, this invariant is rarely violated because $t_{dB} \gg T_L$ (t_{dB} is the magnetic field time variation and T_L is the gyration period), in other words, the spatial and temporal variations of the magnetic field occur in a longer time span than the gyration period.

- **Second adiabatic invariant (bounce):**

  The second adiabatic invariant is sometimes called integral or longitudinal invariant and it is associated to the oscillation movement of a particle along a field line between the two mirror points.

$$J_2 = \oint p_\parallel ds. \tag{1.27}$$

In equation (1.27) $p_\parallel$ is the parallel component of the momentum to the magnetic field and ds is the path length along the field line between the mirror points. This parallel component can be written as $p_\parallel = p\cos\alpha$. At the mirror point, the pitch angle is $\alpha = 90°$, thus $\sin^2\alpha = 1$, and from equation 1.12 it is visible that at an s point on the particle's trajectory

$$\begin{aligned} \sin^2\alpha_1 &= \frac{B_s}{B_M}, \\ \cos\alpha &= \sqrt{1 - \frac{B_s}{B_M}}. \end{aligned} \tag{1.28}$$

Under a slow variation of the magnetic field, the magnetic moment μ and the momentum p are constant. Now replacing in equation (1.27) it yields:

$$\frac{J_2}{2p} = \int_{s_M}^{s'_M} \left(\sqrt{1 - \frac{B_s}{B_M}}\right) ds. \tag{1.29}$$

where s'_M and s_M are the mirror point locations.

If the particle is moving to a region where the magnetic field is more intense, the mirror points will be located at higher altitudes, consequently the distance between the mirroring points will be smaller. Finally, this implies that if $\vec{B}$ increases, the mirror points reach higher altitudes, and $v_{\parallel}$ increases too.

The second adiabatic invariant can be broken during quick field variations, therefore $t_{dB} \gg T_{osc}$ or the characteristic time variation of $\vec{B}$ is larger than the oscillation period. This occurs in the region where the field lines are elongated enough, around 8 Earth radii.

- **Third adiabatic invariant (drift):**

  It states the conservation of the magnetic flux Φ enclosed by the azimuthal drift orbit, where the magnetic flux is

$$\Phi = \oint A dI, \tag{1.30}$$

  and A is the vector potential of the magnetic field (McIlwain, 1966).

  It is also possible to write the third invariant as:

$$J_3 = \oint m v_D d\psi, \tag{1.31}$$

  with v_D the drift velocity and ψ the azimuthal angle between 0 and 2π.

  This invariant is the most commonly broken, when $t_{dB} < T_D$ so the $\vec{B}$ variation is faster than the drift period (see for instance Table 1.1).For example, for magnetic field variations occurring in less than an hour, caused by wave-particle interactions, electrons will be accelerated and the third adiabatic invariant will be no longer valid (Pierrard, 2009).

1.4 Coordinates system

In 1961, Carl McIlwain introduced a new parameter L or magnetic shell parameter, as a function of B and I (the magnitude of the magnetic field, and the integral invariant, respectively). The integral invariant is defined as $I = \frac{J_2}{2p}$, like in equation (1.29) in order to solve the problem of mapping trapped particles (McIlwain, 1961). Nowadays, this coordinate system is one of the most used to study the radiation belts.

McIlwain (1961, 1966) assumes the Earth's magnetic field as a dipole field, where a line of force of this dipole can be described as:

$$R = L_d \cos^2 \lambda, \tag{1.32}$$

where R is the radial distance from the dipole, λ is the magnetic latitude, and L_d is the maximum value of R, which is at the equator when $\lambda = 0$. It is important to see that B and I are constant along lines of force (McIlwain, 1966). Figure 1.7 gives a clearer idea about λ and other parameters used in this section: R is the radial distance to the point X, r_0 is the distance from the center to the equatorial crossing of the field line, in Earth radii, λ is the magnetic latitude, and Λ is the invariant latitude, sometimes also called λ_0. The magnetic latitude λ is equal to the invariant latitude Λ at the Earth surface.

Now under the presence of a dipole, the magnetic field is:

$$B_d = \frac{M}{L_d^3 \cos^6 \lambda}(1 + 3\sin^2 \lambda)^{\frac{1}{2}}, \tag{1.33}$$

with M the dipole magnetic moment (in this case $M = 8.06 \times 10^{25} G\ cm^3 = 0.311653 G R_E$, equivalent to the Earth's dipole moment in 1955 (McIlwain, 1961)).

Then combining the three equations ((1.29),(1.32), (1.33)) McIlwain (1961) defined L as:

$$L^3 B/M = F(I^3 B/M), \tag{1.34}$$

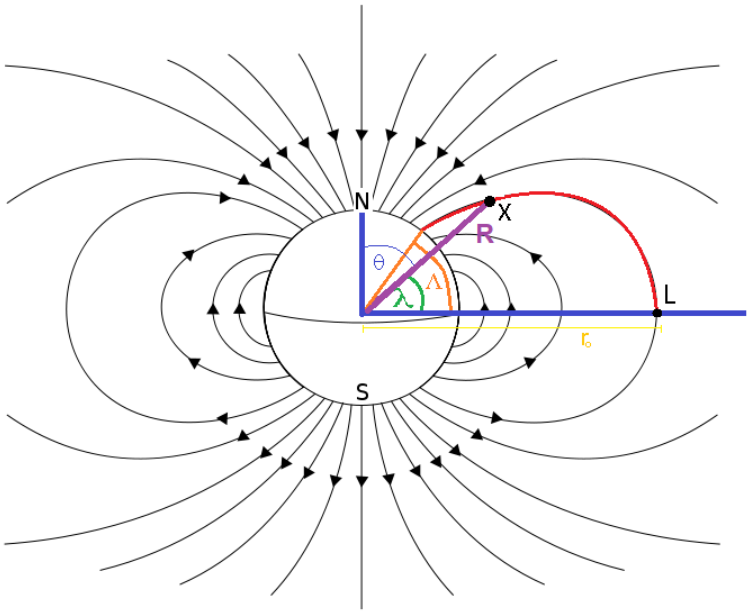

Figure 1.7: Dipolar magnetic field lines of the Earth. For a particle located at point X, the different variables are: L (in Earth radii) is the magnetic-drift shell, λ is the magnetic latitude, θ is the colatitude, R is the radial distance to the X point on the field line, r_0 is the distance to the equatorial crossing of the field line and Λ represents the invariant latitude (adapted from Kivelson and Russell (1995)). From here, it is clear that $\lambda = \Lambda$ for a particle located at the surface of the Earth.

or equivalently,

$$L_d = f(B_d, I_d, M). \tag{1.35}$$

We can see now that the magnetic shell parameter L (in units of Earth radii R_E) depends only on the dipole moment M, the magnetic field B and the integral invariant I, or as McIlwain (1966) states: "in a static dipole field, there exit functions of B and I which depend only on L_d and are therefore precisely constant along the field lines ".

It is also possible to switch from B, L coordinates to polar coordinates R, λ using the transformation:

$$R = L\cos^2\lambda, \tag{1.36}$$

and

$$B = \frac{M}{R^3}\left(4 - \frac{3R}{L}\right)^{\frac{1}{2}}. \tag{1.37}$$

Another useful function is B_0 or the value of the magnetic field B at the equator on the line of force:

$$B_0 = \frac{M}{L^3}. \tag{1.38}$$

This allows us to define B/B_0 as:

$$\frac{B}{B_0} = \frac{(1 + 3\sin^2\lambda)^{\frac{1}{2}}}{\cos^6\lambda}. \tag{1.39}$$

As mentioned earlier, at the Earth's surface the invariant latitude Λ is equal to the magnetic latitude λ, and R the radial distance is equal to 1, thus:

$$\cos^2\Lambda = \frac{1}{L} \tag{1.40}$$

The dipole approximation for the Earth's magnetic field is good enough close to the surface. For higher altitudes or magnetically disturbed conditions, a multipole expansion is more accurate (Kallenrode, 2001).

1.5 Van Allen radiation belts

1.5.1 History

The 4 October 1957 can be cited as the beginning of the Space era, with the first successful launch of a satellite, by the Union of Soviet Socialist Republics (USSR), the Sputnik I. Because of the intense space exploration race (mainly for military purposes at the time) between the United States and the USSR in the height of the Cold war, soon after (31 January 1958) the US launched its first satellite, the Explorer I (for a detailed review of these events see for instance Hess (1968) or Lemaire (2001)).

The "Iowa group" from the University of Iowa, formed by professors James Van Allen, Carl McIlwain, Ernest Ray and George H. Ludwig among others, provided the key payload of Explorer I: a Geiger counter to study cosmic rays intensity. Using these data Van Allen discovered the radiation belts that carry his name today. This discovery was confirmed by the satellite Sputnik III.

1.5.2 Structure

The radiation belts are toroidal structures populated of energetic particles trapped in the Earth's magnetic field (see Figure 1.8). We can distinguish two belts:

Inner belt: It contains mainly energetic protons between 100 keV to hundreds of MeV, located around $2 - 3R_E$. There is also a small population of electrons, with energies varying between some keV and 10 MeV (Pierrard, 2009). But recently Baker et al. (2014) have shown with Van Allen Probes satellites observations that there are no significant relativistic electrons (energy $>$ 2 MeV) in the inner belt (L$<$ 2.8).

Outer belt: It is formed by energetic electrons (from some keV's up to 10 MeV), between 3 and $10R_E$. This region is very dynamic, highly dependent on solar and geomagnetic activity, with flux variations of several orders of magnitude on different timescales.

Some protons can be injected during SEP events, but they do not remain trapped more than some days.

A third belt has also been observed very few times, for example by the CRRES satellite in March 1991 (see for instance Blake et al. (1992); Vampola and Korth (1992); Looper et al. (1994)) and recently with the Van Allen Probes in September 2012 (Baker et al., 2013; Cowen, 2013). Some hypotheses have been provided but a definitive explanation about the formation of this structure and the possible involved mechanisms remain unclear.

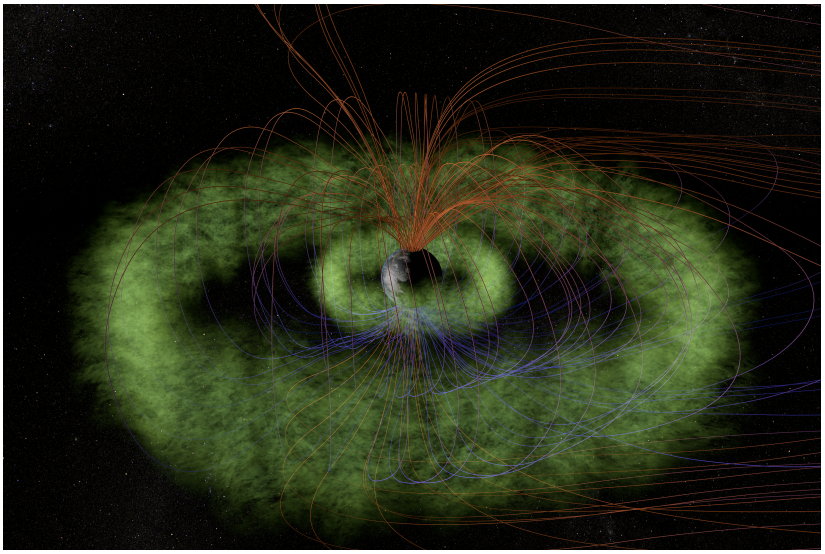

Figure 1.8: Artist conception of the Van Allen radiation belts (Credits: NASA/T. Benesch, J. Carns).

The region that separates both belts is known as the slot region, where the density of energetic particles is very low. This is mainly due to particles scattering by wave-particle interactions (Lyons et al., 1972; Lyons and Thorne, 1973). Although the flux of electrons can drastically increase and fill the slot completely when particles are injected during geomagnetic storms. This will

be shown in Chapter 3.

Different mechanisms are involved in the generation and loss of the radiation belts particles. These source and loss processes will be explained in section 1.6.

1.5.3 The South Atlantic Anomaly (SAA)

The SAA corresponds to the region where the inner Van Allen belt comes closest to the Earth's surface. This is because the axis of the Earth's dipole field is tilted 11° with respect to the rotational axis of the Earth, and is offset 500 km further North with respect to the center of the planet. The SAA covers South America, the Atlantic ocean, and South Africa.

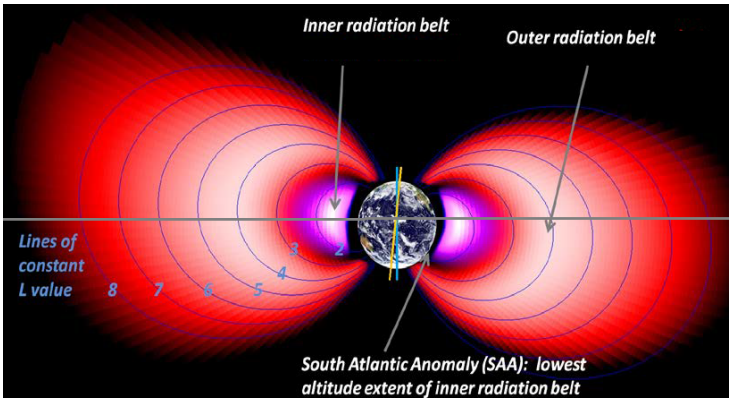

Figure 1.9: Detailed view of the radiation belts, showing the inner and outer belts, the South Atlantic Anomaly and L-shells (taken from Fennelly et al. (2015)). The blue lines represents the rotational axis of the Earth while the yellow one is the dipole axis.

In this region, the magnetic field is weaker, and the inner belt is closest to the Earth's surface. This also produces an increment on energetic particle fluxes at lower altitude, which can be problematic for satellites crossing this region.

The SAA drifts west approximately 0.3° per year (Pierrard, 2009).

1.6 Physical processes in the radiation belts

The dynamics of the radiation belts are modeled by different mechanisms: sources from where particles populate the belts, but also loss mechanisms. The physical processes behind the inner belt and the outer belt are different because of the particle nature and the energies involved.

Table 1.2 shows a summary of the processes involved that will be explained in the next sections.

	Sources	**Losses**
Outer belt	Ionosphere Solar wind	Outward transport to the magnetopause Magnetopause shadowing Wave-particle interactions
Inner belt	CRAND SPAND	Charge exchange Nuclear collisions Coulomb scattering

Table 1.2: Summary of source and loss processes for particle in the radiation belts.

1.6.1 Inner belt

Sources

The main process that provides protons to the inner belt is the disintegration of neutrons, through two mechanisms: CRAND (Cosmic Ray Albedo Neutron Decay) and SPAND (Solar Proton Albedo Neutron Decay). The principle is the same for both: energetic particles (from Galactic Cosmic rays for the first one, and solar protons for the second one) enter the atmosphere and collide with Nitrogen or Oxygen nuclei, creating a neutron. This neutron, with a lifetime around of 1000 seconds, will decay as:

$$n \rightarrow p^{+} + e^{-} + \overline{\nu} \tag{1.41}$$

where $\overline{\nu}$ is an antineutrino (Hess, 1968). A diagram of CRAND is illustrated in Figure 1.10.

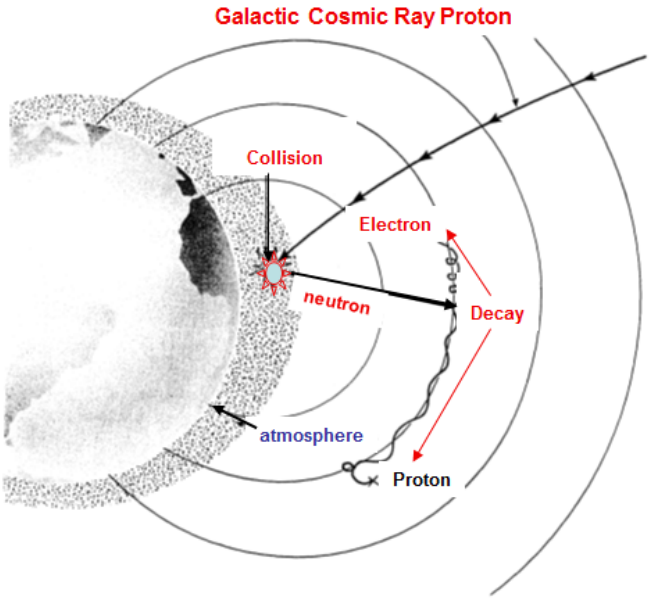

Figure 1.10: CRAND mechanism (Hess (1968))

SPAND protons are generated at the Sun and accelerated by solar flares. This mechanism is ten times less intense as the CRAND source (Kruglanski, 1998).

There is also a small population of electrons, and recently Li et al. (2017) showed that indeed the main source for inner belt electrons is CRAND.

Losses

The main losses are related with particles interactions with the Atmosphere, which can be considered the lower limit of the radiation belts. Mainly three processes can be identified:

1. Charge exchange: A fast proton entering the atmosphere captures an electron after colliding with a neutral atom or molecule. Now the proton has become a neutral hydrogen atom no longer trapped. This is valid for protons below 100 keV (Hess, 1968).

2. Nuclear collisions: They are inelastic collisions of protons above 75 MeV with atmospheric molecules and atoms (Kallenrode, 2001).

3. Coulomb scattering into the loss cone: Mainly electrons are lost by this mechanism because they are lighter than protons, thus they will scatter more easily (Hess, 1968). Scattering can be a consequence of the violation of the second adiabatic invariant, due to changes in the magnetic field at shorter timescales than the bounce period (see section 1.3.4).

1.6.2 Outer belt

As mentioned earlier, the Van Allen outer belt is highly dynamic: particle fluxes can drastically change over timescales ranging from minutes to years. Maybe because of this, there is less consensus about the processes ruling the outer belt. Some mechanisms have been identified but their relevance is still debated.

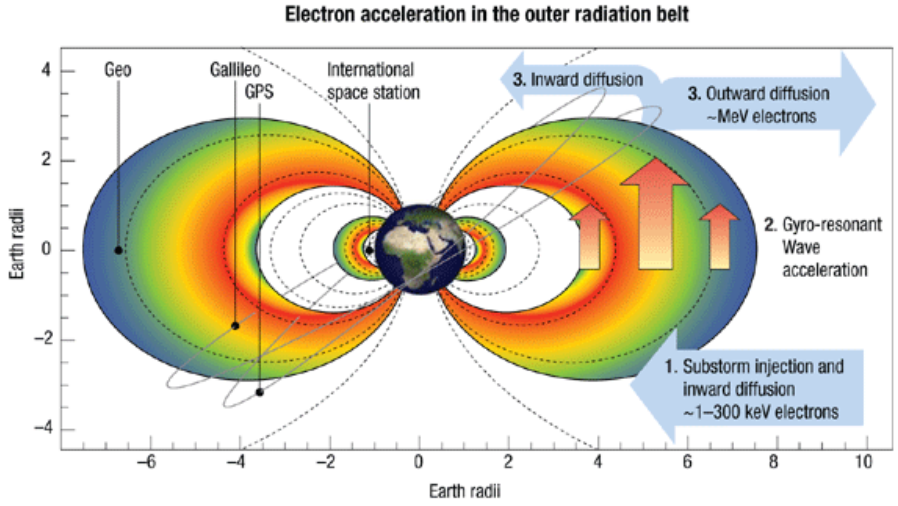

Figure 1.11: Possible explanation of the outer belt dynamics by Horne (2007): 1. Radial diffusion and substorms inject medium-energy electrons from a reservoir in the outer region and excite plasma wave instabilities. 2. Gyro-resonant wave–particle interactions accelerate a fraction of the electrons to relativistic energies (MeV). Acceleration is most efficient in regions of low density. 3. Radial diffusion re-distributes relativistic electrons to fill up the entire outer radiation belt.

Sources

The main source of particles in the outer belt is the solar wind (Pierrard, 2009). Solar wind particles will enter the magnetosphere at the polar cusps, or as Solar Energetic Particles (SEPs) injections. Either source, they both need another mechanisms to accelerate the particles (thus increase their energy) and transport them into the radiation belts.

The transport mechanism is inward radial diffusion (violating the third adiabatic invariant because the variations of the magnetic or electric field, occur on timescales smaller than the drift motion

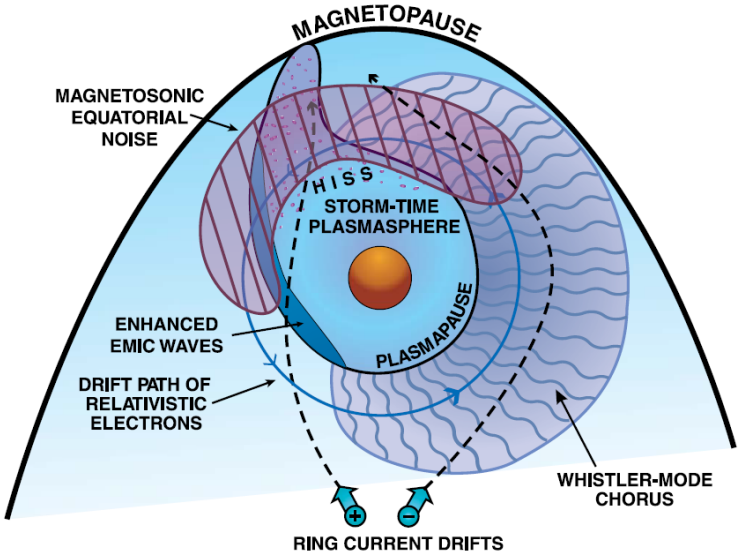

Figure 1.12: Spatial distribution of waves in the inner magnetosphere, in relation to the plasmasphere and the drift-paths of ring-current (10–100 keV) electrons and ions and relativistic ($\geqslant 0.3$ MeV) electrons (Thorne, 2010).

of the particles (Millan and Baker, 2012)), although convection can also contribute (Kallenrode, 2001). The acceleration is done by the betatron effect and Fermi acceleration (Kallenrode, 2001; Horne, 2007).

Figure 1.11 shows a possible scenario to explain the outer Van Allen belt dynamics.

Losses

Particles will be lost when they reach the magnetopause (the outer boundary of the magnetosphere) or when they move inward and interact with the atmosphere. The detailed processes are:

1. Outward radial transport: In order to conserve their third

adiabatic invariant during the main phase of a geomagnetic storm (thus weaker magnetic field strength), particles will move to larger radial distances from the Earth, which can result in losses to the magnetopause. Their energies also decrease to not violate the first adiabatic invariant.

2. Magnetopause shadowing: As a response to the increment in the solar wind dynamic pressure during a geomagnetic storm, the magnetopause will move inward. This will have as result the loss of electrons on the open drift paths that were previously closed (Turner et al., 2012).

3. Wave-particle interactions: There are different types of waves that can interact with radiation belts particles, breaking one, two, or the three adiabatic invariants (Thorne, 2010). Resonances between periodic the particle motion and the waves can energize or scatter particles.

   Some examples of these waves are: **Ultra Low Frequency waves** or ULF have frequencies of the order of mHz. Their interactions with radiation belt particles violates the third adiabatic invariant, driving inward and outward radial diffusion (Shprits et al., 2008b). **Chorus emissions**: they produce fast losses and accelerations outside the plasmasphere (Shprits et al., 2008b). **Plasmaspheric hiss** (within the plasmasphere, 0.2-1 kHz (Hudson et al., 1998)) it is a right-hand polarized whistler-mode emission. According to Shprits et al. (2008b), it is the dominant loss mechanism during quiet times. The slot region is the result of pitch angle scattering by interactions of electrons with this type of waves (Lyons and Thorne, 1973). **Electromagnetic Ion Cyclotron** or EMIC waves are right-hand circularly polarized waves. Destabilized during geomagnetic storms, they can cause rapid scattering and loss for ring current ions (Hudson et al., 1998).

   Figure 1.12 shows a representation of the spatial distribution of these waves in the magnetosphere.

1.7 Proba-V satellite and operations

The Energetic Particle Telescope is a charged particle spectrometer onboard the ESA satellite PROBA-V or **PR**oject **O**n**B**oard **A**utonomy-**V**egetation.

The payload of PROBA-V also includes five other instruments, the main one is a Vegetation imager, a radiation monitor SATRAM, a GaN-based amplifier or GREAT and an air traffic surveillance instrument called ADS-B.

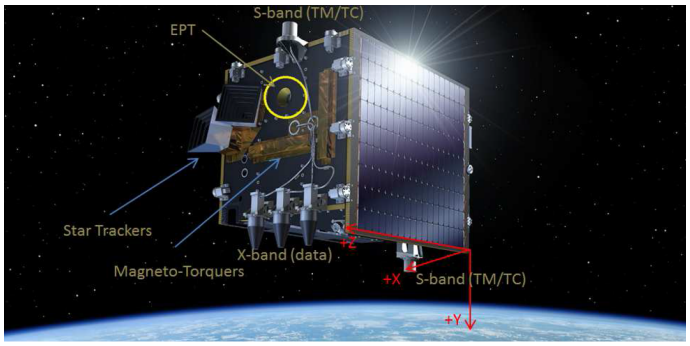

Figure 1.13: Satellite PROBA-V, showing the position of the EPT instrument.

The satellite was launched from Kourou, French Guyana on 7 May 2013 into a LEO (Low Earth Orbit) polar orbit at 820 kilometers altitude, on the VV02 Vega rocket.The inclination is $i = 98.73°$ with a period of 101 minutes, and 10:30 am is the nominal local time at the descending node.

PROBA-V is a cubic satellite of 160 kilograms. As the main payload is a camera to observe the Earth's vegetation, the satellite is stabilized with magnetic torquers to point permanently to Earth with the vegetation imager.

There is a magnetometer onboard to measure the magnetic field (three components, x, y and z) with respect to the satellite reference system: X axis is in the direction of flight, and Z axis points

towards Earth.

The ESA Redu ground station is in charge of the data acquisition from the satellite. Then the B.USOC (Belgian User Support and Operations Centre) gets the raw data and the automatic initial data validation is done through remote desk by CSR (Centre for Space Radiations). After this the data are exported to CSR at UCL (Université catholique de Louvain). They record the L0 level data, check and clean them, and the corrupted data are flagged. Now the conversion to L1 level (energy, flux, etc...) is made. Finally the data are ready to be distributed to the different users. The database can be found as L1 on the website of CSR at `http://web.csr.ucl.ac.be/csr_web/probav/dataaccess.html`

1.8 Energetic Particle Telescope (EPT)

The Energetic Particle Telescope (Figure 1.14) is the result of a fruitful consortium formed by the Royal Belgian Institute for Space Aeronomy (BIRA-IASB), the Centre for Space Radiations (CSR) at the Université catholique de Louvain (UCL) and the private company QinetiQ Space. The Finnish company ASRO also contributed during development phase A/B.

This particle spectrometer specially designed to perform on site particle discrimination has a dimension of $12.75 \times 16.2 \times 21.15\ cm^3$, a weight of 4.6 kg and its power consumption is 5.6 Watt. The field of view or FoV is 52° and the integration time is only 2 s. The instrument is oriented west during day and oriented east during eclipses.

At the entrance of EPT there are three silicon sensors or detectors (Figure 1.14), S1 of 3.5 mm diameter, S2 of 20 mm diameter and S3 with a diameter of 35 mm. When a particle enters the telescope and hits a detector, it has to deposit at least 100 keV to be considered as a valid measurement. The 52° field of view is defined by the two sensors (S1/S3 and S2) because the particle must hit both to trigger the detection process. The combination of the

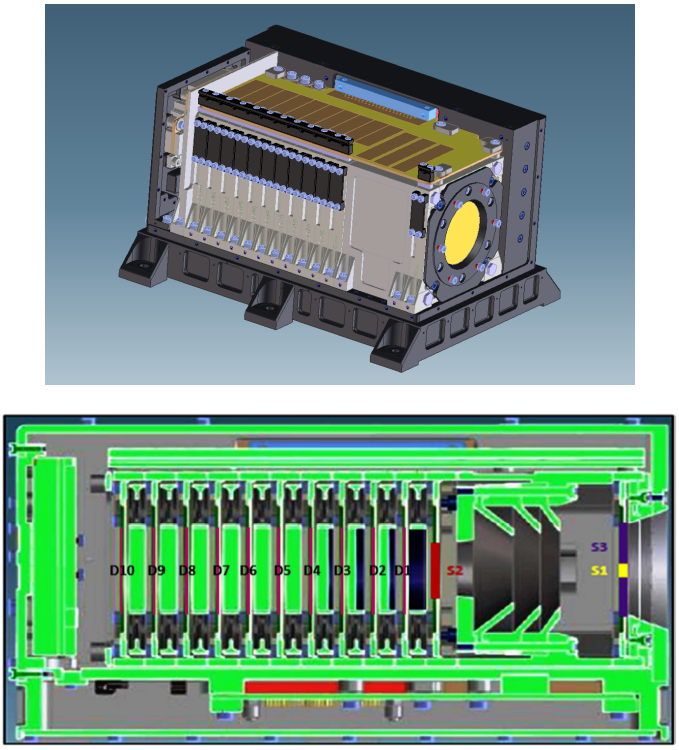

Figure 1.14: Upper panel: Sketch of the Energetic Particle telescope. Bottom panel: cross section of the instrument showing the S1, S2 and S3 detectors. The HES or High Energy Section is defined by 10 DAM (Digital and Absorber Module) detectors (Cyamukungu et al., 2014).

sensors S1/S3 and S2 forms the Low Energy Section (LES) where low energy particles will be detected. The High Energy Section (HES) will be defined by the detector S2 and ten DAMs (Digital and Absorber Module). Each DAM has a 35 mm diameter central sensor which is surrounded by an anticoincidence ring. In front of the central silicon sensor there is an energy degrader (or absorber) material (like aluminum or tungsten). DAMs operate in a so called digital mode, which means they only record if the sensor was hit or not. With the information coming from the detectors S2 and S1/S3 (energy deposited) and the signal from the DAM it is possible to identify the particle specie and its energy (Cyamukungu et al., 2014).

Fluxes of Van Allen radiation belts particles are measured as follows: electrons in 7 virtual channels from 0.5 to 20 MeV, protons in 11 virtual channels ranging from 9.5 to 300 MeV, and 11 virtual channels for heavy ions between 38 and 1600 MeV. Figure 1.15 shows the energy ranges for each virtual channel for the different particle species. These particles are measured in a pitch angle (angle between viewing direction of the instrument and the magnetic field) range between 80° to 120°. Two magnetic fields are used to compute the pitch angle: the calculated magnetic field, based on extrapolations of IGRF2010, and the magnetic field model of Olson and Pfitzer quiet (Olson and Pfitzer, 1974) as external magnetic field (Cyamukungu et al., 2014).

1.9 Satellites

A practical way to evaluate the performance of this new instrument, is to compare it with other satellites, like the ones listed below:

- GOES: or Geostationary Operational Environmental Satellites [3]. It is a constellation of weather satellites in GEO or-

[3]More information about the GOES mission can be found at https://www.nasa.gov/content/goes-overview/index.html, which was used as

Energy channels	Electrons (MeV)	Protons (MeV)	Helium ions (MeV)
1	0.5–0.6	9.5–13	38–51
2	0.6–0.7	13–29	51–116
3	0.7–0.8	29–61	116–245
4	0.8–1	61–92	245–365
5	1–2.4	92–126	365–500
6	2.4–8	126–155	500–615
7	8–20	155–182	615–720
8		182–205	720–815
9		205–227	815–900
10		227–248	900–980
11		> 248	> 980

Figure 1.15: Virtual channels and energy ranges for electrons, protons and Helium ions.

bit, operating since 1975 with the launch of GOES-1 (Goodman et al., 2018). The last GOES launch was in March 2018 (GOES-S or GOES-17) but it will be operational in late 2018. Currently GOES-15 and GOES-16 are in orbit taking science data, and GOES-14 is in storage mode, as a backup in case of problems with any of the other two satellites (Goodman et al., 2018).

The most recent particles data available for public access come from GOES-15, or GOES-west, orbiting in GEO at $\sim 36,000$ km ($L \sim 6.6$), located at 135° west, launched in March 2010. These data come specifically from the EPS or Energetic Particle Sensor package, and its instrument MAGED or MAGnetospheric Electron Detector. It consists of nine solid-state-detector telescopes, which measure 5 energy bands of electrons between 30 keV to 600 keV.

- POES: Polar Orbiting Environmental Satellites project, which

source for this section.

is another constellation of weather satellites but in LEO orbits, starting with TIROS-N (launched in 1978), to NOAA-19 (2009) (NASA). NOAA-14, providing data from 1995 up to 2004, is the most up to date data set accessible[4]. The altitude is 844 km, and inclination=99.1°. The particle detector is MEPED or Medium Energy Proton and Electron Detector, and it measures protons, electrons, and ions with energies between 30 keV and 6.9 MeV.

- RBSP: Radiation Belt Storm Probes, most known as Van Allen Probes, which is a NASA mission dedicated to study the radiation belts. The twin satellites (A and B) were launched in August 2012, into an eccentric orbit (apogee 30,050 and 31250 km, and perigee 500 and 675 km for probe A and B respectively), inclination $i = 10°$ and an orbital period of 9 hours (NASA, 2012). The suite called ECT or Energetic particle, Composition, and Thermal plasma, consists of three instruments specially designed to measure energetic particles. The Magnetic Electron Ion Spectrometer or MagEIS detects electrons and ions in an energy range from 20 keV up to 4.8 MeV (Blake et al., 2013).

There are other satellites that have been used for radiation belts research, but they will not be used on this study. Such is the case of the French satellite DEMETER in a quasi heliosynchronous orbit at 715 km (operating from 2004 to 2010), or the NASA mission THEMIS, consisting of 5 probes in a highly elliptical orbit, still active since their launch in 2007. The ESA satellite constellation Cluster, in an elliptical orbit since 2000 has also contributed to magnetospheric research.

[4]This was the case for the comparisons made in 2014, for the first publication with EPT data: *The Energetic Particle Telescope: First Results*, Pierrard et al. (2014)

1.10 Models

Radiation belt models can be divided into two categories: empirical models based on satellite data and theoretical ones. Some of the most used empirical models are:

- AE8/AP8: NASA static models based on satellite data from early sixties to the mid-seventies, for energy ranges from 0.04 MeV to 7 MeV for electrons (Vette, 1991) and 0.1 MeV to 400 MeV for protons (Sawyer and Vette, 1976). It is possible to choose between a MIN or MAX version, depending on the solar cycle. Figure 2.3 shows an example of AE8-max.

- AE9/AP9-IRENE: Recently renamed IRENE (International Radiation Environment Near Earth) (O'Brien et al., 2018), this model is an updated version of AE8/AP8, which also includes data from RBSP (Ginet et al., 2013).

- TOP: The Transient Observation-based Particle model (Benck et al., 2010; Benck et al., 2013) is a dynamic model based on data of DEMETER (Sauvaud et al., 2008, 2013) and SAC-C that have been registered during the last solar cycle maximum and declining phase (2000–2006). It can predict flux variations during geomagnetic storms.

And the most used theoretical models are:

- BAS-RBM: The British Antarctic Survey Radiation Belt Model[5] is a 3 dimensional, time-dependent diffusion model for phase-space density or flux time series production, based on solution of the Fokker-Planck equation (Glauert et al., 2014). This model also takes into account wave-particle interactions, collisions with the atmosphere, losses to the magnetopause,

[5]For more information and access to the model visit `https://www.bas.ac.uk/science/research-models/bas-radiation-belt-model-bas-rbm/summary-of-features-for-the-bas-global-dynamic-radiation-belt-model/`

and includes radial diffusion coefficients. It can predict radiation belt variations for $L^* = 2.05 - 5.55$, up to energies of 10 MeV for electrons.

- Salammbô: This ONERA/DESP code solves the three-dimensional phase-space diffusion equation (Beutier et al., 1995). It can estimate particle fluxes in the energy range of 10 keV-10 MeV for electrons, and 10 keV-300 MeV for protons (Bourdarie and Boscher, 2006).

1.11 Motivation to study the radiation belts

The Van Allen radiation belts have been studied for decades. Even so, despite the theoretical knowledge accumulated over time –or even the very recent Van Allen Probes mission, specifically designed to study them –important uncertainties remain regarding their dynamics, in all regions of these belts. For instance, it is still not established whether high energy electrons are present in the inner radiation belt of the Earth or not, whereas the mechanisms behind outer belt electrons are not yet fully explained. In addition, the variations in the configuration of the belt associated with changing geophysical conditions are neither entirely understood nor quantified. Filling the knowledge gaps on these issues thus represents an important contribution towards both consolidating the theory behind trapped particles itself and improving our current space weather forecast capabilities.

Therefore, the thrust of the present thesis is to better characterize the changes of the radiation belts, showing specifically how geomagnetic conditions (e.g., geomagnetic storms, SEP events or quiet times) affect the particle fluxes, depending on the type of particles and their energy ranges in the various regions of the belt. This is achieved by studying a new set of satellite observations

(PROBA-V/EPT) with respect to the physics-based mechanisms that determine the distributions of the energetic particles trapped in the magnetic field of the Earth. In particular, the analysis of this dataset yields more accurate insight in assessing the presence of high energy electrons in the inner belt.

This chapter has provided to the reader the necessary background to understand the topics addressed in this thesis. In the next chapter I will present the first results obtained with EPT, concerning electrons, protons and helium ions, and how these different particle species are affected by geomagnetic storms and Solar Energetic Particle Events. Comparisons with other satellites are also shown, in order to validate the data of this new instrument. Chapter 3 will focus on a detailed study of the outer belt and its response to intense geomagnetic storms that occurred in 2015. The spectra of protons and electrons in the South Atlantic Anomaly are presented in Chapter 4. Finally, Chapter 5 summarizes the conclusions presented in this thesis and discusses some perspectives about radiation belt research and EPT data.

Chapter 2

First results

This Chapter is based on the following paper: **Pierrard, López Rosson et al. (2014)** at *Space Science Review*, Volume 184, Issue 1-4, pp. 87-106. DOI 10.1007/s11214-014-0097-8. The present author did the data analysis, most of the figures and contributed with the manuscript text.

2.1 Introduction

PROBA-V/EPT was launched on 7 May 2013. The Energetic Particle Telescope (EPT) took its first particle spectra on 16 May during its first health test (EPT news, CSR webpage).[1] Four operational modes can be identified in the EPT data (Borisov, 2015):

1. Commissioning: 20/05/2013, 00:00:00 – 21/06/2013, 09:37:24 and 24/06/2013, 10:09:16 – 24/06/2013, 19:59:06. During this phase some tests were performed to find the optimal configuration for the instrument. The quality of the data is good,

[1]Published online on 16 May 2013, http://web.csr.ucl.ac.be/csr_web/probav/eptnewspdf/EPTNews0000.pdf

but precaution is still needed to treat the absolute values of fluxes for some channels.

2. Nominal: 21/06/2013, 12:55:54 – 24/06/2013, 10:09:16 and 24/06/2013, 19:59:06 – 27/06/2014, 12:12:11. The instrument was acquiring data under an optimal configuration, obtaining a very good data quality.

3. Recalibration: 27/06/2014, 12:25:20 – 15/09/2014, 11:11:42. An anomaly on sensor S3 noise was suddenly detected on 27 June 2014. At this moment, the baseline counts dropped on both S1 and S3 sensors, and the background counts increased from 50 counts/second to $\sim 5E^4$ counts/second (Borisov, 2015). Some tests were immediately performed to check what was the origin of the problem and recover the instrument nominal performance. The cause of the anomaly remains unknown: there was no SEP event or geomagnetic storm around those dates, and the possibility of electronics failure or voltage issues was discarded. The data of this period should not be used for scientific analysis.

4. Recovered: 11/09/2014, 11:26:15 – now. During the recalibration mode it was finally possible to find a new optimal configuration for EPT, but now it is advised to use proton data only for pitch angle values between 80° and 100°, and be very careful when using channel 1 (9.5-13 MeV) data. It can still be used to see flux variations but it is not recommended to study absolute proton flux values. Later in 2017, it was found that all the proton channels of EPT underestimate the proton fluxes during (and only) SEP events.

A quick look of the EPT data, latest news and how to access the data can be found at `http://web.csr.ucl.ac.be/csr_web/probav/index.html`.

In this chapter we will present the first scientific results obtained with the instrument leading to the first publication concerning the

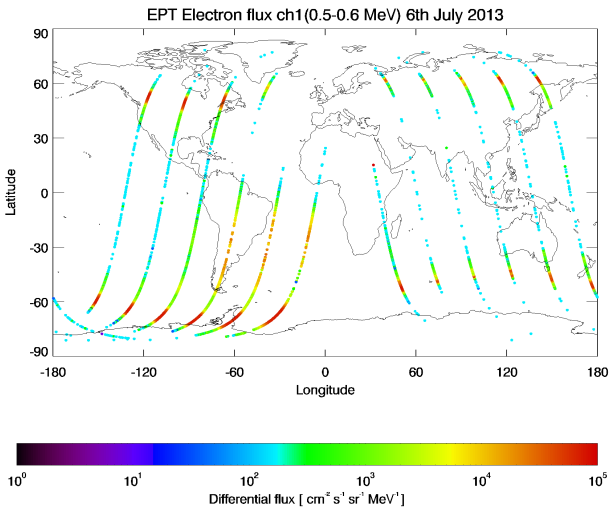

Figure 2.1: Data collected during 6 July 2013 along the PROBA-V LEO orbit at 820 km. The electron flux in channel 1 (0.5-0.6 MeV) is color-coded.

EPT data. The paper focuses on the particle flux variations related to geomagnetic activity.

2.2 Electrons

PROBA-V's orbital period is 101 minutes, thus during a whole day, the satellite will complete multiple orbits around the Earth. This can be seen in Figure 2.1, where each curve represents a satellite's orbit. The day presented on this Figure is the 6 July 2013, when a geomagnetic storm of Dst=-80 nT occurred. In general, electron fluxes are higher during geomagnetic storms than during quiet periods, especially at high latitudes due to particle injections.

The highest fluxes are always observed at lowest energies, which is more clear if we accumulate a longer period of measurements. This is clear is we compare Figure 2.2 (channel 1 (0.5-0.6 MeV)

during the months of June and July 2013, upper and lower panel respectively) and Figure 2.4 (same as Figure 2.2 but for channel 5 (1-2.4 MeV)).

In both images it is possible to distinguish some characteristic features, like the high electron fluxes at the polar "horns" corresponding to the high latitude penetration of the outer belt at low altitudes, and the South Atlantic Anomaly (SAA, see Section 1.5.3). June 2013 was more active than July 2013: There was one SEP (Solar Energetic Particle) event on 23 June, and two geomagnetic storms (1 and 29 June), with Dst values lower than -100 nT, while in July the biggest event was a geomagnetic storm reaching Dst=-87 nT on 6 July. This is why the fluxes observed during June 2013 are slightly higher than July 2013. Also noticeable in Figure 2.2 are the lower fluxes observed in the Northern hemisphere above the North Atlantic. Such low fluxes in the Northern hemisphere were also observed by DEMETER orbiting at an altitude of 700 km (Sauvaud et al., 2008, 2013), as well as by the FEIO detector onboard the SAC-D satellite (S. Bourdarie, personal communication 2014). This is a consequence of the tilt and eccentricity of the geomagnetic field line distribution which, at these longitudes, lifts the mirror points of trapped particles at higher altitudes in the Northern hemisphere than in the Southern one where the surface field intensity is significantly reduced. Because the mirror points are located in the high atmosphere in the Southern hemisphere, the particles are lost and this leads to very low fluxes in the Northern hemisphere above Europe (Pierrard et al., 2014).

These low fluxes are not displayed by the AE8 model (Vette, 1991) (as shown in Figure 2.3) or the more recent AE9 model (Ginet et al., 2013).

The gap in the Northern horn above Europe is due to the data transmission to the ground station located in Redu (Belgium). The instrument is not taking measurements when the data are being downloaded by the ground station.

Figure 2.4 illustrates the electron flux in channel 5 (1-2.4 MeV) for the same months, June (top) and July 2013 (bottom). The

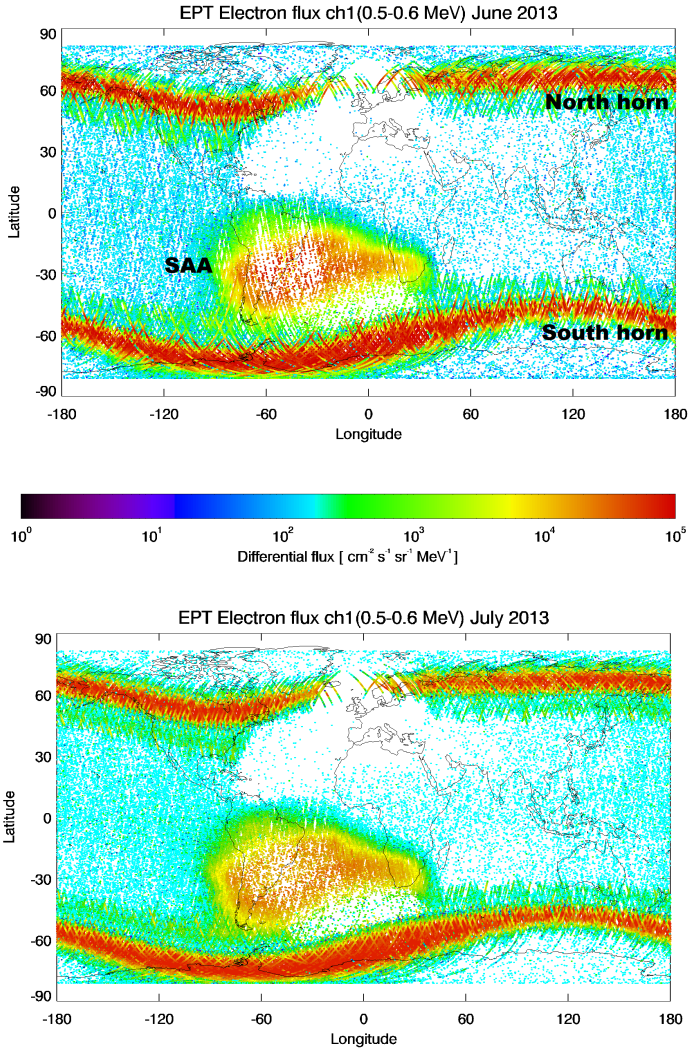

Figure 2.2: Electron flux in channel 1 (0.5-0.6 MeV) over one month of observations. Top panel: June 2013. Here it is possible to see the South Atlantic Anomaly (SAA), as well as the penetration of the outer belt at high latitudes or the so-called 'horns'. Bottom panel: July 2013. The fluxes are higher in June because this month was more geomagnetically active (one SEP and two geomagnetic storms with Dst $< -100\ nT$) than July (only one storm, Dst=-87 nT).

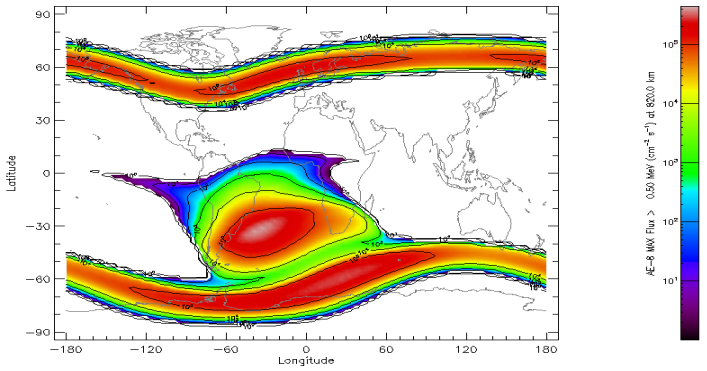

Figure 2.3: AE8-max world map at 820 km for > 0.5 MeV electrons. It is possible to clearly distinguish the north and south horn, and the SAA as well.

fluxes in the SAA are much lower than in channel 1, but for these energies (1-2.4 MeV), the effect of the higher solar and geomagnetic activity is even more pronounced.

Another practical way to show the flux variations and the configuration of the radiation belts is to plot, as a function of L McIlwain parameter (see section 1.4) and time, the flux intensity represented as a color scale. This can be seen in Figure 2.5, which shows electron fluxes as a function of L and time for channel 1 (0.5-0.6 MeV, first panel) and channel 3 (0.7-0.8 MeV, second panel) from 21 May 2013 up to 15 January 2014. A third panel is included to illustrate geomagnetic storms as Dst (Disturbance Storm Time) index (see section 1.1.1).

Only when PROBA-V crosses the SAA, the inner belt ($L < 2.8$) is detected. For electrons, this region is very stable, showing almost no change with time. The opposite is valid for the outer belt, which is much more variable with time, showing variations related with geomagnetic activity.

Particles penetrate at lower L values during geomagnetic storms, characterized by minimum values of the Dst index (third panel in

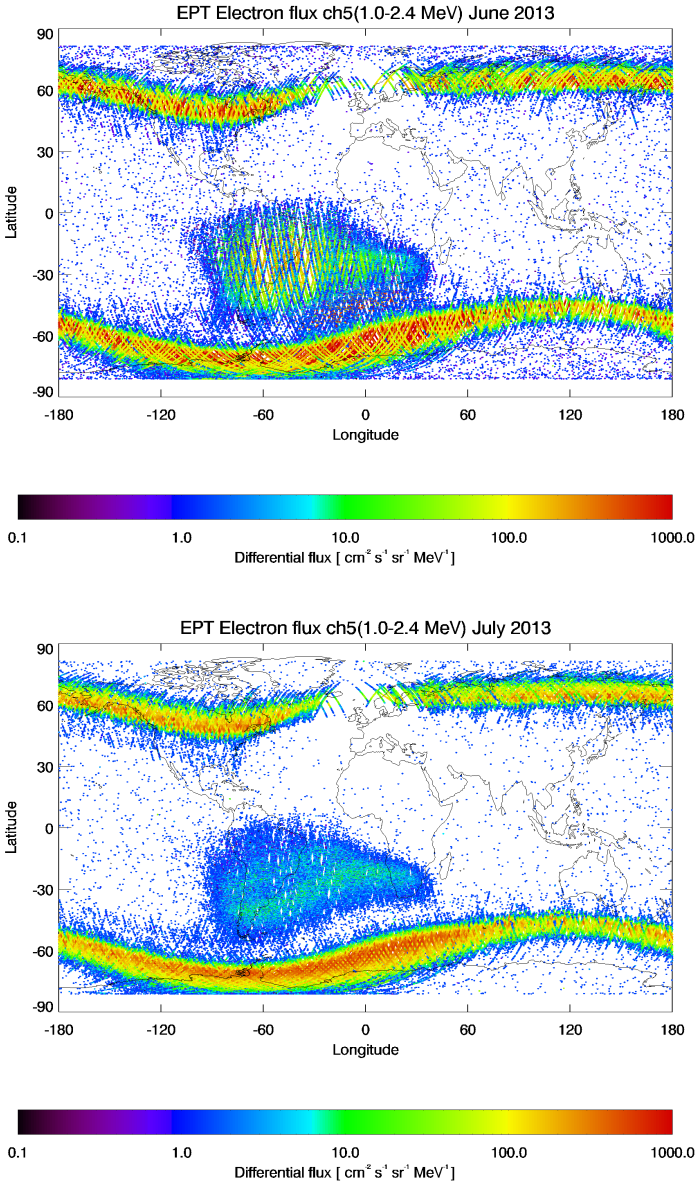

Figure 2.4: Electron flux measured by EPT in channel 5 (1-2.4 MeV) during one month of observations. Top panel: June 2013. Bottom panel: July 2013

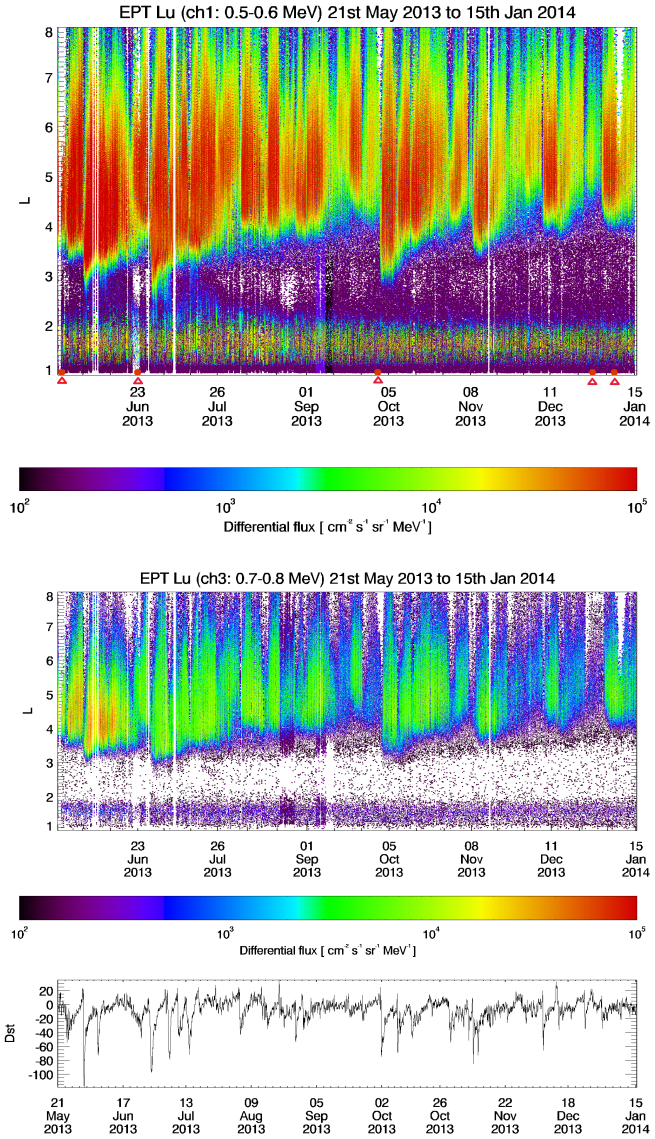

Figure 2.5: EPT electron fluxes from 21 May 2013 up to 15 January 2014 as function of McIlwain L parameter (vertical axis) and time (horizontal axis) for channel 1 (upper panel) and channel 3 (middle panel) using the same color scale. Dst (Disturbed Storm Time) index measured for the same time period is given in the lower panel. Red dots and triangles in the upper panel represent the dates of the SEP events occurred during this period.

Date	Cause	Intensity $[p^+\ cm^{-2}\ sr^{-1}\ s^{-1}]$
22/05/2013	Asymmetric halo	1660
23/06/2013	Coronal Mass Ejection (CME)	14
30/09/2013	CME	182
28/12/2013	CME	29
06/01/2014	Asymmetric halo	42
09/01/2014	Asymmetric halo	1033

Table 2.1: List of SEP events during the studied period (21 May 2013 to 15 January 2014). This information is available at `https://umbra.nascom.nasa.gov/SEP/`

Figure 2.5). Four deep minima of Dst appear during this time period: 1 June 2013 (with the minimum Dst =-119 nT), 29 June 2013 (Dst=-98 nT), 2 October 2 2013 (Dst=-67 nT) and 9 November 2013 (with Dst=-81 nT). It can be seen that during these events electrons were injected, reaching lower L values. As an example, right before the first big storm on 1 June 2013, the outer belt inner boundary was located at $L = 3.4$, but after the injection of particles due to the geomagnetic storm, this inner limit was pushed to $L = 2.7$.

The red triangles on the first panel of Figure 2.5 correspond to Solar Energetic Particle (SEP) events observed since the launch of EPT in May 2013 up to 15 January 2014. Table 2.1 shows some characteristics of these events. During such SEP events, particles emitted by the Sun are accelerated to very high energies due to a solar flare or shocks associated with coronal mass ejections (CME) and arrive to the Earth with speeds close to that of light. The solar plasma associated to a CME can also cause geomagnetic storms a few days later when it reaches the magnetosphere, as for example the case of the CME on 30 September 2013 and the geomagnetic storm on 2 October 2013 (Pierrard et al., 2014). A useful method to validate our data is to compare with other satellites which have

proven the good quality of their measurements. This is the case of the Radiation Belts Storm Probes (RBSP), mainly known now as Van Allen Probes (VAP). Despite the very different orbit (see section 1.9) of these two twin satellites to PROBA-V, the overlap in time, and similar energy channels, allow us to contrast the instruments MagEIS and EPT.

We can see in Figure 2.6 MagEIS data, covering the same time period (21 May 2013 - 15 January 2014) of the EPT data set and similar energy channel at $\sim$ 0.5 MeV. The outer belt shows similar flux variations linked to geomagnetic activity, although electron fluxes are more intense. This was expected since the Van Allen Probes orbit near the equatorial plane. On the inner zone though, it is necessary to be more careful. RBSP fluxes are significantly higher than EPT, however, this is due to background contamination, from energetic inner protons and X-rays generated by electrons interacting with the spacecraft materials (Claudepierre et al., 2015). Due to the novel concept of the EPT design its data don't suffer of similar contamination (Pierrard et al., 2014).

Figure 2.7 shows the comparison made between EPT and GOES15 (Geostationary Operational Environmental Satellites) observations at geostationary orbit, at $6.5 < L < 7$. Channel 1 of EPT (0.5-0.6 MeV) is shown in black versus 10 minutes averaged in situ GOES15 fluxes at 475 keV. The temporal variations are similar, always related with the geomagnetic activity but GOES fluxes are systematically higher, as these data are acquired close to the geomagnetic equator, and because the energy is slightly lower.

2.2.1 Spectra

The particle spectra shows the flux variations as a function of the energy. This is useful to see how the flux changes with energy, and that in general the flux decreases with the energy. It is also possible to fit a theoretical distribution function to this curve and with that also determine certain physical parameters of the particles, like temperature and density.

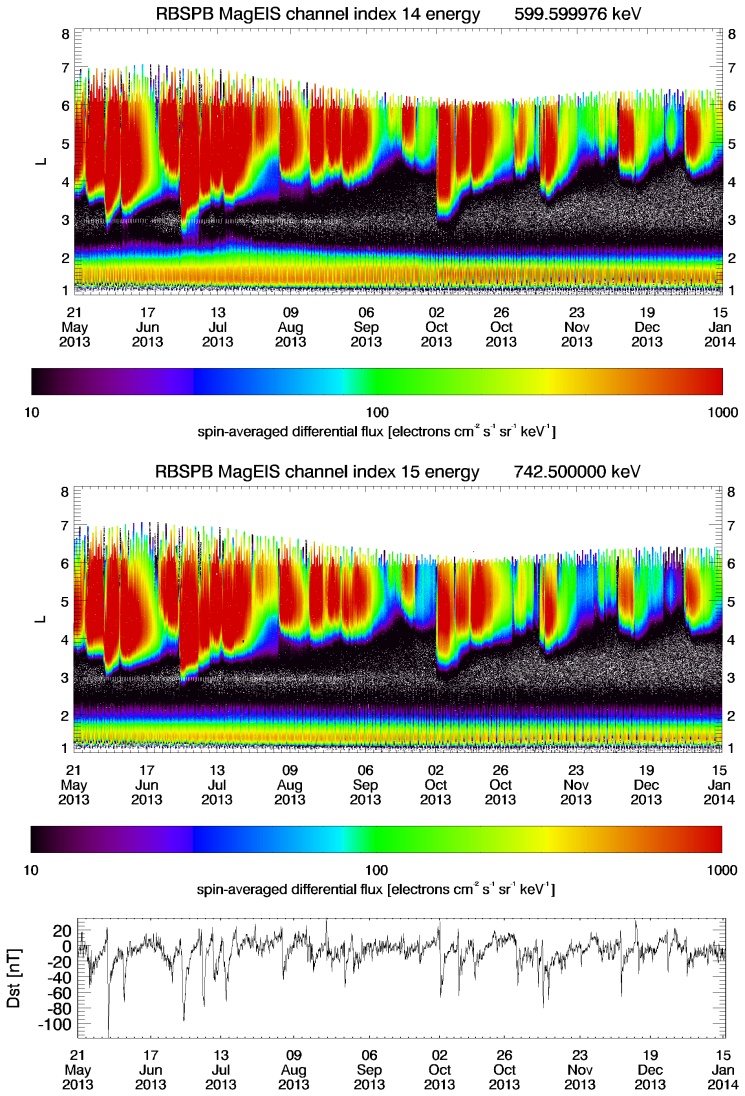

Figure 2.6: Electron fluxes at 600 keV (upper panel) and 742.5 keV (middle panel) in function of L and time from MagEIS observations, from 21 May 2013 to 15 January 2014. Lower panel shows the Dst index for the same time period.

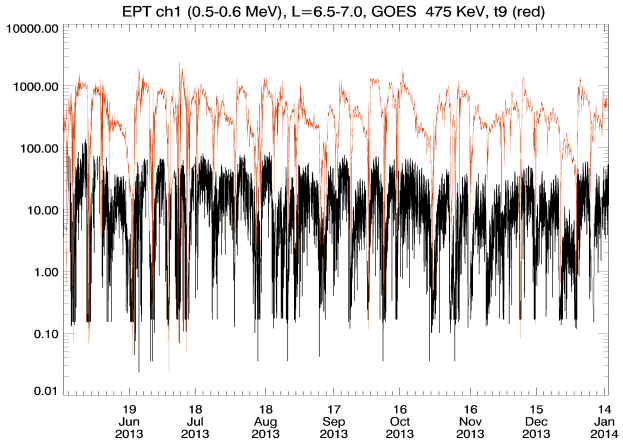

Figure 2.7: GOES15/MAGED (telescope 1) in situ observations for electrons at E=475 keV (red) compared with EPT electrons in channel 1 (0.5-0.6 MeV, in black), for the same time period between $L = 6.5$ and $L = 7$.

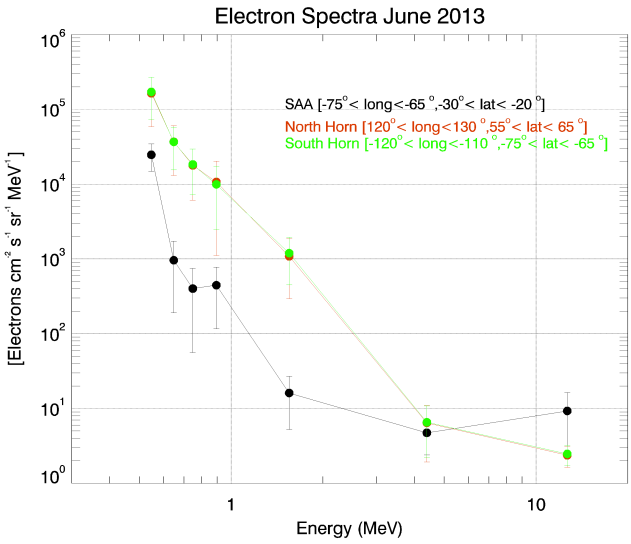

Figure 2.8: Electron spectra during June 2013 for three different locations: South Atlantic Anomaly (black), North horn (red) and South horn (green).

We have computed the spectra for three different locations: the North horn, the South horn and the SAA, during one month of observations, June 2013. This is shown in Figure 2.8. A square of $10° \times 10°$ was used. In the North horn (in red) at $[120° < \text{Long} < 130°]$, $[55° < \text{Lat} < 65°]$, and at $[-120° < \text{Long} < -110°]$, $[-75° < \text{Lat} < -65°]$ in the South horn (in green). The SAA bin (in black) is located at $[-75° < \text{Long} < -65°]$, $[-30° < \text{Lat} < -20°]$.

The spectra in each bin is calculated as the flux average (*mean*) during a month. The error bars are calculated simply as the *standard deviation*, σ.

It is clear from Figure 2.8 that the fluxes in the SAA are much lower than in the horns, except for the last energy channel (8-20 MeV). The spectra of the North and South horn are practically identical, which makes sense because the same L-shell crosses both

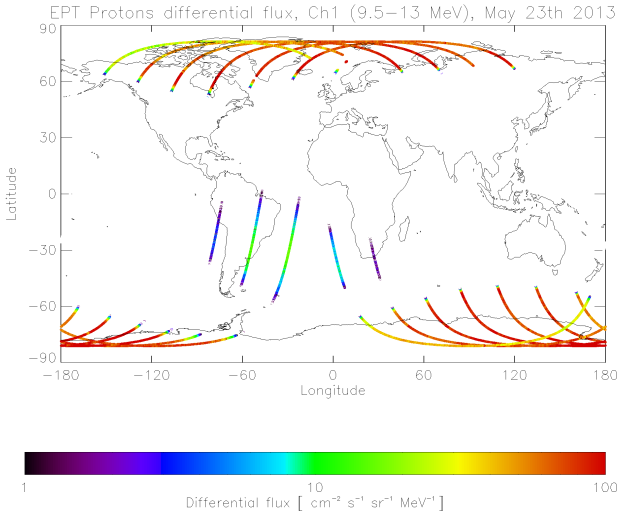

Figure 2.9: Proton fluxes measured in channel 1 (9.5-13 MeV) along the orbit of PROBA-V satellite on 23 May 2013 during the SEP event that started the 22 May 2013.

bins. The fluxes at high latitudes will be always higher than in the SAA.

2.3 Protons

Proton fluxes along one-day orbits of the PROBA-V satellite are generally detected only in the SAA. At high latitudes, the proton fluxes do not penetrate down to 820 km of altitude, except during SEP events. This is illustrated by Figure 2.9 for the SEP of 22 May 2013, which lasted until 23 May. The high latitude fluxes are still detected on 24 May, but they have already decreased.

Figure 2.10 shows the proton fluxes in channel 1 (9.5–13 MeV) observed during one month. The first panel corresponds to June 2013 and the second one to September 2013. The South Atlantic Anomaly is well prominent. High latitude fluxes are only visible

when there is an SEP event, for instance during 23 June (see top panel of Figure 2.10 and 30 September (bottom panel). Sometimes the particles are still visible one day or two after the event. That is why for protons, the orbit of the spacecraft is then well visible for these high latitude fluxes.

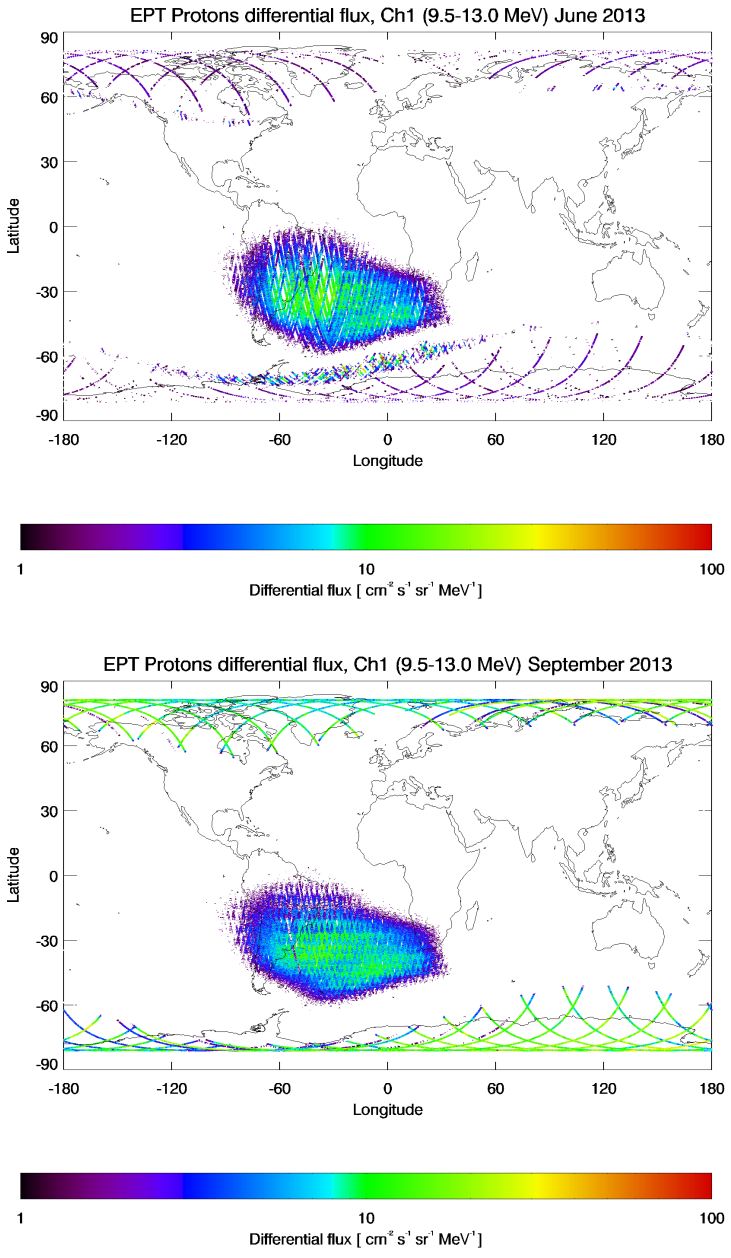

Figure 2.10: Proton flux in channel 1 (9.5–13 MeV) observed during one month of observations. Upper panel: June 2013, lower panel: September 2013

Note the unusual band visible in the Southern hemisphere around $-60°$ (and also partially in the Northern hemisphere around 50° latitude) in June 2013. This band around $-60°$ of latitude is also observed in channels 2 (13-29 MeV) and 3 (29-61 MeV) during the same period of time, but not in the higher energy channels. It is not observed during other months, as shown by the second panel for September 2013.

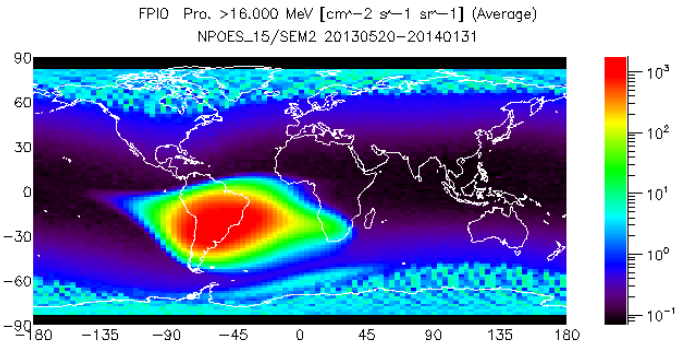

Figure 2.11: POES proton flux for energies higher than 16 MeV from 20 May 2013 up to 31 January 2014 (S. Bourdarie, private communication).

Similar bands have been observed in the standard proton detector of the POES mission (see section 1.9 for more details about the satellite), and have been interpreted as contamination due to energetic outer belt electrons. Figure 2.11 shows the proton map observed by POES on a similar orbit (840 km of altitude, inclination 98°). It shows the omnidirectional flux for protons with energies higher than 16 MeV from 20 May 2013 up to 31 January 2014 (S. Bourdarie, private communication).

This band has also been observed in 2002 by POES, as shown in Figure 2.12, in January. Data from 2002 are the most recent data available for public access.

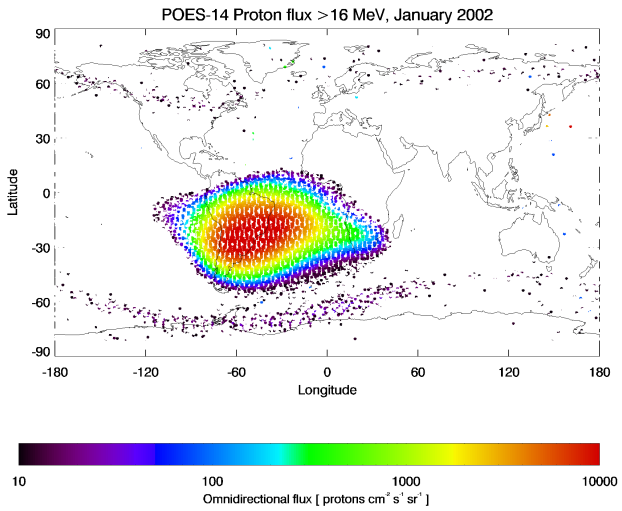

Figure 2.12: Proton flux from POES during January 2002 for E> 16 MeV.

In Figure 2.11, as with EPT, proton fluxes are observed at high latitudes. This is observable only during SEP events. The structure located between the SAA and the South horn appears also in these POES observations, as in EPT during June 2013 after a SEP event. Such band of proton precipitation at higher L in the Southern hemisphere was also reported by Evans et al. (2008) after two SEP events: 1 November and the 10 November 2004. However, the authors stated that a careful analysis of the POES proton data set indicated that the high latitude flux enhancement (Northern and Southern bands) they observed after SEP events in late 2004 and early 2005, was likely due to E $>$ 3 MeV electrons and not due to high energy protons.

With EPT, it is also noted that the appearance of these protons in location and intensity is correlated to the high energy electron flux above 2 MeV. It must be stated that the data until 24 June 2013 has been acquired during the commissioning phase of the EPT, while some tests were still performed in order to find

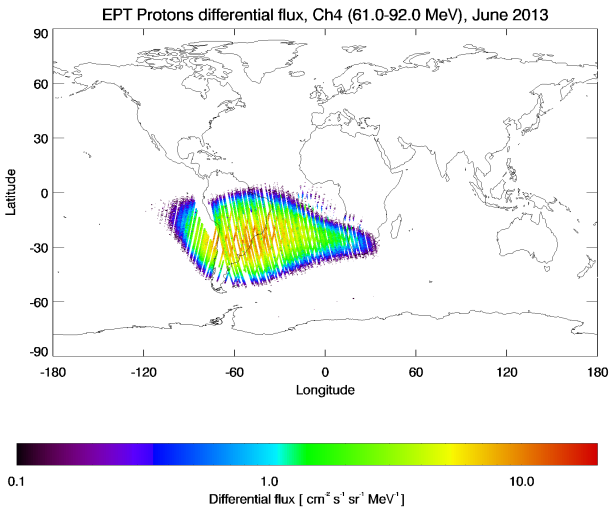

Figure 2.13: Proton flux in channel 4 (61-92 MeV) observed during the month of June 2013, only with pitch angles between 80° and 100°.

its optimal configuration. This means that the energy deposition limits set for each analogue detector S1, S2 and S3 to define the various detection channels, were not yet optimized. While it was definitely observed that with the un-optimized configuration particle type misidentification could occur, contamination under the optimized configuration was found to be extremely negligible, since the channel definition process excluded recording of particles with ambiguous signature. For instance, the EPT identification of particles in the HES, requires cross validation from both the S2 and the S1/S3 sensors (Cyamukungu et al., 2014).

GEANT4 simulations showed that with the unoptimized configuration file, electrons can be registered as 29–61 MeV (channel 3) protons if their energy is above 2 MeV, but it needs a flux of ~ 400 electrons $cm^{-2}\ s^{-1}\ sr^{-1}\ MeV^{-1}$ in the energy range 2.4-8 MeV, to register one event in the corresponding proton channel. At the time of this unusual proton occurrence, sometimes more than 10 counts

could be registered in this proton channel and the highest flux observed for 2.4-8 MeV electrons was around 200 electrons $cm^{-2}\ s^{-1}\ sr^{-1}\ MeV^{-1}$. With the more restricted energy limits for particle identification (configuration file after 24 June 2013), the electron contamination efficiency was calculated to be zero. After optimization of the EPT configuration, no such intense high latitude proton population was observed anymore, but the May 2013 SEP event was also the strongest one during the period between PROBA-V launch and the publication of "The Energetic Particle Telescope: first results"(Pierrard et al., 2014). Figure 2.13 illustrates directional proton fluxes from channel 4 during the month of June 2013 using only the measurements with boresight orientation between 80° and 100°. The omnidirectional flux divided by 4π gives a good estimation (within a factor of about 2) of the proton directional flux for the covered particle pitch angle range (Cabrera et al., 2005). At low altitudes, the high-energy trapped proton fluxes are strongly anisotropic, i.e. proton fluxes depend on their arrival direction in the plane perpendicular to the local magnetic field vector, as well as on their pitch angle. The anisotropy manifests itself through steep pitch angle distributions and the so-called East-West effect: The pitch angle distribution is due to the particle gyration around magnetic field lines and their mirroring in an inhomogeneous magnetic field. The East-West effect is the result of the interaction of the protons with the Earth's magnetosphere. Below 2000 km, the gyroradii of trapped protons with energies above 1 MeV are comparable to the neutral atmospheric scale height[2], which means that during a gyration they encounter different atmospheric densities and this causes differences of a factor of three or more in fluxes arriving from different azimuths (Kruglanski, 1996). Due to the orientation of the

[2]The scale height represents the vertical distance above a planet's surface at which the density or the atmospheric pressure decreases by a factor of e. It is defined as $H = \frac{kT}{Mg}$, where k is the Boltzmann constant, T is the temperature, M is the average atomic mass of the atmospheric particle, and finally g is the gravity. For the Earth $H \approx 8.5km$ at the surface of the Earth.

PROBA-V satellite, dayside measurements correspond to westward fluxes, while nightside measurements correspond to eastward fluxes. Due to their wider pitch angle distributions and the wider field of view the electrons can be assumed almost omnidirectional, at least in first order approximation (Cyamukungu and Grégoire, 2011).

Figure 2.14 illustrates the proton fluxes observed from 21 May 2013 to 15 January 2014 as a function of L (vertical axis) and time (horizontal axis) for channel 1 (first panel) and channel 3 (second panel) using different color scales. The red dots in both panels correspond to the main SEP events. One can see that each SEP event corresponds to the injection of energetic protons on distant drift shells. The particles penetrate the Earth's magnetic field into the polar regions. The injected proton fluxes remain high for several days after the event. Note that after the SEP event of 22 May, particles remain trapped at $L = 4 - 5$ during more than one month (up to July) and form the additional proton belt displayed in Figure 2.10 (upper panel) corresponding to the month of June. There are almost no fluxes outside the SAA from July to 30 September 2013.

2.4 Helium ions

Figure 2.15 illustrates the Helium fluxes observed in channel 1 (38-51 MeV) when accumulated from 16 May to 21 October 2013. Almost no measurable He^{++} ion fluxes are observed on individual orbits except during SEP events, when the fluxes at high latitudes are higher than 0.01 He^{++} cm^{-2} s^{-1} sr^{-1} MeV^{-1}. EPT observations show very low fluxes in the SAA. Figure 2.16 shows that injections of helium ions appeared during the SEP events (again identified by the red dots on the X axis) at $L > 4.5$, but they start to disappear already one day after the event.

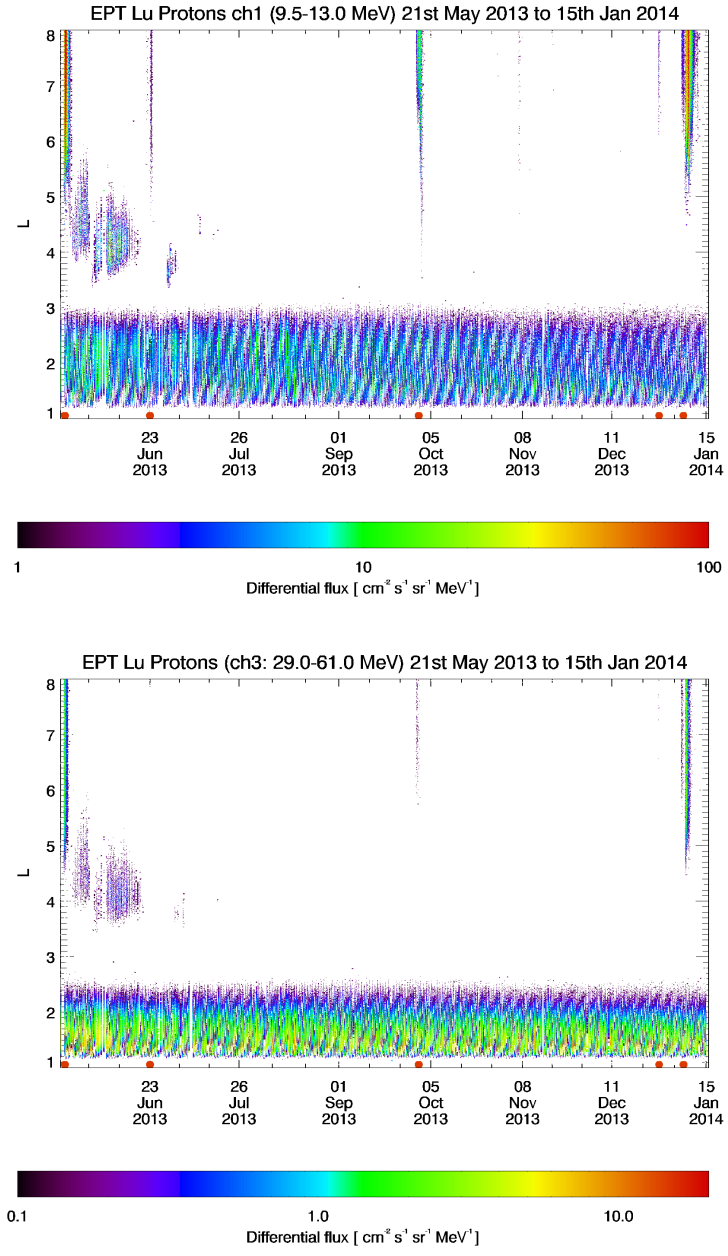

Figure 2.14: Proton fluxes observed from 21 May 2013 up to 15 January 2014, as a function of L (vertical axis) and time (horizontal axis) for channel 1 corresponding to 9.5-13 MeV (first panel) and channel 3 corresponding to 29-61 MeV (second panel). Note that different color scales are used for both panels.

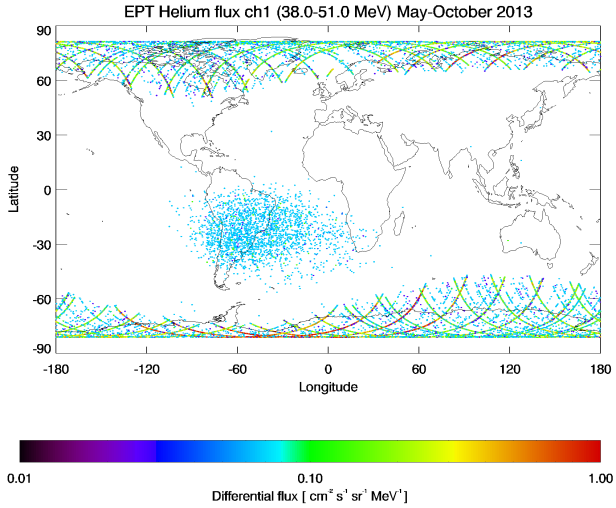

Figure 2.15: Helium fluxes observed in channel 1 (38-51 MeV) when accumulated from 16 May to 21 October 2013.

2.5 Discussion and conclusions

The new spectrometer EPT measures directional fluxes of electrons, protons and heavier ions simultaneously in different energy ranges. This enables us to produce world maps of electron fluxes between 0.5 and 20 MeV, proton fluxes between 9.5 and 300 MeV and helium fluxes between 38 MeV and 1600 MeV. Due to the widely varying fluxes of electrons, protons and heavy ions within the radiation belts, the instrument was designed with a unprecedented in flight particle and energy discrimination capability that provides more precise measurements than those made by previous detectors which have been used in the past to build the AE8, AP8, AE9, AP9 and other empirical radiation belt models. The results of the EPT will now be available for the development of more elaborated statistical models of the space radiation environment. The simultaneity of the

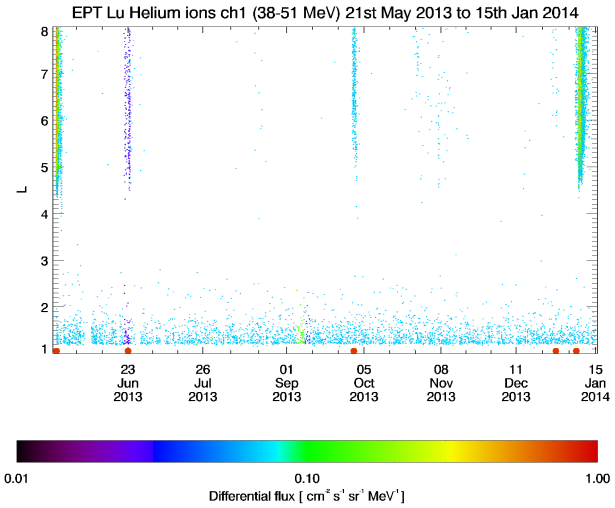

Figure 2.16: Helium fluxes observed from 21 May 2013 to 15 January 2014 as a function of time (horizontal axis) and L (vertical axis) for channel 1.

energetic electron, proton and helium ion flux measurements is also an unprecedented asset of the EPT detector.

First EPT observations show electron, proton and helium ion fluxes in the South Atlantic Anomaly (SAA), as well as at high latitudes, with significant flux enhancements of protons and ions during SEP events in the polar regions. These yet unforeseen enhancement will need further investigations and a proper theory to account for their injection into the radiation belts drift shells. An important difference with the fluxes predicted by the AE8 and AE9 model was found in the magnetically conjugate region of the SAA in the Northern hemisphere where the IGRF magnetic field has a relatively pronounced maximum and where very low fluxes are observed in Figures 2.2 and 2.4. The extension and shape of the SAA is also somewhat different from that predicted by the AE8 and AP8 model in some energy ranges. Indeed, due to the secular variation of the IGRF, the epicenter of the SAA has moved westward at a rate of 0.3°/ year between the early radiation belt measurements in the 60's and the present epoch (Heynderickx, 1996). Flux variations observed by EPT allow us to better understand the dynamics of the radiation belts, especially during Solar Energetic Particle (SEP) events, as well as during other changes of Interplanetary Magnetic Field (IMF) and geomagnetic field. Losses and sources of relativistic electrons in the outer belt (see Section 1.6) have been recently reviewed by Shprits et al. (2008a,b). These source and loss processes are controlled by radial transport, as well as by local acceleration due to different waves. Radiation belt electron precipitation due to whistler waves of ground-based VLF transmitters have also been reported at such low altitudes (Vampola, 1977; Sauvaud et al., 2008). The worldwide distribution of the protons at 820 km altitude can also be determined and modeled from the EPT uncontaminated energy spectra of the electrons, protons, and He^{++} ions collected already since May 2013. Indeed, the instrument provides uncontaminated spectra well discriminated for each particle species unprecedented energy resolution and very good time resolution (2 s). EPT spectra can be compared with AE8 and AP8 mod-

els (Pierrard and Lemaire, 1996; Pierrard and Borremans, 2012) and with the low altitude trapped proton model for solar minimum conditions based on SAMPEX/PET data that was developed some years ago (Heynderickx et al., 1999; Pierrard et al., 2000). There are also other radiation belt measurements from LEO missions (POES, EQUATOR-S, DEMETER, SAC-D,...) which had energetic particle detectors/spectrometers onboard, and that can be cross-calibrated a posteriori using the uncontaminated EPT energy spectra. Significant proton flux enhancements during SEP events are observed by the EPT instrument. It appears definitely from EPT data that the main time variations of proton and helium fluxes at 820 km are associated with SEP events. Relativistic electrons injections are also associated with SEP events (on 23 May and 30 September 2013 for instance), but also with Dst geomagnetic storms. The EPT observations will be used to complete the empirical dynamic model TOP of the space radiations to predict the flux variations during geomagnetic storms at LEO orbit (Benck et al., 2010; Benck et al., 2013). Section 1.10 gives more insight about this model.

Cluster observations have also been analyzed to determine the flux variations during geomagnetic storms. The Cluster spacecraft, as well as RBSP, directly cross the middle of the radiation belts and complete the observations of LEO satellites. Dynamic simulations based on averaged Cluster observations have been developed to give the flux of non-relativistic electrons during quiet and storm time periods. Using simultaneous observations of the Cluster instruments RAPID, CIS and WHISPER, Pierrard and Benck (2012) and Darrouzet et al. (2013) showed also observed links between the position of the plasmapause and the locations of the electron radiation belts boundaries for different energies. Cluster spacecraft continue to provide observations that can be compared with EPT. The two Van Allen Probes launched by NASA in 2012 provide also high resolution measurements in the heart of the radiation belts that are compared with EPT observations. Unlike many solid state detectors used since the 60's to measure the fluxes of

energetic charged particles in the Earth's radiation belts, after the commissioning phase, the energy channels of the EPT are free of contamination from fluxes of other (undesired) types of penetrating particles. This is an advantage of the novel concept on which this new solid state detector/spectrometer is based. In the future, the EPT instrument could be implemented on other spacecraft to measure the space radiation fluxes. As a consequence of the modularity of the EPT instrument, its energy ranges, its sizes, and mass can easily be adapted to the needs of future GEO, GTO, as well as other LEO space missions.

Chapter 3

Geomagnetic Storms

Part of this chapter has been published in **Pierrard and López Rosson (2016)** at *Annales Geophysicae*, Volume 34, Issue 1, 2016, pp.75-84. DOI 10.5194/angeo-34-75-2016. The analysis and the manuscript text presented in this chapter are work of the present author.

3.1 Introduction

As mentioned in Section 1.5, the inner radiation belt is fairly stable, while the outer belt is very dynamic, where the flux of relativistic electrons (of the order of MeV's) can change by several orders of magnitude on timescales from a few hours to a few days. Observations of the outer electron radiation belt often show dropouts, i.e., sudden electron depletions during the main phase of storms, followed by injections occurring at lower radial distances. These changes in the radiation belt flux are driven by the interaction of the solar wind with the Earth's magnetosphere and can occasionally fill-in the slot region (Lemaire et al., 1996). The high energy electrons cause a range of problems for satellites like internal satellite charging effects while protons produce cumulative dose and dam-

age, as well as prompt single event effects. Forecast is thus crucial and needs accurate measurements associated to good understanding of the physical mechanisms associated to the flux variations (Horne et al., 2013).

Note that a third radiation belt was recently observed just after the launch of the two Van Allen Probes for energetic electrons (> 2 MeV), from 2 September 2012 and with a duration of around 4 weeks (Baker et al., 2013). This new belt resulted from a combination of electron losses to the interplanetary medium and scattering by electromagnetic ion cyclotron waves to the Earth's atmosphere (Shprits et al., 2013).

In accordance with recent observations of the Van Allen Probes spacecraft, our results show that the radiation belts are sometimes different from the general feature. During the first half of 2015, several geomagnetic storms have modified the space radiations around the Earth, as described in the present work based on EPT observations.

In the present study, we report the formation of unexpected space radiation hazard appearing after a geomagnetic storm on 17 March 2015 and two other similar events that occurred respectively in January and June 2015.

3.2 Data and analysis of the observations

3.2.1 The 17 March 2015 event

On 17 March 2015, the biggest geomagnetic storm observed by EPT since its launch in May 2013 reached a Dst index of $-223\ nT$. This event is also the biggest storm during the current solar cycle (up to August 2018). The planetary geomagnetic index of Bartels Kp reached 7+.

This event was associated with a sudden increase in solar wind density N, velocity u and interplanetary magnetic field (IMF) intensity B due to a shock created by a coronal mass ejection (CME).

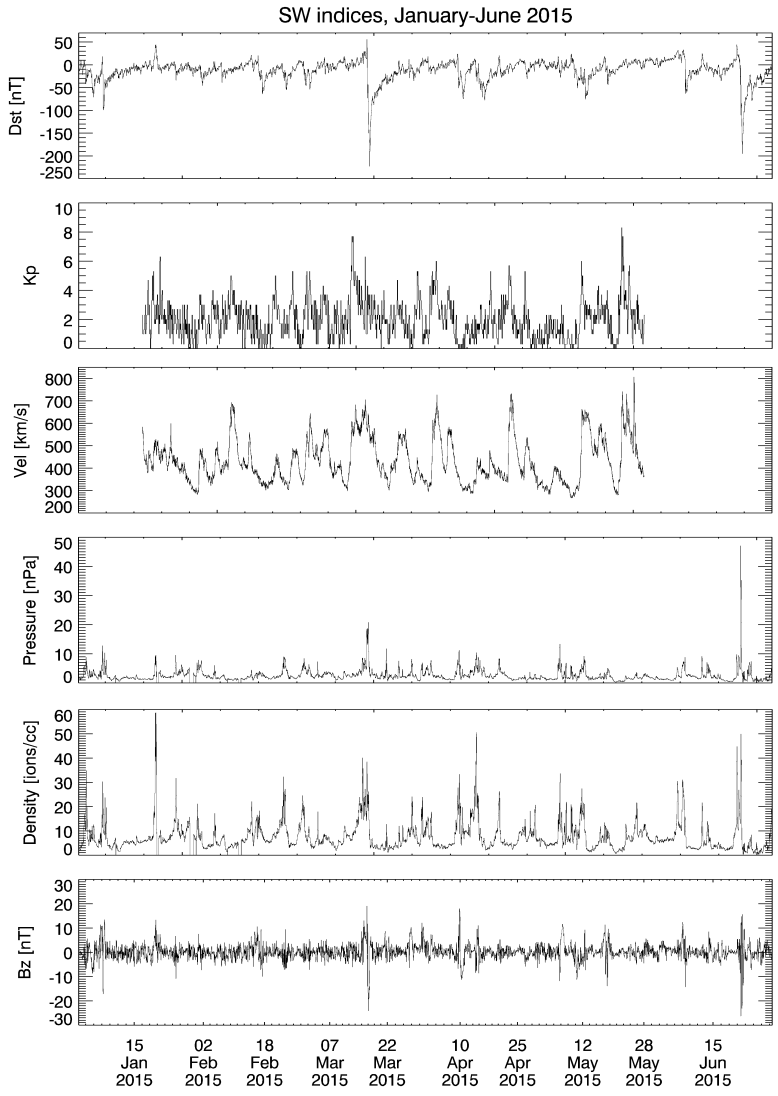

Figure 3.1: Solar wind parameters measured by ACE. From bottom to top: Bz (the z component of IMF in nT), N or the solar wind density, solar wind pressure in nPa, bulk velocity u in $km\ s^{-1}$ and geomagnetic activity indices (respectively Kp and Dst in nT) observed between January to June 2015.

The event occurred because there were two flux increases, caused by two eruptions from the same active region. The first was a long duration C9.1 flare at 29°W longitude location on the Sun with peak time at 15 March 01:25 UT and accompanied by a partial-halo CME with a speed of 712 $km\ s^{-1}$. The second increase follows an M1.2 flare (associated with a type II radio burst and a coronal dimming) at 32°W location on 15 March with peak at 23:22 UT. After the passage of the shock front, solar wind speed continued to increase reaching a peak of over 650 $km\ s^{-1}$ around 10:45 UT on 17 March and a peak of the magnetic field over 35 nT around 13:35 UT. Figure 3.1 illustrates the different parameters of the solar wind, where from bottom to top we find Bz (the z component of IMF in nT), N or the solar wind density in cm^{-3}, the solar wind pressure in nPa, the bulk velocity u in $km\ s^{-1}$, and the geomagnetic activity indices Kp and Dst in nT between January and June 2015. The Bz peak went down to $-27\ nT$ during the CME.

It is important to point that as mentioned in Section 1.1.2, even if the event was very energetic, it didn't reach the threshold to be considered as an SEP event. This is shown in Figure 3.2.

3.2.2 Electrons

The effect of this interplanetary shock caused a major event on geomagnetic activity and in the observations of the electron fluxes of the radiation belts. Figure 3.3 illustrates the electron fluxes observed by PROBA-V/EPT in channel 1 (0.5-0.6 MeV) as a function of the McIlwain parameter L from 28 February to 13 April 2015. One can see the outer belt penetrating down to $L = 2$ after the event, while the inner edge of the outer belt in this energy range is generally located at $L = 3$ before the event. During previous lower geomagnetic events in 2013 and 2014, the outer belt generally did not penetrate at lower L values than 2.7 (Pierrard et al., 2014). On the contrary, during the event of 17 March 2015, high fluxes are observed at radial distances as low as $L = 2$, filling the usual slot region and reaching the inner belt that generally corresponds

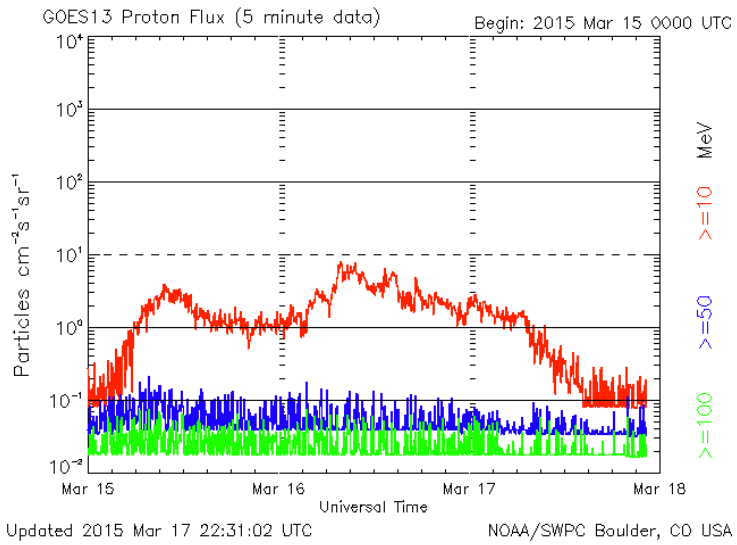

Figure 3.2: GOES13 proton flux for different energies (data from `https://www.solarmonitor.org/`). The threshold for being considered as an SEP events is 10 protons per $[cm^2 s\ sr]$ for energies higher than 10 MeV. This is why the event was not considered as such, but it is clear that it almost reached the limit.

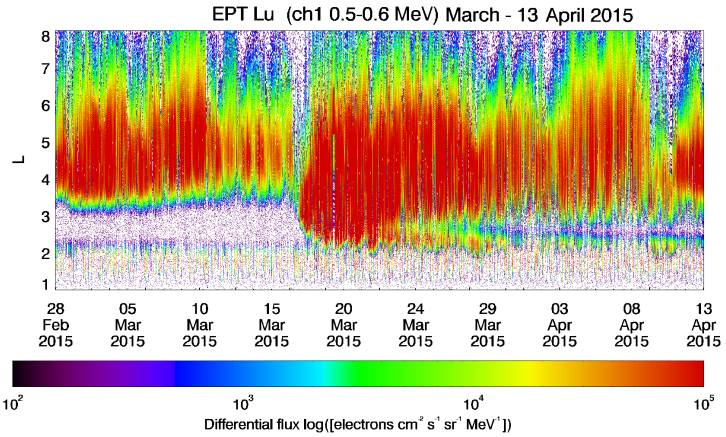

Figure 3.3: Electron fluxes observed by PROBA-V/EPT in channel 1 (0.5–0.6 MeV) as a function of McIlwain L between 28 February and 13 April 2015.

to the crossing of the South Atlantic Anomaly (SAA) at such low altitudes.

A few days after the event (around 23 March), the sector around $L = 2.8$ starts to be gradually depleted for 0.5-0.6 MeV particles, so that a new slot region appears and grows in time. Due to this new depletion localized around $L = 2.5$, the inner and outer belts are again separated, with an upper edge of the inner belt highly more intense at $L = 2.3$ than before the storm. The new electron population trapped at L shells lower than 2.5 remains for more than a month, as its intensity decreases with time. The decay is most likely due to particle interactions with whistler mode hiss waves (e.g. Lyons et al. (1972); Lyons and Thorne (1973); Meredith et al. (2007); Ripoll et al. (2014)) Note that at $L > 4$, the fluxes in the outer radiation belt drop out entirely during the main phase of the storm. Dropouts are commonly observed during storm events (Hudson et al., 1998). As usual, the duration of the dropout is longer at high L values. The fluxes remain low even after the storm has abated in the outer regions, which remain empty dur-

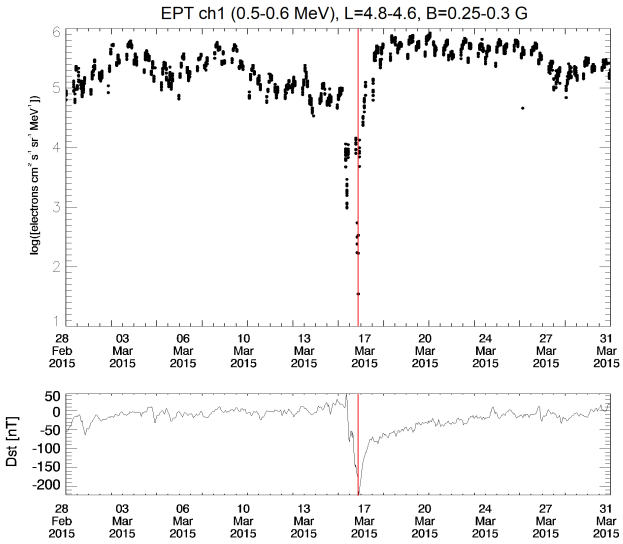

Figure 3.4: Electron fluxes observed by PROBA-V/EPT in channel 1 (0.5–0.6 MeV), in bin $4.6 < L < 4.8$; $0.25 < B < 0.3$G as a function of time between 1 and 31 March 2015. A dropout is clearly visible during the main phase of the 17 March storm.

ing more than 1 day. Figure 3.4 illustrates the fluxes observed in the bin $4.6 < L < 4.8$; $0.25 < B < 0.3$ as an example of flux dropout around $L = 4.7$. The electron flux drops by several orders of magnitude in just a few hours. After the depletion, the flux increases during the recovery phase and is larger a few days after the storm than before. Such a flux increase is generally observed after dropouts, but not always (Reeves et al., 2003). Sudden electron depletion observed during storm's main phase seems primarily a result of outward transport or an adiabatic change (Dst effect) rather than loss to the atmosphere (Turner et al., 2012). Note that a similar behavior is also observed in higher channels of EPT.

Figure 3.5 illustrates the electron fluxes observed by EPT in channel 5 (1–2.4 MeV) as a function of L between 28 February and 13 April 2015. At these energies, high electron fluxes reach $L \sim 2.8$

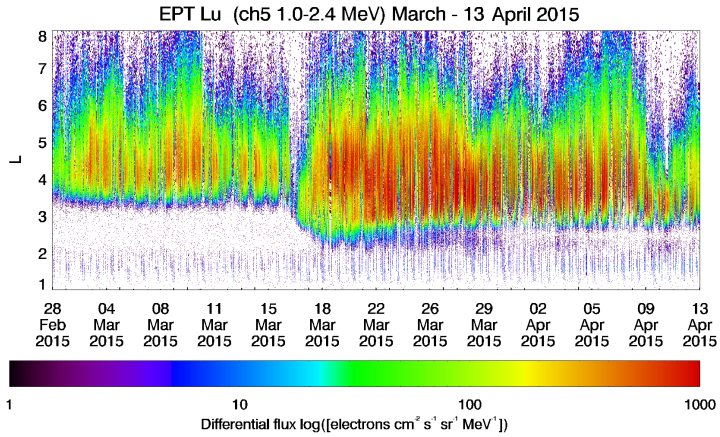

Figure 3.5: Electron fluxes observed by PROBA-V/EPT in channel 5 (1-2.4 MeV) as a function of L between 28 February and 13 April 2015.

but lower fluxes penetrate down to $L \sim 2.2$. The low flux level represents a new population that decays from 20 March to 1 April 2015, until the slot has been formed below $L < 2.8$. But, referring to the pre-storm period, between 28 February and 17 March, we can see the slot can be high up to $L \sim 3.4$ for these energies. Again, we are probably witnessing the scattering of 1-2 MeV electrons by hiss waves, occurring between $L \sim 2.3$ and $L \sim 3.4$, as the combination of L and energy suggests, in agreement with theory (cf. Figure 6 in Meredith et al. (2007); or Figure 9 in Ripoll et al. (2014)). The slot position, as well as the belt position, are energy dependent.

Figure 3.6 shows EPT measurements of the electron fluxes in channel 6 (2.4–8 MeV) as a function of L between 28 February and 13 April 2015, and the Dst index for the same period. The fluxes penetrate a little bit deeper on 18 March than before the storm, but it is limited to $L = 2.8$. This threshold was recently reported as an impenetrable barrier to ultra-relativistic electrons by Baker et al. (2014).

The two NASA satellites Van Allen Probes (VAP or RBSP, see

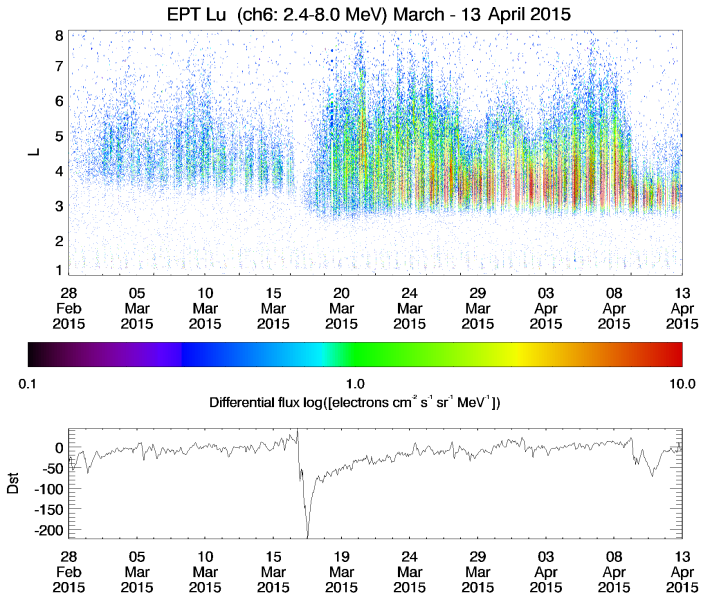

Figure 3.6: EPT electron fluxes in channel 6 (2.4–8 MeV) as a function of L between 28 February and 13 April 2015, and Dst index for the same time period.

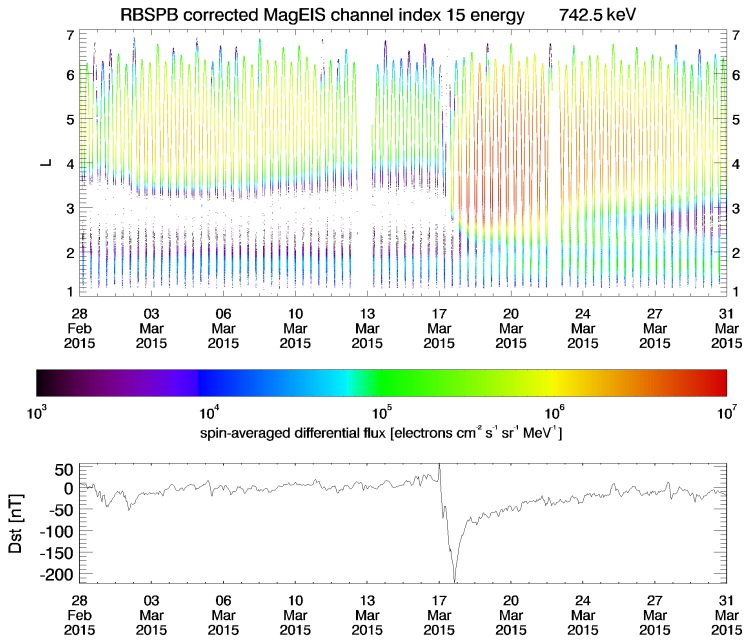

Figure 3.7: Corrected electron fluxes observed in channel 742.5 keV of Van Allen Probe/MagEIS as a function of L between 28 February and 31 March 2015.

Section 1.9 for more details) A and B also provide observations of the radiation belts at the same time. The orbits are quite different since RBSP circulate close to the equatorial plane ($i = 10°$, see Section 1.9 for more details) while the orbit of PROBA-V is polar and LEO (820 km). A comparison with Van Allen Probe B/MagEIS is illustrated in Figure 3.7 (RBSP-A gives almost the same result). We use the MagEIS data corrected from proton contamination that appeared mainly at $L < 2$ in the inner belt (Claudepierre et al., 2015; Li et al., 2015). The resolution obtained with EPT is higher than with RBSP because PROBA-V has a period of 101 minutes and thus crosses the radiation belts more than 14 times per day while the orbital period of RBSP is 9 hours.

At the energy of 742.5 keV, one can see the penetration of higher fluxes just above the inner belt. As observed with EPT, particles injected during the storm reached the inner belt, and filled up the slot region, staying trapped there for a week. Then, the belts started to slowly recovered. At the beginning the slot region is located around $L \sim 2.5$ to later go to its original configuration around $L = 2$ and $L = 3.5$ for electrons with energy higher than 0.6 MeV.

Few electrons of energies from 0.6 MeV to 1 MeV penetrate at such low radial distances of $L = 2.3$ during the event of 17 March. Nevertheless, the few electrons that penetrate at these low L-shells have the same behavior as for channel 1 of EPT: they are lost around $L = 2.8$ in the slot region. The others remain trapped and contribute to feed the inner belt during at least 1 month with a slightly decreasing flux at the outer edge of the inner belt.

3.2.3 Electron spectra

The electron spectra observed in two different (L, B) bins [1] are illustrated in Figure 3.8 for 16 March, the day before the storm,

[1] Similarly to what is done in Chapters 2 and 4, the spectra in each bin is calculated as the daily flux average or arithmetic mean, and the error bars are the standard deviation.

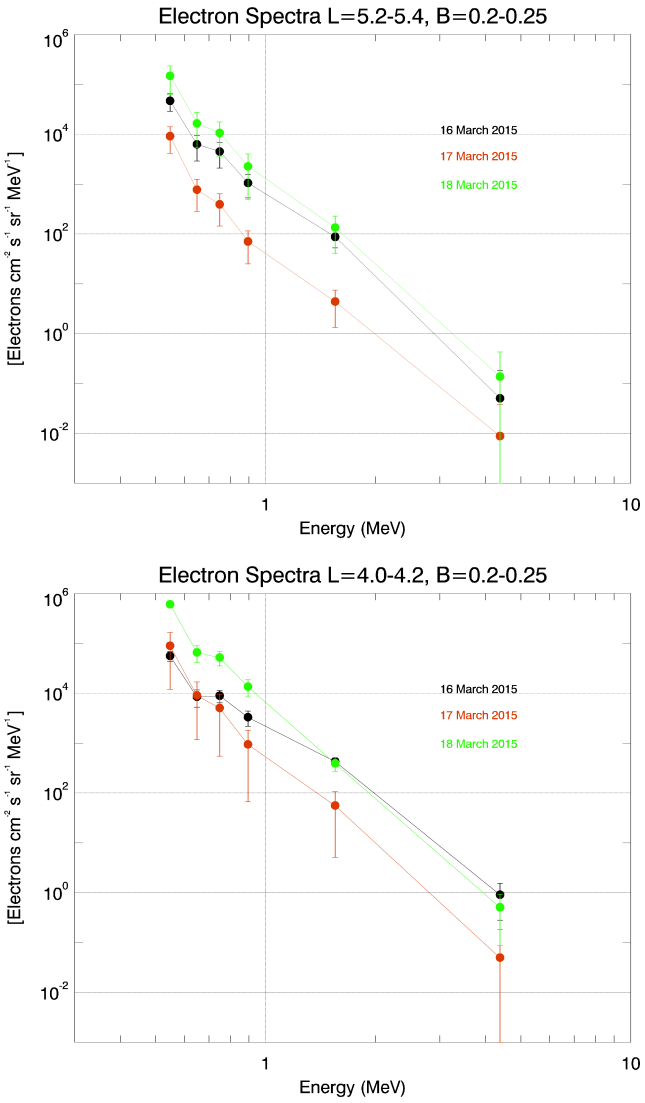

Figure 3.8: Spectra for two different (L, B) bins observed by EPT on 16, 17 and 18 March 2015, corresponding respectively to the day before, during and after the storm. The upper panel shows the bin $L = 5.2-5.4$, $B = 0.2-0.25$. The lowest fluxes are observed during the storm, but for the 3 days, the spectra shape is the same. The bottom panel shows the bin $L = 4.0 - 4.2$, $B = 0.2 - 0.25$. For this bin, 17 March has also the lowest fluxes, but only the energies > 0.8 MeV show a dropout.

for 17 March when the storm occurred and for 18 March, the day after the storm. The upper panel shows the bin $L = 5.2 - 5.4$, $B = 0.2 - 0.25$. We see clearly that the lowest fluxes were observed during the storm on 17 March (dropout), and that the highest fluxes are observed after the storm on 18 March. But for the 3 days, the spectra shape is the same so that the depletion and flux increase are similar for the different energy ranges. The bottom panel shows the bin $L = 4.0 - 4.2$, $B = 0.2 - 0.25$. For this bin, 17 March has again the lowest fluxes, but the lowest energy channels (< 0.8 MeV) are almost not depleted. The flux increase after the storm is on the contrary, similar for all the different energy ranges. Studies of other storms confirm that the dropout mainly concerns the energetic electrons and primarily at high L. Note that the spectra show a nearly power-law shape instead of an exponential spectrum at high energies. The non-Maxwellian shape and the presence of different populations with different energies was already deduced earlier from AE8 electron spectra (Pierrard and Lemaire, 1996) in the radiation belts and even for protons with AP8 spectra (Pierrard and Borremans, 2012). The spectra vary with time so that the shape is different from one time to the other.

Flux variations observed by EPT as a function of Dst events will be used to complete the dynamic empirical TOP model of electron fluxes developed on the basis of averaged flux increase and decay times after storms observed in different (B, L) bins and for different energies by the LEO satellites SAC-C and DEMETER (Benck et al., 2010; Benck et al., 2013).

3.2.4 World maps

World maps are also useful to illustrate LEO observations. Figure 3.9 shows the map of the electron fluxes observed in channel 1 by EPT from 15 February to 15 March 2015 (before the event). While the inner belt corresponded only to the crossing of the SAA in 2013 and 2014 (see especially Pierrard et al. (2014)), this is not anymore the case in February 2015: The presence of a thin belt appears at

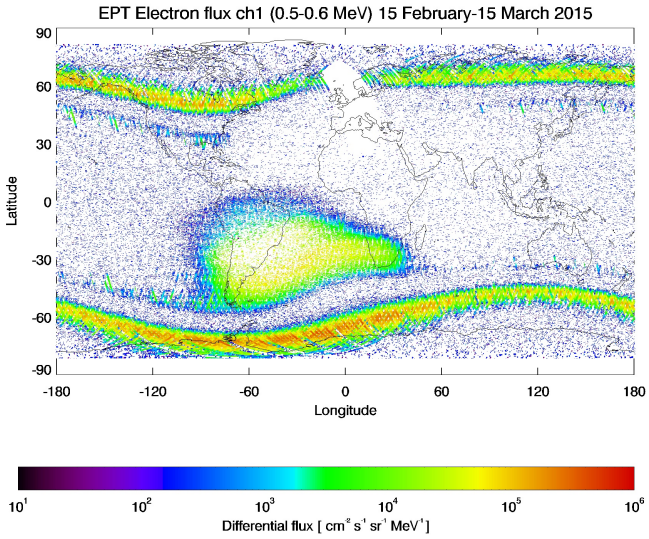

Figure 3.9: Map of the electron fluxes observed by EPT in channel 1 (0.5-0.6 MeV) between 15 February and 15 March 2015 (before the event).

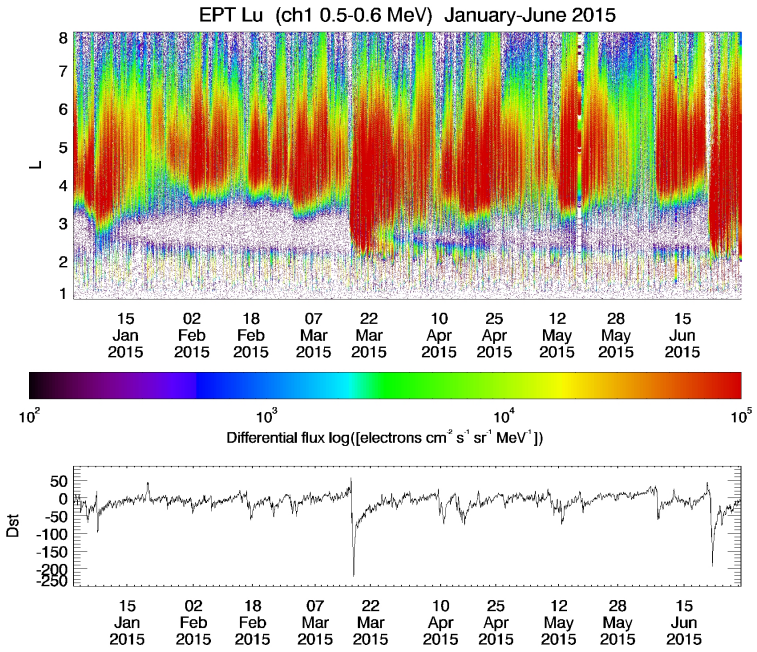

Figure 3.10: Channel 1 (0.5-0.6 MeV) EPT electron fluxes as a function of L between 1 January and 30 June 2015. Bottom panel shows the Dst index during the same period.

$L = 2.3$ at all longitudes in the Northern and Southern Hemispheres at 820 km of altitude. This thin belt is not visible in other channels before the 17 March 2015 event .

It can be verified in Figure 3.10 that this thin belt was created by another storm with a minimum Dst of -99 nT appearing on 7 January 2015. This storm injected some electrons of $0.5 - 0.6$ MeV in the inner belt, and this belt was then visible at all longitudes at 820 km up to the event of March 2015 with a decreasing intensity. Note that another event on 23 June 2015 reached -195 nT and also injected electrons in the slot region.

Figure 3.11 shows the fluxes measured in channel 1 from 16 March to 13 April 2015 after the mid-March storm: The fluxes in

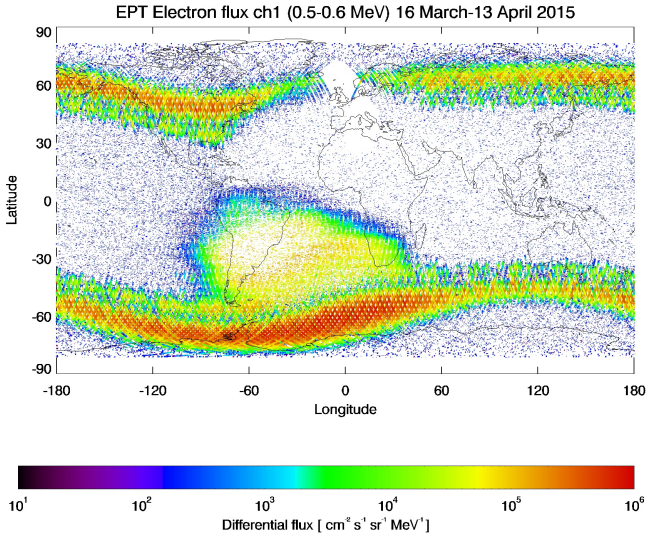

Figure 3.11: Map of the electron fluxes observed by EPT in channel 1 (0.5-0.6 MeV) between 16 March and 13 April 2015 (after the event).

the outer belt have highly increased and reached the inner belt. The fluxes are very high in the outer belt, much more than before the event (see Figure 3.9) and they come closer to the SAA. The new slot appearing after 15 days is also clearly visible.

Figure 3.12 shows the same map but starting 10 days after the storm. The fluxes in the outer belt have been reduced and the new slot region is more visible. The new slot region, appearing here after typically 10 days, is believed to be a result of enhanced precipitation losses of energetic electrons due to their interactions with whistler waves in the magnetosphere (e.g. Lyons et al. (1972); Lyons and Thorne (1973); Glauert and Horne (2004); Fung et al. (2006); Meredith et al. (2007); Sauvaud et al. (2008); Ripoll et al. (2014)). Shprits et al. (2008a,b) have reviewed the different sources and loss mechanisms determining the dynamics of the outer belt for relativistic electrons, which are also explained in Section 1.6.

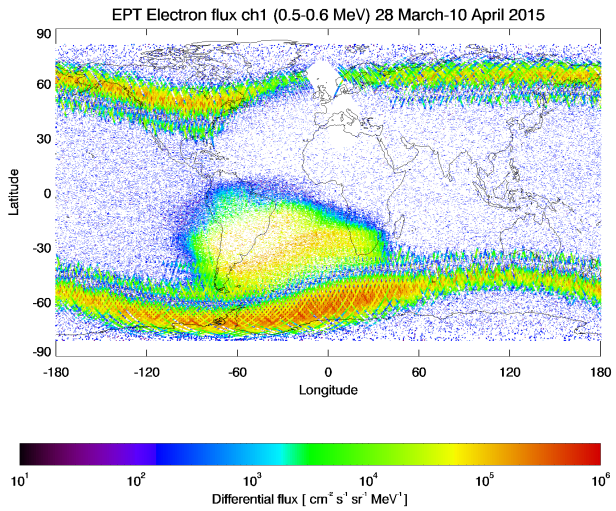

Figure 3.12: Map of the electron fluxe measured by EPT in channel 1 (0.5-0.6 MeV) from 28 March up to 10 April 2015 (10 days after the event).

3.2.5 Protons

Because EPT has a very good discrimination between the particle species, it is very interesting to investigate what happens to the protons during the same period of time.

Figure 3.13 shows the proton fluxes observed by PROBA-V/EPT in channel 1 (9.5-13 MeV) as a function of L from 1 January up to 30 June 2015. One can see protons suddenly injected and penetrating at high L values due to the event. This happened already on 15 March 2015 because the (almost) SEP event appeared before the geomagnetic storms associated to the CME. Sudden high-latitude proton fluxes appear also during the event of June where the injections were even stronger: longer in time and with higher fluxes. Such injections of energetic protons at high latitudes appear when there are SEP events (Pierrard et al., 2014). In June, three SEP events were observed on 18, 21 and 26 June 2015, and only these

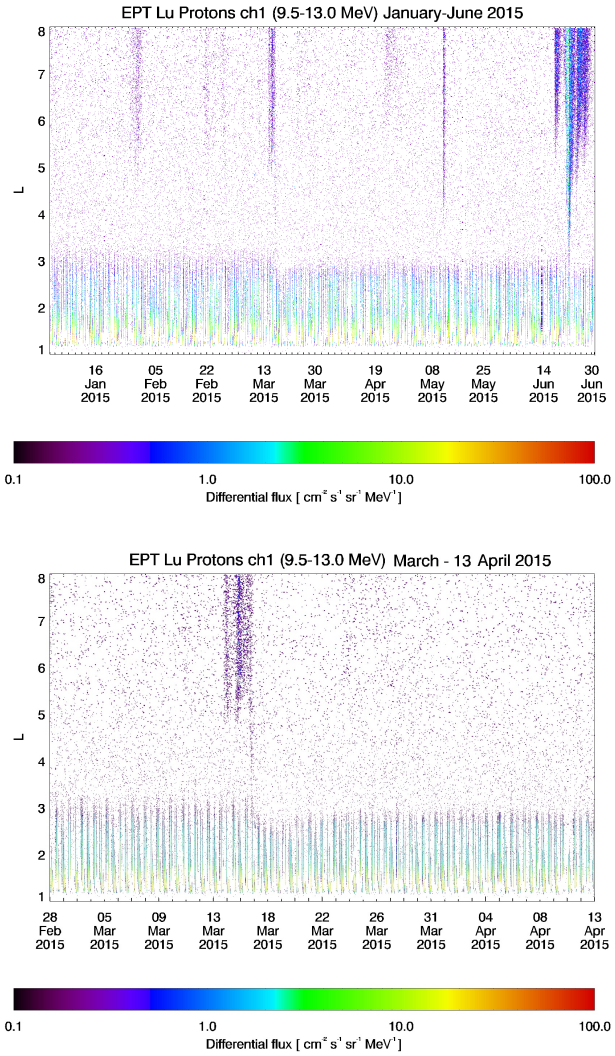

Figure 3.13: Proton fluxes observed by EPT in channel 1 (9.5–13 MeV) as a function of L between 1 January and 30 June 2015 (upper panel) and focused between 28 February and 13 April 2015 (bottom panel) to emphasize that the March proton injection starts on 15 March 2015 due to the arrival of solar energetic protons (SEP event).

events of June inject also protons of higher energies visible in channel 2 (13–29 MeV). Note nevertheless that the injected proton fluxes are generally very low (see the color scale). The SEP event of 15 March 2015 reached a solar flux of 8 particles $cm^{-2}s^{-1}sr^{-1}$ for energies higher than 10 MeV, which is just below the threshold to be considered as a full SEP event.

In addition, we can see that after the event, the extent of the inner belt (corresponding to the crossing of the SAA at this low altitude of 820 km) is slightly reduced, with an extension of the inner belt decreasing from $L = 3$ to $L = 2.8$. Similar injections are not observed at the higher energy channels (except for channel 2 in June), neither for the helium ions.

Figure 3.14 shows the proton map observed by EPT in channel 2 (13-29 MeV) between 16 March and 13 April 2015. The proton shape of the SAA is similar to the low energy electron SAA illustrated in Figure 3.9, but a little less extended (for instance above the Pacific Ocean).

3.2.6 5 years of EPT observations

Since the launch of PROBA-V on 13 May 2013, EPT has provided excellent quality data almost non stop (except for the recalibration period between 27 June 2014 to 15 September 2014) during the last 5 years. The next figures show electrons and protons in function of L and Dst index between 21 May 2013 to 1 January 2018. Using these 5 years of data we confirm our previous results: we see the penetration of low energy electrons at lower altitudes during geomagnetic storms. When these storms are very intense, even the slot region can be filled up and electrons can reach also the inner belt, as shown in the upper panel of Figure 3.15, for electrons of 0.5-0.6 MeV. For relativistic electrons (energies $\geqslant$ 1 MeV) only a few events show particles penetrating to the inner belt (see middle panel of Figure 3.15). Figure 3.16 show even higher energy electrons ($>$ 2.4 MeV) where there are no electrons lower than $L = 3$, although the fluxes in the outer belt almost always increase after a

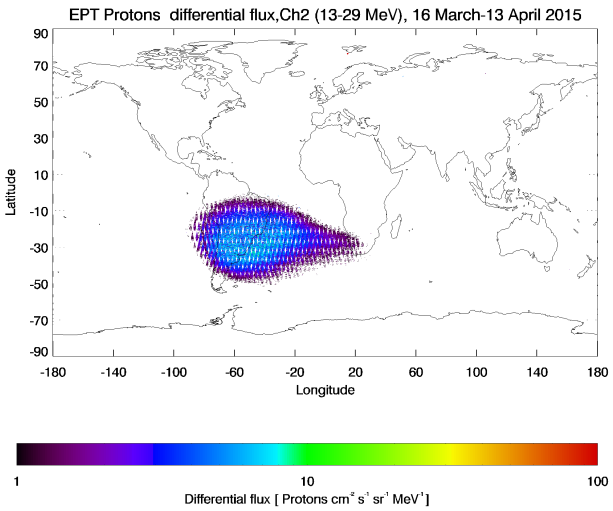

Figure 3.14: Map of the proton fluxes observed in channel 2 by PROBA-V/EPT from 16 March until 13 April 2015.

medium geomagnetic storm (Dst < -70). For protons (see Figures 3.17 and 3.18) the trend is also the same as previously observed: particle injections at high L values during SEP events (red dots on the figures). For high energies (> 92 MeV) there are no protons at $L > 2$.

3.3 McIlwain L parameter and the plasmapause

As described in Section 1.1, the plasmasphere is a torus shaped region of dense and cool plasma (energies of a few eV and densities around 10 to 10^4 cm^{-3} (Darrouzet and De Keyser, 2013)). Its boundary layer is the plasmapause.

It has been suggested by several authors that the plasmapause location (see Figure 1.1) is related with the radiation belts position (see for instance Li et al. (2006); Pierrard and Benck (2012);

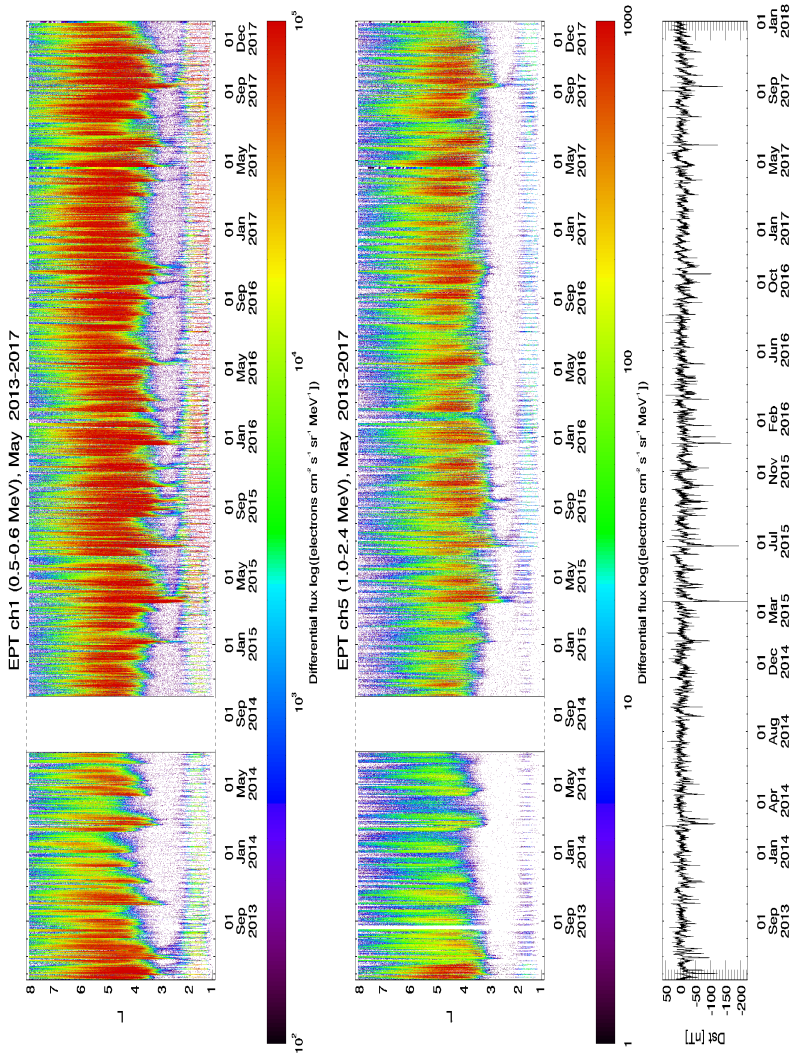

Figure 3.15: EPT electron fluxes: upper panel, in channel 1 (0.5-0.6 MeV) from 21 May 2013 to 1 January 2018. The middle panel shows channel 5 (1-2.4 MeV). The Dst index is also shown in the lower panel for the same period.

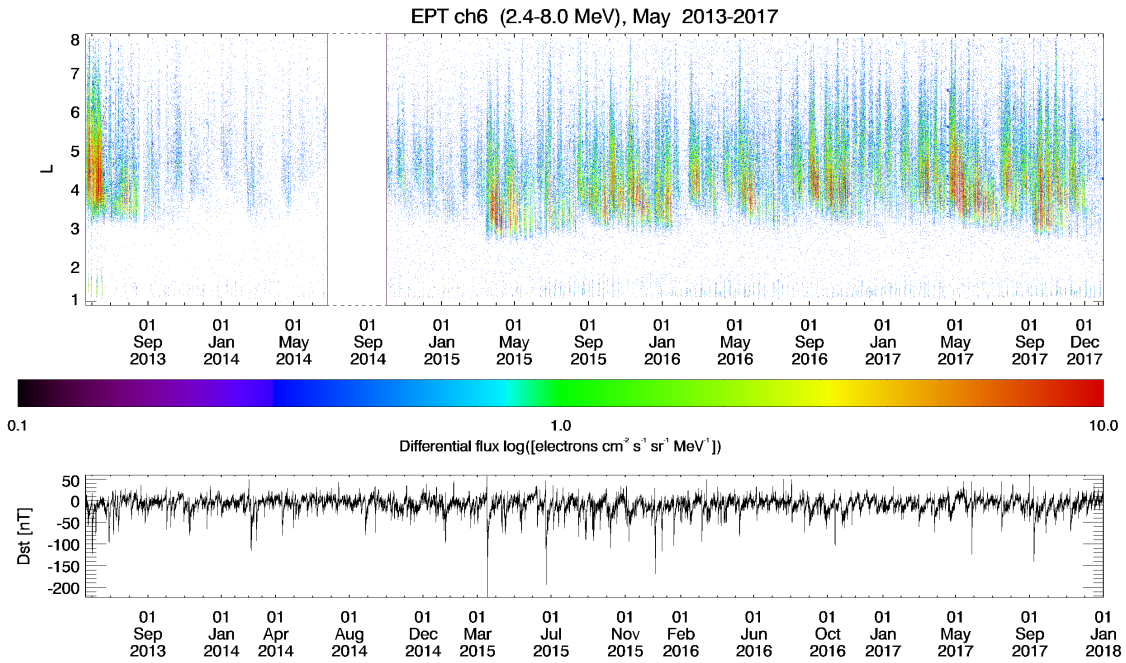

Figure 3.16: EPT electron fluxes in channel 6 (2.4-8 MeV) from 21 May 2013 to 1 January 2018. Dst index is also shown for the same period.

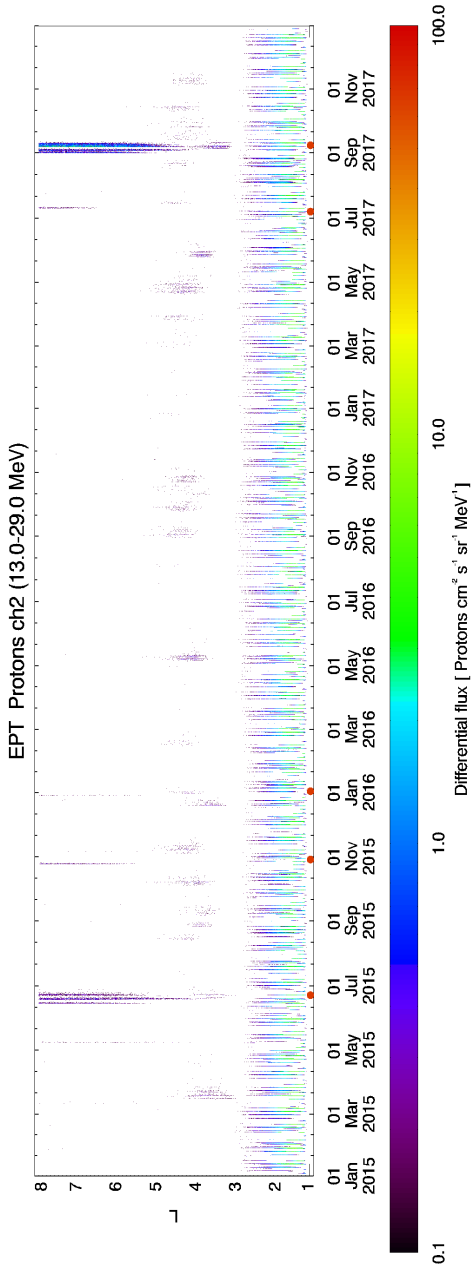

Figure 3.17: EPT proton fluxes in channel 2 (13-29 MeV) from 1 January 2015 to 1 January 2018. Red dots mark the SEP events.

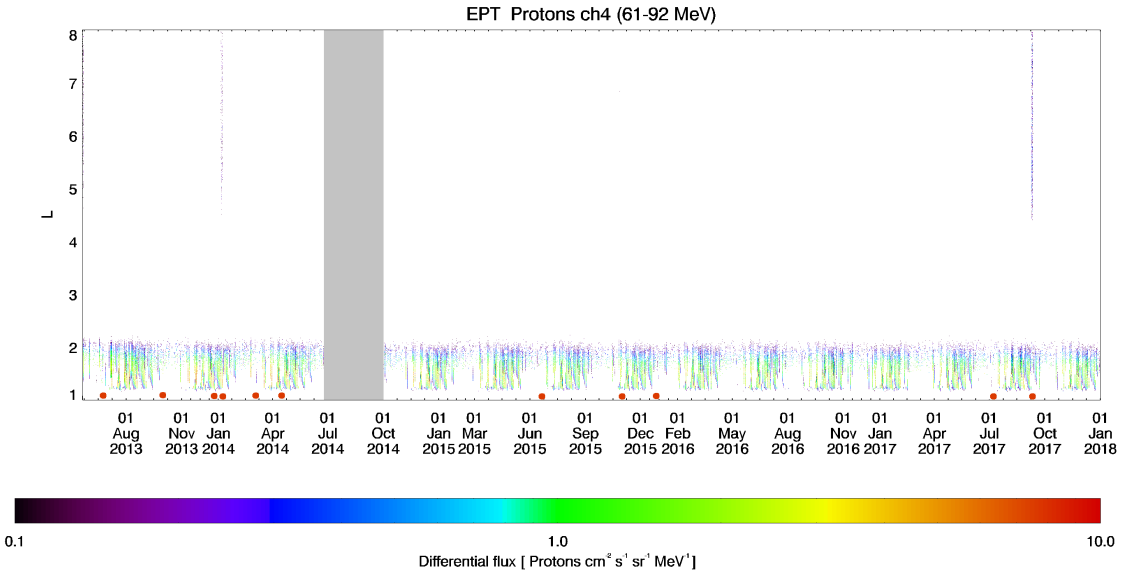

Figure 3.18: EPT Proton fluxes in channel 4 (61-92 MeV) from 21 May 2013 to 1 January 2018.

Darrouzet et al. (2013)), and it can be calculated using different geomagnetic indices, like Kp or Dst.

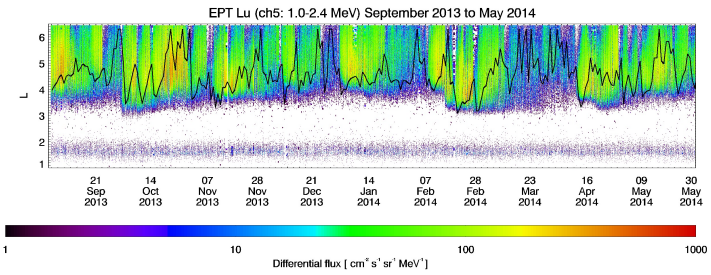

Figure 3.19: EPT electron fluxes for channel 5 (1.0-2.4 MeV). The black curve represents the plasmapause location calculated as a function of Dst index, according to equation (3.1), from O'Brien and Moldwin (2003).

Baker et al. (2014) derived the plasmapause location from spacecraft potential measurements. They cited Li et al. (2006), "Correlation between the inner edge of of outer radiation belt electrons and the innermost plasmapause location", who used the model developed by O'Brien and Moldwin (2003) to study the plasmapause location. Considering the same model, the next equation will be used to calculate the plasmapause location and compare it with EPT data:

$$L_{pp} = 6.3 - 1.57 \log_{10} |Dst_{min}| \tag{3.1}$$

This is shown in Figure 3.19: EPT electron fluxes in function of time and L for channel 5 (1.0-2.4 MeV), and the black curve represents the plasmapause location determined with O'Brien and Moldwin (2003) model, or equation (3.1).

The Dst_{min} corresponds to the minimum value of the Dst index during the previous day. If we assume that Baker et al. (2014) plasmapause location derived from spacecraft potential is similar to the result obtained with equation (3.1), then we can compare

with EPT, as we have done in Figure 3.20. If we look at both plots, the location of the plasmapause seems to oscillate around $L = 4$ and higher values, but the shapes do not look very similar. It is important to mention that the temporal coverage of both plots is not the same. This is because Van Allen probes study was made using data between September 2012 until 1st May 2014, while EPT was not in orbit yet during most part of this period. Between September 2013 and beginning of May 2014 both satellites overlap but considering the fluxes are very low, it is difficult to make a conclusive comparison.

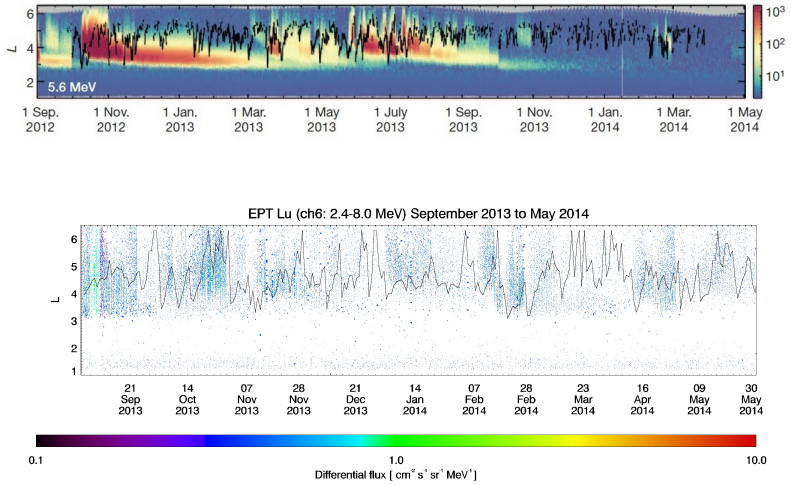

Figure 3.20: Plasmapause location comparison of Van Allen Probes (5.6 MeV, top panel from Baker et al. (2014)) and EPT electrons (2.4-8 MeV, bottom panel), using the equation derived by O'Brien and Moldwin (2003) as function of Dst index.

Because this comparison is not very satisfactory, we can also consider the definition of plasmapause location suggested by Carpenter and Anderson (1992), based on the Kp index, which is:

$$L_{ppi} = 5.6 - 0.46 Kp_{max} \tag{3.2}$$

where Kp_{max} is the maximum value of the Kp in the preceding 24 hours.

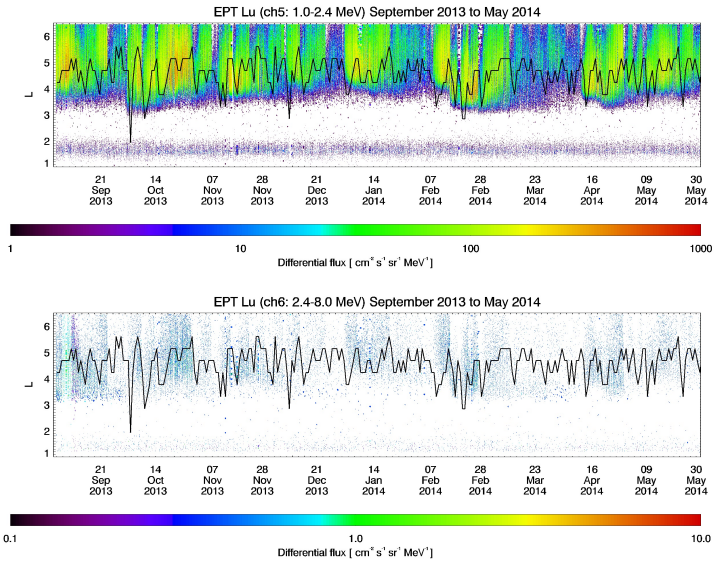

Figure 3.21: Plasmapause location computed using Kp index as presented by Carpenter and Anderson (1992), superimposed on EPT electron channels 5 (1.0-2.4 MeV) and 6 (2.4-8.0 MeV).

In Figure 3.21 is shown our calculation of the plasmapause done with equation (3.2), superimposed on EPT electron channels 5 (1.0-2.4 MeV), upper panel, and 6 (2.4-8.0 MeV) at the bottom panel.

It is easier to compare both methods if we plot them together superimposed on the EPT data. This was done in Figure 3.22, for energies between 1.0 to 2.4 MeV (channel 5) and 2.4 to 8.0 MeV (channel 6). In black it is shown Carpenter and Anderson (1992) prediction based on Kp while in red is the O'Brien and Moldwin (2003) calculation using Dst. In general the results appeared to be more different than expected. Certainly the dates when the plasmapause location changes seem to be the same, but the curve shapes are different. Note also that the Dst method always shows

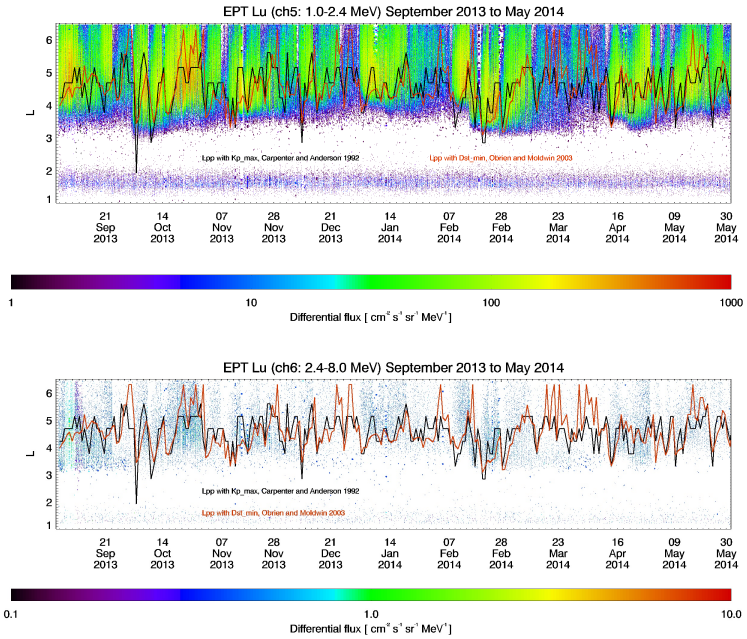

Figure 3.22: Plasmapause location plotted with channels 5 (1.0-2.4 MeV, upper panel) and 6 (2.4-8.0 MeV, lower panel) of EPT. In red is the calculation performed with Dst method (O'Brien and Moldwin, 2003), while in black is the plasmapause location as function of Kp index (Carpenter and Anderson, 1992).

that the maximum of the plasmapause location (or the most distant position) reaches $L \sim 6$, and it is higher than the maximum obtained with Kp equation (3.2), which almost never goes higher than $L = 5$.

It can be noticed that according to Darrouzet et al. (2013), during quiet magnetic periods, the plasmapause coincides more with the outer border of the radiation belts, for electrons with energies higher than 2 MeV. On the other hand, during active periods, the plasmapause is located closer to inner edge of the outer Van Allen belt. The period studied here, from September 2013 to May 2014 can be considered as an active period, because there at least 5 big geomagnetic storms (Dst $< -70\ nT$).

It is clear that for particles at low altitude as the ones measured by EPT, any of the methods really match the data. However there is certain correspondence: for channel 5, mainly when there is an injection of particles which reach lower altitudes. This makes sense because both, the plasmapause location, and the radiation belts are correlated with the Dst index. The correlation is better for channel 6, where between November 2013 and the end of February 2014, the plasmapause computed with both models coincides with the inner edge of the outer belt, in agreement with Darrouzet et al. (2013). Later, between the end of February until the end of May 2014, the plasmapause location, computed with O'Brien and Moldwin (2003) method, matches the outer boundary of the outer belt. Although, it is very important to keep in mind that the fluxes here are very low.

3.4 Conclusions

The event of 17 March 2015 is the highest geomagnetic storm that has been observed since the launch of PROBA-V in May 2013, and during the current solar cycle, with a Dst index as low as -223 nT. We report here the injection of electrons in the inner belt after geomagnetic storms that make the inner belt visible at all

longitudes at 820 km and not only in the SAA as in 2013 and 2014. The penetration of electrons from 0.5-0.6 MeV (up to 2.4 MeV) in the inner belt, filled up completely the slot region for around one week. Later, the radiation belts slowly went to their original configuration, but electrons stayed trapped in the inner region for around a month.

Other major events appeared in January and June 2015, also with injection of electrons in the inner belt, while this was not observed during the 2 first years of observations. The good discrimination of the EPT instrument allows us also to observe the spectra to study the energy dependence of the electron flux variations during dropouts and after geomagnetic storms for instance, as well as simultaneous modifications in the proton observations. These new observations open many perspectives to better understand the source and loss mechanisms associated to the relativistic and non-relativistic particles in the radiation belts.

A comparison between the plasmapause location computed with two different methods, one related to Dst index (O'Brien and Moldwin, 2003), and the other one linked to Kp index (Carpenter and Anderson, 1992), and the outer belt position was made. Results show that even if any of the methods really match the EPT data, there is certain correspondence, mainly for high energy particles (2.4-8 MeV), when the plasmapause location coincides with the inner edge of the outer belt during active geomagetic activity periods.

Chapter 4

Proton and electron spectra in the South Atlantic Anomaly (SAA)

Part of this chapter has been published in **López Rosson and Pierrard (2017)** at *Advances in Space Research*, Volume 60, Issue 4, p. 796-805. DOI 10.1016/j.asr.2017.03.022. The analysis and the manuscript text presented in this chapter are work of the present author.

4.1 Introduction

As explained earlier in Chapter 1, Section 1.5.3 the South Atlantic Anomaly (SAA) is the region where the inner belt is closest to the Earth and the radiation is very intense at low altitude.

This region is mainly populated by high energy protons and some electrons. Both particle populations are very stable and for a long time it has been thought that there is only one source generating these particles.

Studying the spectra of protons and electrons we have found that depending on the location in the SAA the spectra of both species are different, which indicates the presence of two different populations of protons.

4.2 Spectra in different bins

The shape of the SAA is extremely dependent on the particle species and their energy. For EPT observations, in general the SAA location for electrons at energies up to 1 MeV is $[-100° < \text{Long} < 40°]$, $[-50° < \text{Lat} < 5°]$ as illustrated for instance in Figures 2.2 and 2.4.

For protons, it is even more sensitive to the energy at which the observations are taken. If we consider the first EPT proton channel (9.5-13 MeV), the SAA is very similar in shape to the electron SAA (see Figure 2.10), but if we go only one EPT channel up, the shape drastically changes: at energies between 13 and 29 MeV it will be located at $[-90° < \text{Long} < 25°]$, $[-50° < \text{Lat} < 0°]$, as it is shown in Figure 4.2. In McIlwain magnetic coordinates (McIlwain, 1966) the SAA is located between L shells $L = 1.2$ and $L = 2.2$ (see Figure 4.9).

If we take into account this special characteristic of the SAA, it is necessary to be very careful while choosing the areas that will be studied. For this reason we have chosen 5 square bins (at different locations and different sizes for electrons and protons) where we can effectively find particles at all energy ranges covered by EPT. These bins of $15° \times 15°$ for electrons are:

- Bin 1: $[-55° < \text{Long} < -40°]$, $[-30° < \text{Lat} < -15°]$
- Bin 2: $[-40° < \text{Long} < -25°]$, $[-30° < \text{Lat} < -15°]$
- Bin 3: $[-55° < \text{Long} < -40°]$, $[-45° < \text{Lat} < -30°]$
- Bin 4: $[-40° < \text{Long} < -25°]$, $[-45° < \text{Lat} < -30°]$
- Bin 5: $[0° < \text{Long} < 15°]$, $[-35° < \text{Lat} < -20°]$

and can be seen in Figure 4.1.

This bin size is big enough to use only one month of data (the particle flux will be averaged over that time period) and still have sufficient measurements in order to have reliable statistics to draw conclusions.

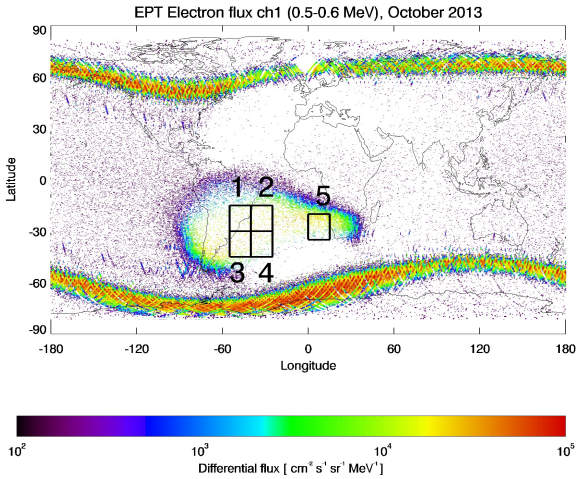

Figure 4.1: Map of the electron fluxes in channel 1 (0.5–0.6 MeV) observed by EPT during October 2013, including the five bins that are studied.

For protons the bins are smaller (see Figure 4.2), $5° \times 5°$ each. This is because the proton flux is higher than the electron flux, thus it is easier to find more protons concentrated in a smaller area. Although, the flux will be averaged over three months data to have enough statistics. For this special study, only 10 of the 11 proton energy channels will be used. The first channel (9.5-13 MeV) is not working properly since the recalibration of EPT, performed between June and September 2014 (for more details see Section 2.1), and it can be used to see variations from one period to another but not to evaluate absolute flux values.

After the recalibration, where CSR tried to go back to previous

noise levels without success for channel 1, the values for this energy range (9.5-13 MeV) are not reliable anymore, hence the data of this channel will not be used after June 2014.

The five proton bins are:

- Bin 1: $[-50° < \text{Long} < -45°]$, $[-25° < \text{Lat} < -20°]$
- Bin 2: $[-35° < \text{Long} < -30°]$, $[-25° < \text{Lat} < -20°]$
- Bin 3: $[-50° < \text{Long} < -45°]$, $[-40° < \text{Lat} < -35°]$
- Bin 4: $[-35° < \text{Long} < -30°]$, $[-35° < \text{Lat} < -30°]$
- Bin 5: $[5° < \text{Long} < 10°]$, $[-25° < \text{Lat} < -20°]$

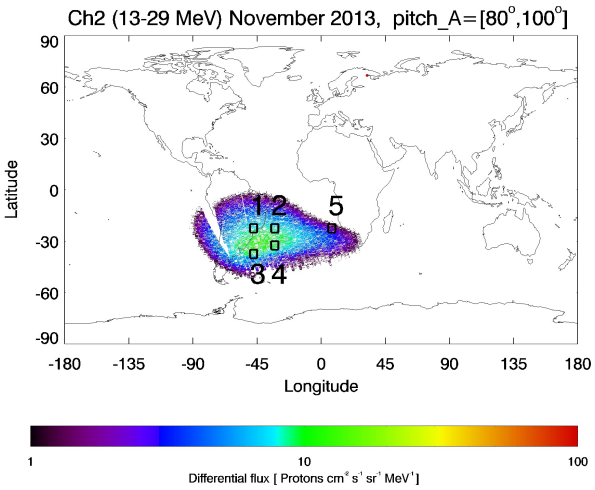

Figure 4.2: Proton fluxes measured by EPT in channel 2 (13–29 MeV) during November 2013. The used measurements have pitch angles between 80° and 100°. The five bins used for the study are also illustrated.

For both particle species two datasets will be used to be sure that the results are valid independently of the time period. November 2013 and April 2015 will be used to compare the electron spectra, while for protons the datasets will be October-December 2013 and April-June 2015.

4.3 Electron spectra

We can see in Figure 4.1 that the fluxes of electrons are lower in the SAA than in the horns at higher latitudes. They decrease as the energy increases. They will become practically zero for ultrarelativistic energies according to Baker et al. (2014). For this reason it is necessary to have a bin size big enough to find particles in all EPT energy ranges, which for electrons is from 0.5 to 20 MeV. It can also be seen in Figure 4.1 the fluxes at high latitudes, or the so called 'horns' which correspond to the penetration of the outer electron belt at low altitudes. The highest electron fluxes are always found at these high latitudes. As it was mentioned earlier we can notice that the extent of the SAA is larger for electrons than for protons.

Figure 4.3 shows the position of the bins for channel 5 (1.0-2.4 MeV) in a zoom of the SAA during October 2013. Also visible is the edge of the SAA for channel one, located at $L = 2.2 - 2.23$. This illustrates that the South Atlantic Anomaly location varies depending on the particles energy. The electron fluxes are very low, especially for higher energies. The shape of the SAA is different from the configuration at lower energy (see Figure 4.1). It is almost empty (very low fluxes) with very low fluxes in the north part of the SAA at this energy range. The average electron spectra observed by EPT during the month of October 2013 are illustrated in Figure 4.4, for the five different bins.

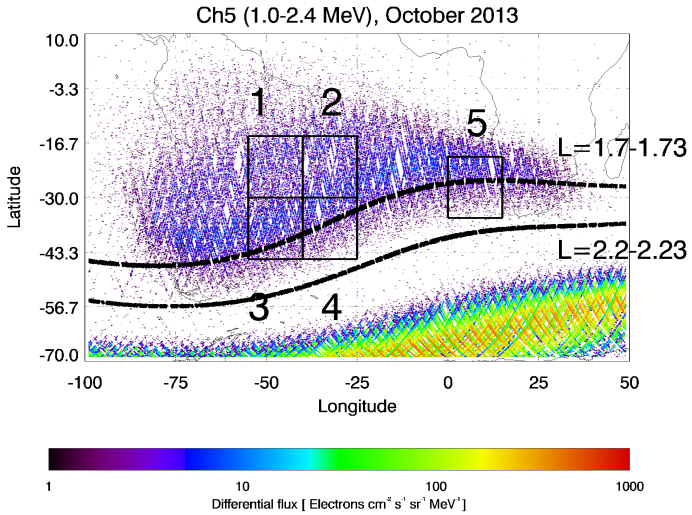

Figure 4.3: Zoom of the SAA showing electron fluxes in channel (1.0-2.4 MeV) observed by EPT during October 2013, including the five bins that will be studied, the L shells corresponding to the bins center, and the border of the SAA for channel 1 at $L = 2.2$.

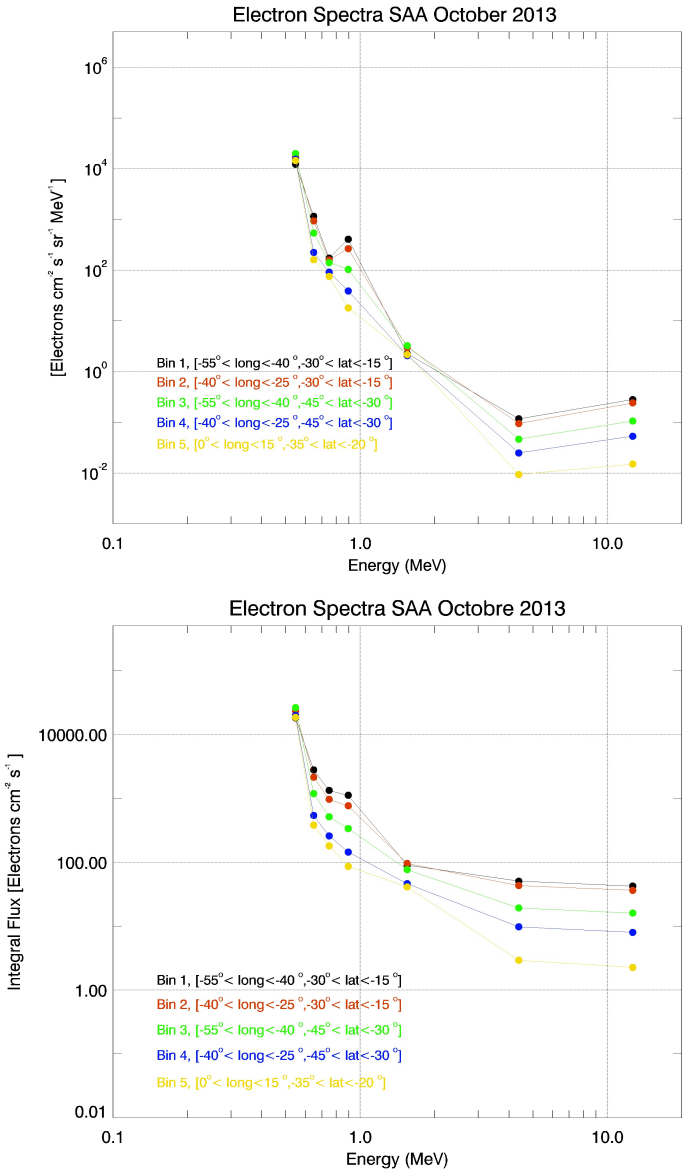

Figure 4.4: Average electron spectra observed by EPT in October 2013 in the SAA for the 5 bins color coded. The upper panel shows the differential flux, while the bottom panel shows the integral flux.

The upper figure shows the differential flux [cm^{-2} s^{-1} sr^{-1} MeV^{-1}] while the bottom panel represents the omnidirectional integral flux [cm^{-2} s^{-1}]. Omnidirectional integral fluxes are calculated by first, multiplying the differential flux for a certain channel by ΔE, or the energy bandwidth of the respective channel. Then, summing up the flux from all energy channels higher than an energy threshold, thus integrating the flux from the highest to the lowest energy channels, and finally multiplying by 4π.

The differential spectra from Figure 4.4 (upper panel) shows clearly a peak in channel 4 (0.8-1 MeV) in bin 1 and 2. Here a difference seems to appear between the north and south part of the SAA and the use of differential fluxes instead of integral fluxes allows us to observe these differences and the corresponding energy dependence. Bins 1 and 2 spectra have exactly the same shapes, just that the flux values are slightly different. The spectra on bins 4 and 5 show lower fluxes but again they have the same slopes. These similarities can be explained by two populations of electrons ruled by different mechanisms: one populating the north region of the SAA and the other one in the south part, as we could already suspect seeing Figure 4.3, where it is possible to observe a difference between the north and the south part of the South Atlantic Anomaly.

To be sure our spectra are representative, we have also checked the spectra for April 2015, where the five bins on the world map for channel 1 (0.5-0.6 MeV) and channel 5 (1.0-2.4 MeV) are shown in Figure 4.5.

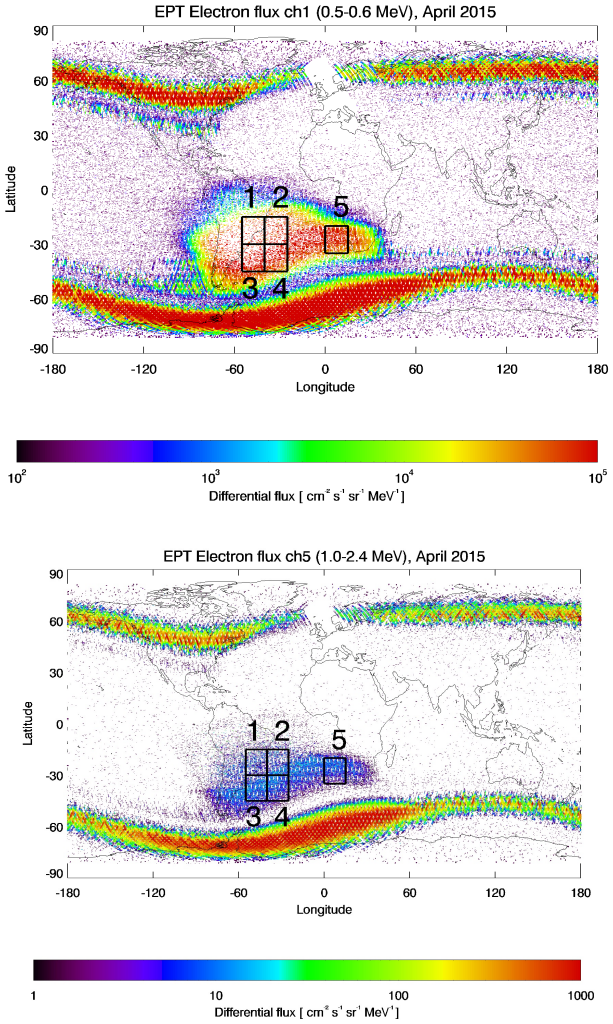

Figure 4.5: Map for electrons flux observed by EPT during April 2015 in channel 1 with energies between 0.5 and 0.6 MeV, and channel 5 with energies between 1.0 and 2.4 MeV. The fluxes in channel 5 still remain very high in the SAA, mostly in the south part.

By comparing Figures 4.1 and 4.5 upper panel, we may observe

that the fluxes are much higher during April 2015, in the outer belt but also in the SAA. This is expected considering the high fluxes measured in 2015 and the intense geomagnetic storms of January and March 2015 (Pierrard and López Rosson, 2016). Note that fluxes remained very high, even for higher energies, like the bottom panel of Figure 4.5 showing the fluxes on channel 5, for energies between 1.0 and 2.4 MeV. But for energies from 2.4 to 8 MeV (ch6) and above (ch7, 8 to 20 MeV), the SAA is almost empty and only high latitude fluxes are observed.

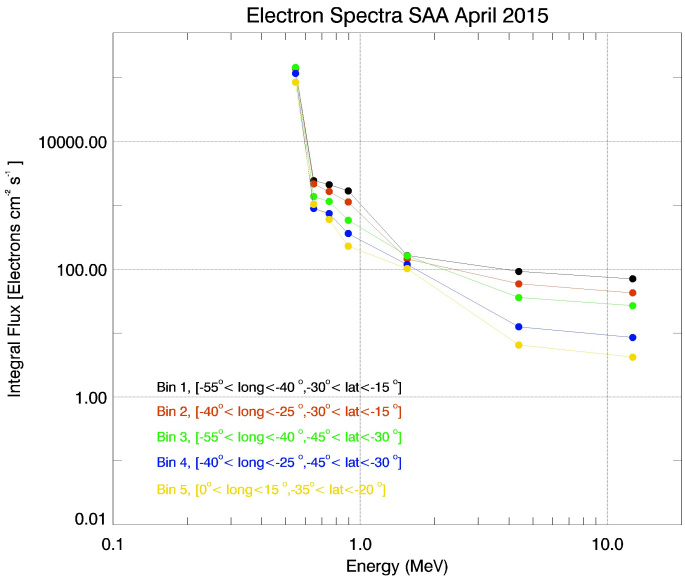

Figure 4.6: Omnidirectional integral flux of electrons spectra for the five bins during April 2015.

If we look at the spectra shown in Figure 4.6, as expected from the information seen on the world maps, the fluxes are higher than in October 2013 (check Figure 4.4). For instance for bin 1, the flux in the first channel is higher for more than one order of magnitude in the SAA (around 10^5 *particles* $cm^{-2}s^{-1}$ in April 2015 while 10^4 *particles* $cm^{-2}s^{-1}$ during October 2013). This is a consequence

of the big geomagnetic storm occurred on 17 March 2015, where electrons penetrated deep down closer to the Earth, completely filling the slot region and also reaching the inner belt (Pierrard and López Rosson, 2016). These particles remained trapped for a few weeks after the event, which is why we can observe higher fluxes in April 2015 than in October 2013.

We have used NASA AE8 empirical model (Vette (1991); for more details see Section 1.10) to compare with our data. This comparison is shown in Figure 4.7.

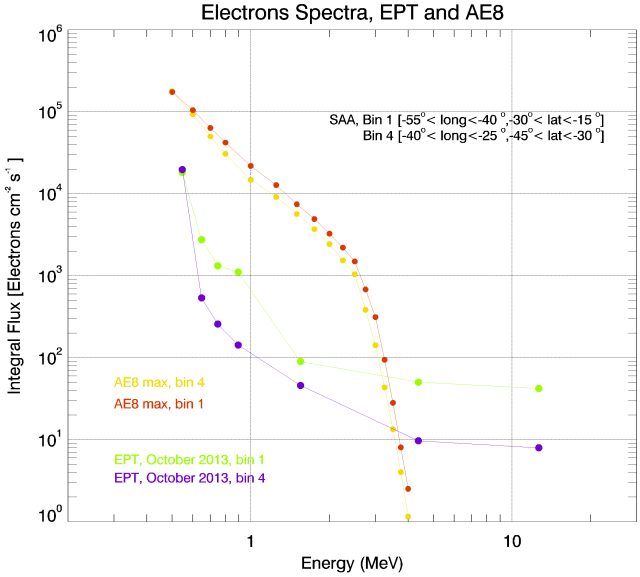

Figure 4.7: Average integral electron spectra observed by EPT in October 2013 in bins 1 and 4 of the SAA and comparison with models AE8-MAX on the same bins.

The empirical model provided by the Space ENVironment Information System (SPENVIS, `https://www.spenvis.oma.be`) differentiates minimum and maximum solar activity, but the differences for electron fluxes at 820 km are very small. We used AE8-MAX spectrum because 2013 is close to solar maximum activity. AE8

makes flux estimations between energies 0.04 and 7 MeV, which is lower than EPT's highest energy channel (8.0-20 MeV).

We have selected two bins to compute the model, at the same locations of EPT bins 1 and 4. In Figure 4.7 the yellow curve represents the spectra in bin 4 calculated with AE8 while the red curve is the spectra for bin 1. The difference between bin 1 and 4 predicted by AE8-MAX is very small and both bins look practically identical. In the energy region from 3 MeV to 4 MeV the fluxes obtained with the NASA model and EPT data show certain similarity for bin 1. For other energies, the fluxes observed by EPT in the SAA are lower than the AE8 model, similar to what has been obtained before, for example by Li et al. (2015). Models such as AE8 (minimum and maximum) are useful but constructed from relatively old and sparse datasets, from scientific satellites. Additionally there are large uncertainties over the maximum electron flux that might be encountered, its energy spectrum and its duration. We need to keep in mind that in those early days of space exploration, when space instrumentation was just starting to be developed, contamination issues were very common and more problematic to solve. The satellite data used on AE8 dates back to the early sixties (Vette, 1991). That is why EPT measurements with improved particle discrimination can help to improve empirical models. These data will be used to improve the TOP model especially dedicated to determine dynamical flux variations of electrons at LEO during geomagnetic storms as well for quite periods (Benck et al., 2013). The advantage of this model is that at a given position, it is possible to simulate the variability of the particles flux. The data sets used, from satellites orbiting at LEO, are: SAC-C/ICARE from December 2000 to September 2006, and DEMETER/IDP between August 2004 and March 2006. On the other hand, a disadvantage of TOP is that is actually only possible to estimate flux variations for LEO positions.

Comparing the two months studies, April 2015 with October 2013, it is visible in Figure 4.8 that fluxes are higher by more than one order of magnitude in April 2015 for energies lower than 0.6 MeV.

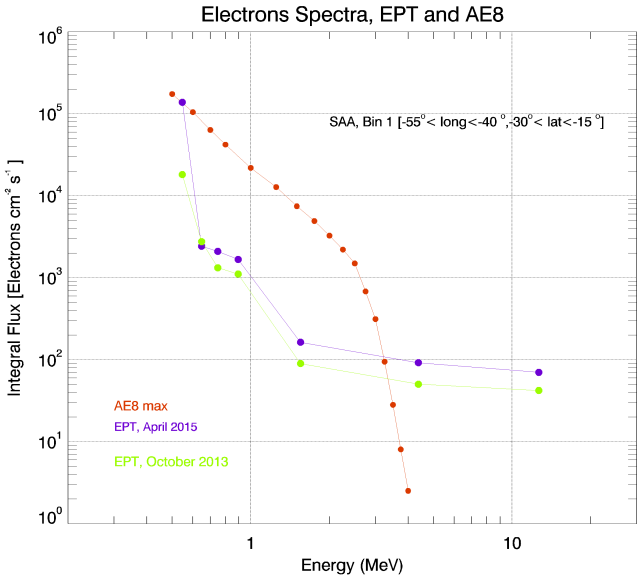

Figure 4.8: Average integral electron spectra observed by EPT in October 2013 and April 2015 in bin 1 of the SAA and comparison with predictions for bin 1 of AE8-MAX.

For intermediate energies (0.6-1 MeV) both months show similar values, and for higher energies April 2015 shows always higher fluxes than October 2013 but the differences are less significant than in channel 1. Notice that the shapes of the curves are exactly the same for both months. We have also included the prediction of AE8 for the bin 1. It is clear that this model overestimates electron fluxes at LEO, except for energies higher than 3 MeV, where the fluxes are underestimated.

4.4 Proton spectra

The same five bins illustrated in Figure 4.2 are now shown in Figure 4.9 as a zoom of the South Atlantic Anomaly that includes also the location of the SAA as bins on terms of L (McIlwain parameter

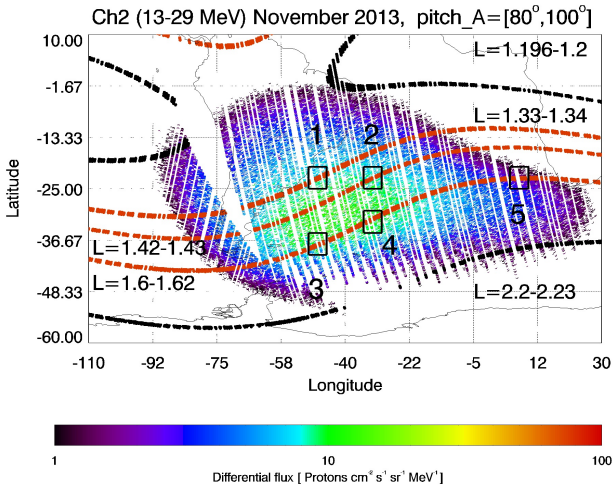

Figure 4.9: Zoom of the SAA during November 2013. The five bins are shown as their L position.

(McIlwain, 1966), see Section 1.4). The values at the center of each bin are:

- Bin 1: $L = 1.33 - 1.34$, B=0.165 nT
- Bin 2: $L = 1.42 - 1.43$, B=0.174 nT
- Bin 3, 4, 5: $L = 1.6 - 1.62$, B=0.178 nT, B=0.176 nT, B=0.195 nT respectively

As we mentioned in Section 4.2 the SAA changes depending on the energy. We can observe this change in Figure 4.10. For energies between 13 and 29 MeV (channel 2, upper panel) the border of the SAA coincides with L shell $L = 2.2-2.23$, while for higher energy at 155-182 MeV (channel 7, bottom panel) the border is now situated at $L = 1.7 - 1.73$ which means that for higher energies there are no particles at the same locations than lower energies, as in this case between $L = 1.7$ and $L = 2.23$.

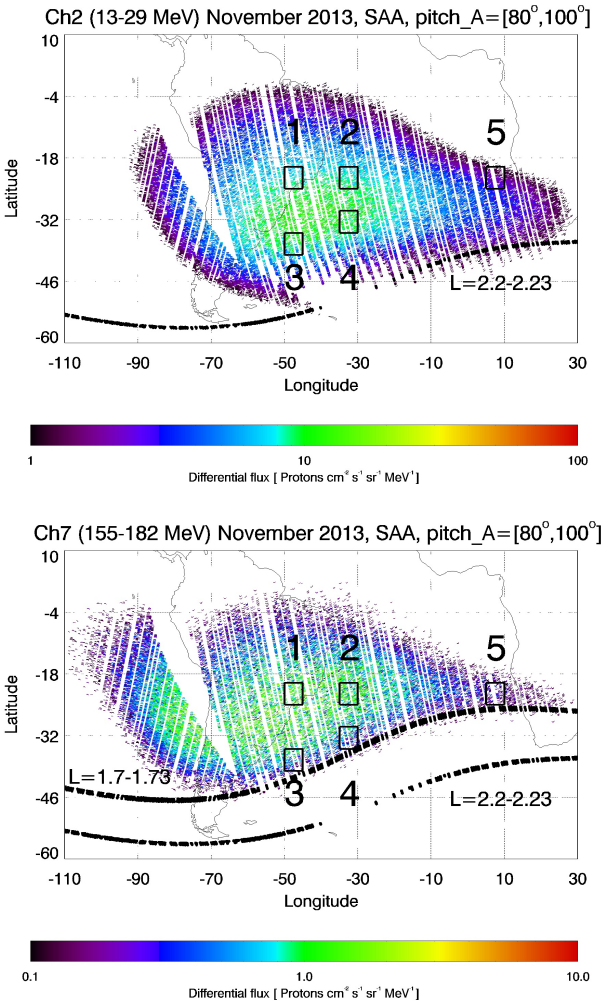

Figure 4.10: Zoom of the SAA during November 2013. The upper panel shows channel 2 (13-29 MeV) and the L-shell that crosses the south limit of the SAA. Lower panel shows channel 7 (155-182 MeV) and the L-shells for channel 7 and channel 2. We can see that for high energy there are no particles between $L = 1.7$ and $L = 2.23$.

At low altitudes like the EPT orbit at 820 km, proton fluxes are only observed in the South Atlantic Anomaly. In case of Solar

Energetic Particle (SEP) events, proton fluxes can also be observed at high latitudes during a few days (Pierrard et al., 2014).

For this study we selected only observations with pitch angle values between 80° and 100° in order to deal with proton anisotropy at low altitude due to pitch angle distribution (Badhwar and Konradi, 1990). With this selection, the extension of the SAA is reduced. As it crosses the SAA, the EPT boresight is either towards East during night crossings or towards West during day crossings. Due to the particularity of the PROBA-V orbit, the pitch angle selection creates a triangular empty area over the Pacific Ocean covering as well a part of Chile and Argentina. Nevertheless, this selection does not modify the spectra. We compared the spectra using all the pitch angles and the spectra with the filter: The slopes and flux values were the same. In the SAA, the proton fluxes are very stable and they do not significantly change from one month to another, as we will show later.

Figure 4.11 illustrates the averaged differential proton spectra in $[cm^{-2}\ s^{-1}\ sr^{-1}\ MeV^{-1}]$ obtained from EPT measurements in each of the 5 selected bins in the SAA during the period between October to December 2013. It may be seen that the spectra have several orders of magnitude difference depending on the location of the bin. They all decrease with energy, but the spectra of bins 3 and 4 (south of the SAA) decrease faster than those in bins 1 and 2 (north region of the SAA). The highest fluxes for lower energies are observed in bins 3 and 4, but for higher energies, bins 1 and 2 have the highest fluxes.

Lowest fluxes are obtained in bin 5, in the east of SAA, as we could already expect from the map in Figure 4.10. Also notice that the spectra seem to be organized in pairs like for the electrons. This possibly related with the bins locations because bin 3 and 4 cross the same L-shell while bin 1 and 2 are close to the same L line ($L = 1.4 - 1.6$). This could explain the similarity between each pair of bins. The different slopes of the differential spectra in the north and the south of the South Atlantic Anomaly can indicate the presence of two different belts with different physical

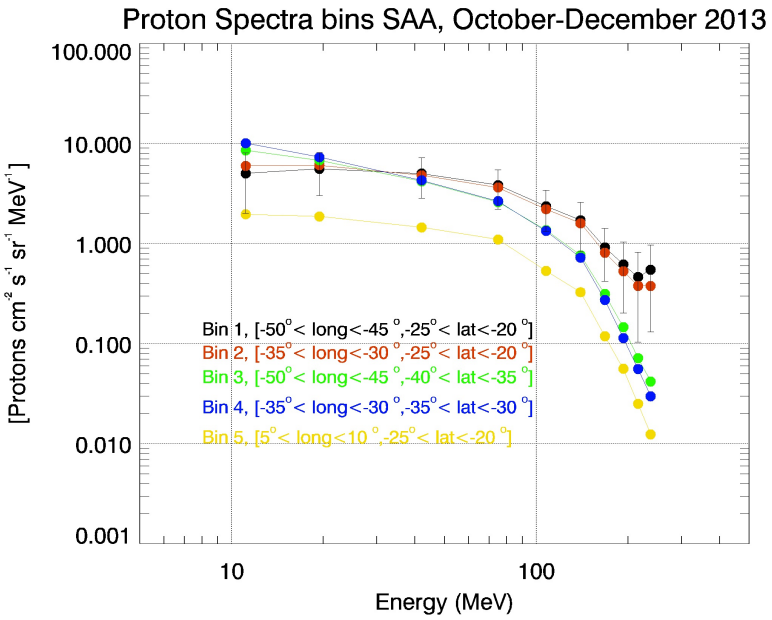

Figure 4.11: Average differential proton spectra observed by EPT from October to December 2013 from 13 to 248 MeV in the five different bins of the SAA. Error bars are shown for bin 1. The other four bins have similar error bars, but are not shown to avoid confusion. The average was calculated as the mean of the flux for a determined energy channel during three months, and the errors as the standard deviation of the mean for the same period.

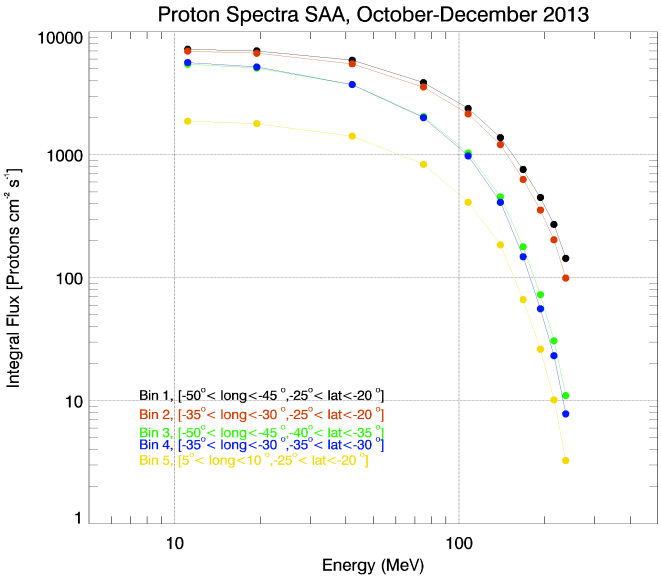

Figure 4.12: Integral proton spectra during October until December 2013.

processes acting upon them. The inner belt is mainly assumed to be due to CRAND (Cosmic Ray Albedo Neutron Decay, see Section 1.6.1), and sometimes particles of the neutral sheet can be transported by radial diffusion ((Murayama and Simpson, 1968)). Nevertheless, some regions of the inner belt can also be modified during exceptional SEP events as those observed in October 2003 (Looper et al., 2005).

To study these possible different mechanisms, we have also calculated the omnidirectional integral flux in $[cm^{-2}\ s^{-1}]$ for the five bins, by adding the fluxes observed in the different channels, which is presented in Figure 4.12.

This time, bins 1 to 4 have practically the same flux for the lowest energy but then they split and we see again the 'pairs behavior': same slope and fluxes for bin 1 and 2 while bin 3 and 4 are almost identical. The lowest fluxes again are obtained in bin 5.

The different slopes for the integral fluxes in the north and south parts of the SAA confirm probable different origins.

We have checked the spectra during other periods of time to verify that our results are representative.

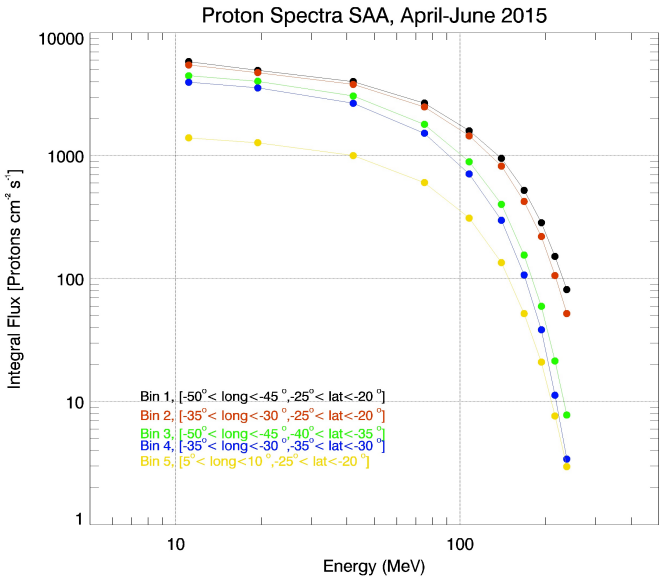

Figure 4.13: Averaged proton spectra using integral flux measured by EPT from April to June 2015, for the same five bins used from October to December 2013 in Figure 4.12.

Figure 4.13 shows the averaged proton spectra using integral fluxes measured by the EPT instrument from April to June 2015. The spectral slopes are almost the same as in October-December 2013, except that the fluxes in bin 1 and 2 have a higher value in 2013. Bin 5 looks identical during both periods. The small difference between the two datasets may not be satisfactorily explained by the high activity of the year 2015, since the main observed SEP events are observed at the end of June 2015, especially three in this month and one in October 2015 (Pierrard and López Rosson, 2016).

During this study, as we checked the pitch angle selection, we

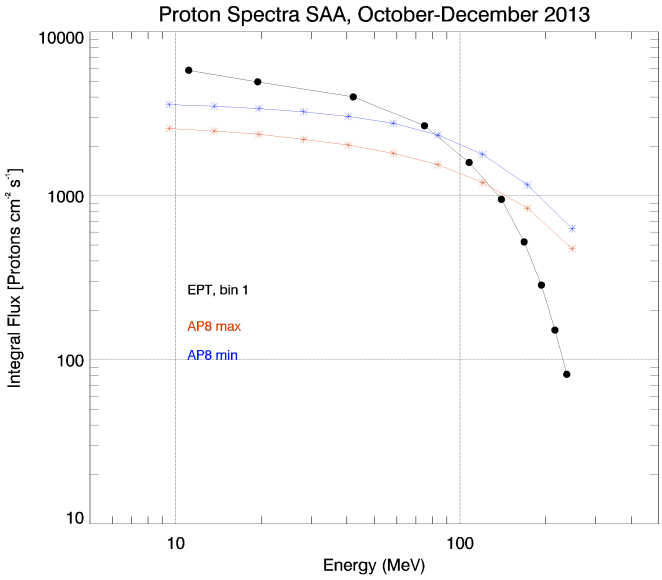

Figure 4.14: EPT spectra on bin 1 (black) between October and December 2013, compared with AP8-min (blue) and AP8-max (red).

also tested different bin sizes, up to bins of $15° \times 15°$ each on the same locations in the SAA and we obtained similar results on the spectra shapes and flux values.

As we did with electrons comparing with NASA model, we have compared with the omnidirectional spectra obtained with the empirical model AP8 (Sawyer and Vette, 1976) of NASA for solar minimum and maximum solar activity at a similar position than bin 1 which corresponds to L= 1.22–1.25, B = 0.17G, using SPENVIS (`www.spenvis.oma.be`).

Figure 4.14 shows omnidirectional integral spectra of integral fluxes in $[cm^{-2}\ s^{-1}]$ observed in October-December 2013 in bin 1 of the SAA.

EPT fluxes are higher than those of the models AP8 MIN and MAX for energies lower than 100 MeV, while they are one order

lower than AP8 for the highest energies. AP8-MAX shows lower fluxes than AP8-MIN at low altitudes because the atmosphere is warmer during maximum solar activity and its expansion at higher altitude erodes more the radiation belts particles trapped in the Earth's magnetic field during this period.

The EPT unidirectional differential flux has been converted in omnidirectional integral flux by multiplying it by a factor of 4π, but without dividing it by the Badhwar-Konradi scaling factor (Badhwar and Konradi, 1990) or 'anisotropy conversion factor' (Kruglanski and Lemaire, 1996) used when it is necessary to take into account the anisotropy in the proton flux, that will depend on the pitch angle distributions of the observations (Borisov et al., 2014).

It is already known that AP8 fluxes predictions can be very different from satellite measurements depending on the location. For example Borisov et al. (2014) showed that for energies lower than 60 MeV, at [$-20.5°$Lat, $-56.8°$Long] AP8 flux values never agree with EPT data at the same location. On the same hand, at [$-18°$Lat, $-57.3°$Long], this empirical model always overestimates the proton fluxes for energies lower than 30 MeV and higher than 100 MeV. Finally, they also tested AP9 at this same location, finding that AP9 flux prediction is 5 times larger than EPT measurements.

4.5 Temporal variations

Another way to see why the spectra are different and a possible way to prove the existence of two populations is to check the temporal evolution of the flux on the different bins.

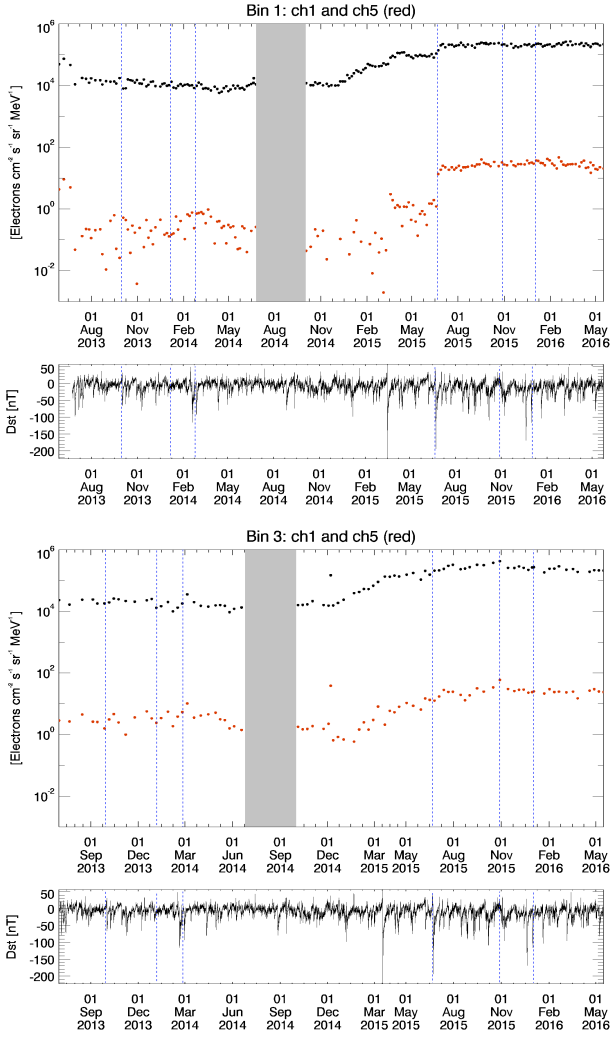

Figure 4.15: Electrons temporal evolution during 31 months, for bins 1 and 3. The curve in black represents channel 1 (0.5-0.6 MeV) while the red one shows channel 5 (1-2.4 MeV). The vertical dotted lines show the SEP events for this period.

We have studied the time period of June 2013 until April 2016 of EPT which corresponds to 31 months.

Because the electron fluxes are higher it is better to use smaller bins to study the temporal evolution. If we used the 15° square there are too many particles and it becomes necessary to do an average, but doing this we will lose information about the small flux changes, which is the feature we want to investigate. This way we have reduced the bin size to coincide with the proton bins size of 5° square.

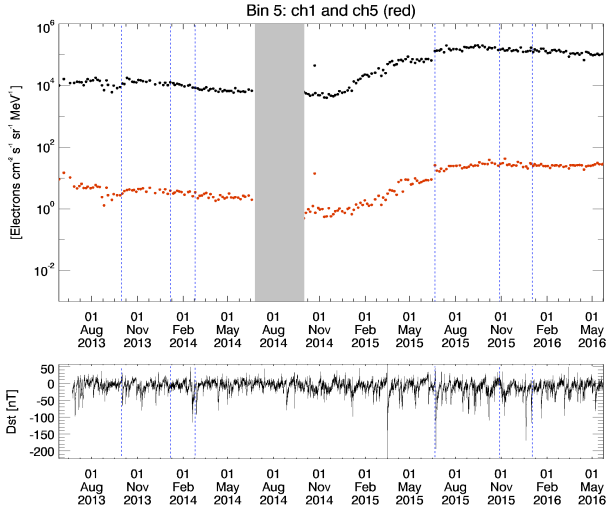

Figure 4.16: Same as Figure 4.15 but for bin 5.

The temporal evolution for bin 1, 3 and 5 of electrons is shown in Figures 4.15 and Figure 4.16 respectively. Channel 1 (0.5-0.6 MeV) is shown in black, and channel 5 (1-2.4 MeV) in red. The gray rectangle masks the period when the instrument was under recalibration (see Section 2.1). On these figures it is possible to see that the three bins are different, with bin 3 having completely different shape fluxes. If the particles on the distinct bins obey the same mechanismswe would expect that the temporal evolution would be the same for the five bins, which is not the case.

Figure 4.17 shows the temporal evolution of the proton flux in bins 1, 4 and 5. The gray rectangle covers the dates where the

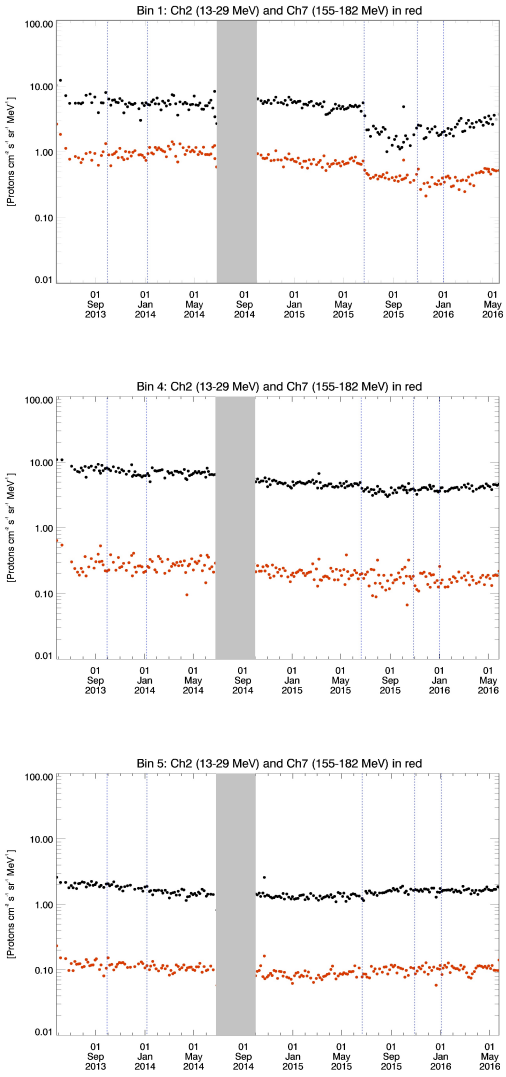

Figure 4.17: Temporal evolution of the proton flux during the period of EPT from June 2013 to April 2016, for channel 2 (13–29 MeV) in black and ch7 (155–182 MeV) in red. Bin 1 is shown on the upper panel, bin 4 in the middle, while bin 5 can be seen on the lower panel. The gray rectangle masks the period when the instrument was off due to recalibration.

instrument was not working and the data being recalibrated, from June 2014 to September 2014.

The blue dotted lines on the plots represent the SEP events (`https://umbra.nascom.nasa.gov/SEP/`), from left to right:

1. 30/09/2013
2. 06/01/2014
3. 21/06/2015
4. 29/10/2015
5. 02/01/2016

All panels of Figure 4.17 illustrate fluxes of channel 2 in black and channel 7 in red. The fluxes in bin 1 (upper panel) are very variable with time, and show especially a strong decrease after the SEP event of June 2015. The case is similar for bin 2, reason why it is not shown here. On the contrary fluxes in bin 4 (middle plot) and bin 5 (see the bottom panel of Figure 4.17) show almost no time variations. Results in bin 3 are intermediate, with time variations lower than in bins 1 and 2. From this it is clear that there is one population of protons in the north part of the SAA that changes fast, related with SEP events, but in the south of the SAA there is another population which remains stable during long time periods.

4.6 Conclusions

In the SAA, electron fluxes are much lower and more stable than at high latitudes. Although some variations can be observed especially associated to geomagnetic storms. A good example of this trend is 2015 where higher fluxes were detected due to particles injection during geomagnetic storms (see Pierrard and López Rosson (2016)).

Using Van Allen Probes observations Baker et al. (2014) found that ultrarelativistic electrons do not penetrate lower than $L < 2.8$

so there are no electrons of $\geqslant 2MeV$ in the inner belt. But EPT does observe relativistic electrons on this region though with very low fluxes (between $\sim 1-5$ electrons per $cm^2\ s^1\ sr^1\ MeV^1$ approximately).

EPT proton spectra suggest the existence of two different populations of protons in the SAA. One is very stable, with fluxes that remain constant in time, that can be related with CRAND. The other population on the contrary seems more variable, in the north part of the SAA where some flux changes are observed during SEP events, but further study is necessary to understand if there are other physical mechanisms behind this unexpected behavior.

Note that CSR recently discovered that the proton measurements may be influenced by the saturation of the detector during the big events of 2015 (S. Benck, Private communication 5/10/2018, Benck (to be released end 2018)). This can modify the temporal evolution of the protons.

Comparing the spectra obtained with EPT in the SAA with the NASA empirical model AE8, we found that: 1. There is almost no difference between bin 1 and bin 4 predicted by AE8, and 2. Fluxes predicted by AE8 are always higher than what is observed by EPT, sometimes even more than one order of magnitude bigger, except for energies higher than 3 MeV, where the fluxes are underestimated.

The results for protons show that for energies lower than 100 MeV AP8 prediction is in agreement with EPT observations. But above 100 MeV AP8 overestimates the actual unidirectional fluxes when the models of the fluxes are simply divided by 4π, due to flux anisotropy, especially at high energies.

Other models (AP9 (Ginet et al., 2013), CRRESPRO (Meffert and Gussenhoven, 1994)) also give spectra that can differ by several orders of magnitude in a same location, even for stable regions like the inner belt.

For example, recently Bourdarie et al. (2014) have shown that for LEO orbit AP8 underestimates proton flux by 24% for energies > 40 MeV, while AP9 overestimates it by 97%.

This is one of the reasons why EPT measurements, with an ac-

curate particle discrimination can help to improve predictions done by empirical models, like the Transient Observation-based Particle or TOP model (Benck et al., 2013). EPT observations will be incorporated to this model, which determines electron flux variations at LEO orbit during magnetically disturbed periods.

Chapter 5

Conclusion and Perspectives

The successful launch of Sputnik I in 1957 marked the beginning of the Space Era. Only one year later professor James Van Allen discovered the radiation belts (afterward called Van Allen belts, located at $\sim 2 - 10R_E$), formed by energetic particles –mainly electrons and protons– trapped in the Earth's magnetic field in a toroidal configuration.

Radiation belts are extremely important nowadays because we rely more and more on satellite systems, and they orbit in the proximity of this region. Space radiations are a major hazard for those systems but more importantly for astronauts. In addition, knowing more about the terrestrial radiation belts can also facilitate the research concerning the radiation belts of other planets of the Solar system, like those of Jupiter or Saturn.

The Energetic Particle Telescope (EPT) onboard the PROBA-V satellite, a particle spectrometer designed especially to study radiation belts, can discriminate on site different particle species as electrons, protons or alpha particles. EPT's good quality data during the last five years have contributed to radiation belts research, giving new insight about radiation belts dynamics, as we show in the results presented in this thesis.

For electrons ranging in energy between 0.5 and 20 MeV, the flux changes are related with geomagnetic activity. As it was shown in

Chapter 2, at the 820 km Low Earth Orbit (LEO) of PROBA-V, it is possible for EPT to measure electrons in the South Atlantic Anomaly (SAA) where the fluxes are lower than in the outer belt, which is visible as polar horns in a world map. In those maps we can also observe lower fluxes in the north Atlantic ocean, as a counterpart of the SAA. The electron fluxes decrease as the energy increases, i.e., there are less relativistic electrons, in the inner belt as well as the outer belt. As a consequence of this, the shape of the SAA changes with the energy, shrinking when the energy increases, until it completely disappears at energies > 8 MeV.

In the inner belt, we have detected those relativistic electrons up to EPT's channel 6, with energies between 2.4 to 8 MeV, although the fluxes are very low at this energy range. It is important to mention that it is not possible to know the energy distribution of those particles from EPT data, hence we cannot give a more precise estimation of the upper energy limit of electrons in the inner belt. Measuring relativistic electrons between $2.4 - 8$ MeV in the inner belt is a very interesting finding, which also confirms the excellent performance of EPT: Recently Li et al. (2015) suggested that is was possible to distinguish electrons more energetic than 1.6 MeV in the inner zone.

Particle fluxes predicted by NASA models AE8/AP8 are in agreement with EPT data for lower energies, and during quiet times. The models do not show the flux enhancements related with geomagnetic activity. Also the shape and extent of the SAA is not the same.

The comparisons made with other satellites at different orbits as GOES, POES and Van Allen Probes helped to validate PROBA-V/EPT observations.

During geomagnetic storms or Dst events, electron fluxes first dropout and then increase, even changing the configuration of the radiation belts. Our EPT results concerning the electrons are shown in details in Chapter 3. 2015 was a very active year –in terms of geomagnetic activity– which had the biggest geomagnetic storms of the current solar cycle. Such events injected electrons

that penetrated to lower L shells, even filling the slot region and reaching the inner belt. This new population stayed trapped in the slot for around a week. Then, the radiation belts started slowly to go back to their original configuration.

A comparison between the plasmapause location computed with two different methods, one related to Dst index (O'Brien and Moldwin, 2003), and the other one linked to Kp index (Carpenter and Anderson, 1992), and the outer belt position was made. Results show there is certain correspondence, mainly for high energy particles (2.4-8 MeV), when the plasmapause location coincides with the inner edge of the outer belt during active geomagetic activity periods, as suggested by Darrouzet et al. (2013).

Protons between 9.5 to 300 MeV were also studied in Chapter 2. These particles are only present in the inner belt. However, during Solar Energetic Particles (SEP) events protons are injected into the inner magnetosphere and they can be found at high L shells during a few days. Similar to electrons, the fluxes are higher for lower energy particles, and the shape of the SAA changes also in function of the energy: It becomes smaller as the energy increases. Geomagnetic storms seem to not especially affect this particle species.

Studying in Chapter 4 the particles spectra in the SAA allowed us to conclude that there exit two proton populations: one in the North and one in the South part of the SAA. One is very stable, maybe mainly modulated by CRAND mechanism, because it does not show flux variations in time. In contrast, the second population does show a flux temporal variation. Further investigation is needed to characterize those two populations and give details about their physical mechanisms.

Helium ions are also present in the radiation belts but with very low fluxes. Those particles are mainly found in the inner belt when a couple of months of data are accumulated. As for protons, some ions are injected during SEP events. Helium ions with energies between 38 and 51 MeV are visible at high latitudes during such events.

At the present time, PROBA-V continues orbiting around the

Earth, while EPT is still measuring the particles that populate the Van Allen radiation belts. Because the solar cycle has an effect on the solar wind and the magnetosphere, it is very interesting to investigate the dynamics of the radiation belts on a longer timescale, to be able to measure this impact.

Fitting the particle spectra can be very useful to know more about these particles: Knowing their distribution function, it is possible to estimate their temperature and density. Depending on those profiles, it would be possible to study the evolution of electrons depending on the magnetic activity conditions. Analysis of electron spectra –at different L values in the outer belt and for different geomagnetic conditions (quiet, pre-storm, storm)– and fit to particle distribution functions seems a promising path to explore and is actually the topic of ongoing work.

EPT/PROBA-V observations at LEO orbit can complement other satellite measurements at different orbits, like Van Allen Probes, in order to have a global view of the Van Allen belts from different locations.

Appendix A

Relativistic particles motion

Following section 1.3, we present here the relativistic form of the main equations concerning the trapped particles motion. Some new terms will be introduced as m_0, which is the rest mass of the particle, $\beta = \frac{v}{c}$, where c is the speed of light. The relativistic correction factor γ is $\gamma = (1-\beta^2)^{1/2}$. The mass m of the particle can be also written as $m = \frac{m_0}{(1-\beta)^{1/2}}$ (Northrop, 1963).

Relativistic theory applies to electrons, where for instance an electron of 500 keV moves at 85% c. Because ions are substantially heavier, their velocities will not always be relativistic, e.g., a 500 keV proton has a speed of only 3% of c (Spjeldvik and Rothwell, 1985), thus the non-relativistic equations presented in section 1.3 must be used.

The relativistic equation of motion of a charged particle, where $\vec{p}$ is the momentum, and equivalent to equation 1.2 is:

$$\frac{d\vec{p}}{dt} = \frac{d}{dt}\frac{m_0\vec{v}}{(1-\beta^2)^{1/2}} = q(\vec{E} + \frac{\vec{v}}{c} \times \vec{B}). \tag{A.1}$$

Now, using the relativistic definition of the mass, it is possible to write the gyroradius or Larmor radius (as equation 1.5),

$$r_L = \frac{\gamma m_0 v_\perp}{|q|B}, \tag{A.2}$$

and the relativistic gyrofrequency (equation 1.6):

$$\omega_L = \frac{|q|B}{\gamma m_0}. \tag{A.3}$$

The magnetic moment of a particle, called μ_B (equation 1.16) or M equates

$$\mu = M = \frac{m_0 v_\perp^2}{2B(1-\beta^2)^{1/2}} = \frac{p_\perp^2}{2m_0 B}, \tag{A.4}$$

where $p_\perp$ is the perpendicular component of the relativistic momentum $\vec{p}$ (Northrop and Teller, 1960).

The drift velocity due to external forces, as shown in equation (1.13), but for a relativistic particle is:

$$\vec{v}_D = \frac{c}{q}\frac{\vec{F}_{ext} \times \vec{B}}{B^2}. \tag{A.5}$$

According to Northrop (1963), the nonrelativistic guiding-center equations can be rewritten as relativistic just using the new definition of the mass m in function of (m_0, β). Thus the main drifts of a relativistic particle can be written as:

Drift due to the electric force or $\vec{E} \times \vec{B}$ drift (presented in equation (1.15))

$$\vec{v}_E = c\frac{\vec{E} \times \vec{B}}{B^2}. \tag{A.6}$$

The drift caused by the gravitational force (equation 1.14) is

$$\vec{v}_g = \frac{cm_0\gamma}{qB^2}(\vec{g} \times \vec{B}). \tag{A.7}$$

The gradient drift due to an inhomogeneous magnetic field, $\vec{v}_\nabla$ (equation (1.17)):

$$\vec{v}_\nabla = \frac{Mc}{q\gamma}\frac{\vec{B} \times \vec{\nabla}B}{B^2}, \tag{A.8}$$

and finally the curvature drift (Spjeldvik and Rothwell, 1985), as equation (1.21)

$$\vec{v}_{R_c} = \frac{c}{\gamma q} \frac{p_{\parallel}^2}{m_0 B^3} (\vec{B} \times \vec{\nabla}_{\perp} |\vec{B}|) \tag{A.9}$$

Again, the total drift velocity will be the superposition of all contributing drifts.

Bibliography

G. D. Badhwar and A. Konradi. Conversion of omnidirectional proton fluxes into a pitch angle distribution. *Journal of Spacecraft and Rockets*, 27:350–352, June 1990. doi: 10.2514/3.26148.

D. N. Baker, S. G. Kanekal, V. C. Hoxie, M. G. Henderson, X. Li, H. E. Spence, S. R. Elkington, R. H. W. Friedel, J. Goldstein, M. K. Hudson, G. D. Reeves, R. M. Thorne, C. A. Kletzing, and S. G. Claudepierre. A Long-Lived Relativistic Electron Storage Ring Embedded in Earth's Outer Van Allen Belt. *Science*, 340(6129):186–190, 2013. ISSN 0036-8075. doi: 10.1126/science.1233518. URL `http://science.sciencemag.org/content/340/6129/186`.

D. N. Baker, A. N. Jaynes, V. C. Hoxie, R. M. Thorne, J. C. Foster, X. Li, J. F. Fennell, J. R. Wygant, S. G. Kanekal, P. J. Erickson, W. Kurth, W. Li, Q. Ma, Q. Schiller, L. Blum, D. M. Malaspina, A. Gerrard, and L. J. Lanzerotti. An impenetrable barrier to ultrarelativistic electrons in the Van Allen radiation belts. , 515: 531–534, November 2014. doi: 10.1038/nature13956.

J. Bartels, N. H. Heck, and H. F. Johnston. The three-hour-range index measuring geomagnetic activity. *Terrestrial Magnetism and Atmospheric Electricity*, 44(4):411–454, 1939. doi: 10.1029/TE044i004p00411. URL `https://onlinelibrary.wiley.com/doi/abs/10.1029/TE044i004p00411`.

S. Benck. Technical note 1B, Data analysis procedure for PROBA-

V/EPT spectra aquired after 15/09/2014. Technical report, CSR, Université catholic de Louvain, to be released end 2018.

S. Benck, L. Mazzino, M. Cyamukungu, J. Cabrera, and V. Pierrard. Low altitude energetic electron lifetimes after enhanced magnetic activity as deduced from SAC-C and DEMETER data. *Annales Geophysicae*, 28(3):849–859, 2010. doi: 10.5194/angeo-28-849-2010. URL https://www.ann-geophys.net/28/849/2010/.

S. Benck, M. Cyamukungu, J. Cabrera, L. Mazzino, and V. Pierrard. The transient observation-based particle (TOP) model and its potential application in radiation effects evaluation. *J. Space Weather Space Clim.*, 3:A03, 2013. doi: 10.1051/swsc/2013024. URL https://doi.org/10.1051/swsc/2013024.

T. Beutier, D. Boscher, and M. France. SALAMMBO: A three-dimensional simulation of the proton radiation belt. *Journal of Geophysical Research: Space Physics*, 100(A9):17181–17188, 1995. doi: 10.1029/94JA02728. URL https://agupubs.onlinelibrary.wiley.com/doi/abs/10.1029/94JA02728.

J. B. Blake, W. A. Kolasinski, R. W. Fillius, and E. G. Mullen. Injection of electrons and protons with energies of tens of MeV into $L < 3$ on 24 March 1991. *Geophysical Research Letters*, 19(8):821–824, 1992. doi: 10.1029/92GL00624. URL https://agupubs.onlinelibrary.wiley.com/doi/abs/10.1029/92GL00624.

J. B. Blake, P. A. Carranza, S. Claudepierre, J. Clemmons, W. R. Crain Jr, Y. Dotan, J. F. Fennell, F. H. Fuentes, R. M. Galvan, J. S. George, M. Henderson, M. Lalic, A. Y. Lin, M. D. Looper, D. J. Mabry, J. E. Mazur, B. Mccarthy, C. Nguyen, T. P. O'Brien, and M. P. Zakrzewski. The Magnetic Electron Ion Spectrometer (MagEIS) instruments aboard the Radiation Belt Storm Probe (RBSP) spacecraft. 179, 06 2013.

S. Borisov. The PROBA-V/EPT L1 Data User Manual. *Internal communication*, 2015.

S. Borisov. Technical note 6 & 7. The EPT-CD data status report 2 & 3. Technical report, CSR, Université catholic de Louvain, 2015.

S. Borisov, S. Benck, M. Cyamukungu, P. E. O'brien, J. E. Mazur, P. Nieminen, H. Evans, and E. J. Daly. Angular Distribution of Protons Measured by the Energetic Particle Telescope on PROBA-V. *IEEE Transactions on Nuclear Science*, 61:3371–3379, 2014.

S. Bourdarie and D. Boscher. Earth radiation belts. In J-P. Rozelot, editor, *Solar and Heliospheric Origins of Space Weather Phenomena*, pages 93–118. Springer Berlin Heidelberg, Berlin, Heidelberg, 2006. ISBN 978-3-540-33759-1. doi: 10.1007/3-540-33759-8_5. URL `https://doi.org/10.1007/3-540-33759-8_5`.

S. Bourdarie, D. Falguere, C. Inguimbert, C. Deneau, J. R. Vaillé, E. Lorfèvre, and R. Ecoffet. Correlation of In-Flight Displacement Damage on the OSL Sensor With Space Environment On-Board Jason-2 Spacecraft. *IEEE Transactions on Nuclear Science*, 61(4):1643–1647, Aug 2014. ISSN 0018-9499. doi: 10.1109/TNS.2014.2315832.

J. Cabrera, M. Cyamukungu, P. Stauning, A. Leonov, P. Leleux, J. Lemaire, and G. Grégoire. Fluxes of energetic protons and electrons measured on board the Oersted satellite. *Annales Geophysicae*, 23(9):2975–2982, 2005. doi: 10.5194/angeo-23-2975-2005. URL `https://www.ann-geophys.net/23/2975/2005/`.

D. L. Carpenter and R. R. Anderson. An ISEE/Whistler model of equatorial electron density in the magnetosphere. *Journal of Geophysical Research: Space Physics*, 97(A2):1097–1108, 1992. doi:

10.1029/91JA01548. URL https://agupubs.onlinelibrary.wiley.com/doi/abs/10.1029/91JA01548.

S. G. Claudepierre, T. P. O'Brien, J. B. Blake, J. F. Fennell, J. L. Roeder, J. H. Clemmons, M. D. Looper, J. E. Mazur, T. M. Mulligan, H. E. Spence, G. D. Reeves, R. H. W. Friedel, M. G. Henderson, and B. A. Larsen. A background correction algorithm for Van Allen Probes MagEIS electron flux measurements. *Journal of Geophysical Research (Space Physics)*, 120:5703–5727, July 2015. doi: 10.1002/2015JA021171.

R. Cowen. Ephemeral third ring of radiation makes appearance around Earth. 2013. URL https://doi.org/10.1038/nature.2013.12529.

M. Cyamukungu and G. Grégoire. The Energetic Particle Telescope (EPT) concept and performances, 2011. URL https://doi.org/10.1117/12.892420.

M. Cyamukungu, S. Benck, S. Borisov, G. Grégoire, J. Cabrera, J. L. Bonnet, B. Desoete, F. Preud'homme, C. Semaille, G. Creve, J. D. Saedeleer, S. Ilsen, L. De Busser, V. Pierrard, S. Bonnewijn, J. Maes, E. V. Ransbeeck, E. Neefs, J. Lemaire, E. Valtonen, R. Punkkinen, M. Anciaux, K. Litefti, N. Brun, D. Pauwels, C. Quevrin, D. Moreau, A. Helderweirt, W. Hajdas, and P. Nieminen. The Energetic Particle Telescope (EPT) on Board PROBA-V: Description of a New Science-Class Instrument for Particle Detection in Space. *IEEE Transactions on Nuclear Science*, 61(6):3667–3681, Dec 2014. ISSN 0018-9499. doi: 10.1109/TNS.2014.2361955.

F. Darrouzet and J. De Keyser. The dynamics of the plasmasphere: Recent results. *Journal of Atmospheric and Solar-Terrestrial Physics*, 99:53–60, July 2013. doi: 10.1016/j.jastp.2012.07.004.

F. Darrouzet, V. Pierrard, S. Benck, G. Lointier, J. Cabrera, K. Borremans, N. Yu Ganushkina, and J. De Keyser. Links

between the plasmapause and the radiation belt boundaries as observed by the instruments CIS, RAPID, and WHISPER onboard Cluster. *Journal of Geophysical Research: Space Physics*, 2013.

T. N. Davis and M. Sugiura. Auroral electrojet activity index ae and its universal time variations. *Journal of Geophysical Research*, 71(3):785–801, 1966. doi: 10.1029/JZ071i003p00785. URL https://agupubs.onlinelibrary.wiley.com/doi/abs/10.1029/JZ071i003p00785.

D. Evans, H. Garrett, I. Jun, R. Evans, and J. Chow. Long-term observations of the trapped high-energy proton population (L 4) by the NOAA Polar Orbiting Environmental Satellites (POES). *Advances in Space Research*, 41:1261–1268, 2008. doi: 10.1016/j.asr.2007.11.028.

J. A. Fennelly, W. R. Johnston, D. M. Ober, G. R. Wilson, T. P. O'Brien, and S. L. Huston. South Atlantic Anomaly and CubeSat design considerations, 2015. URL https://doi.org/10.1117/12.2190595.

S. F. Fung, X. Shao, and L. C. Tan. Long-term variations of the electron slot region and global radiation belt structure. *Geophysical Research Letters*, 33(4), 2006. doi: 10.1029/2005GL024891. URL https://agupubs.onlinelibrary.wiley.com/doi/abs/10.1029/2005GL024891.

G. P. Ginet, T. P. O'Brien, S. L. Huston, W. R. Johnston, T. B. Guild, R. Friedel, C. D. Lindstrom, C. J. Roth, P. Whelan, R. A. Quinn, D. Madden, S. Morley, and Yi-Jiun Su. AE9, AP9 and SPM: New models for specifying the trapped energetic particle and space plasma environment. *Space Science Reviews*, 179(1):579–615, Nov 2013. ISSN 1572-9672. doi: 10.1007/s11214-013-9964-y. URL https://doi.org/10.1007/s11214-013-9964-y.

S. A. Glauert and R. B. Horne. Calculation of pitch angle and energy diffusion coefficients with the PADIE code. *Journal of Geophysical Research: Space Physics*, 110(A4), 2004. doi: 10.1029/2004JA010851. URL https://agupubs.onlinelibrary.wiley.com/doi/abs/10.1029/2004JA010851.

S. A. Glauert, R. B. Horne, and N. P. Meredith. Three-dimensional electron radiation belt simulations using the bas radiation belt model with new diffusion models for chorus, plasmaspheric hiss, and lightning-generated whistlers. *Journal of Geophysical Research: Space Physics*, 119(1):268–289, 2014. doi: 10.1002/2013JA019281. URL https://agupubs.onlinelibrary.wiley.com/doi/abs/10.1002/2013JA019281.

S. J. Goodman, T. J. Schmit, J. Daniels, W. Denig, and K. Metcalf. 1.05 - GOES: Past, Present, and Future. In *Comprehensive Remote Sensing*, pages 119 – 149. Elsevier, Oxford, 2018. ISBN 978-0-12-803221-3. doi: https://doi.org/10.1016/B978-0-12-409548-9.10315-X. URL http://www.sciencedirect.com/science/article/pii/B978012409548910315X.

W. N. Hess. *The radiation belt and magnetosphere*. Blaisdell Publishing company, 1968.

D. Heynderickx. Comparison between methods to compensate for the secular motion of the South Atlantic anomaly. *Radiation Measurements*, 26:369–373, May 1996. doi: 10.1016/1350-4487(96)00056-X.

D. Heynderickx, M. Kruglanski, V. Pierrard, J. Lemaire, M. D. Looper, and J. B. Blake. A low altitude trapped proton model for solar minimum conditions based on SAMPEX/PET data. *IEEE Transactions on Nuclear Science*, 46:1475–1480, December 1999. doi: 10.1109/23.819110.

R. B. Horne. Plasma astrophysics: Acceleration of killer electrons. *Nature Physics*, 3:590–591, September 2007. doi: 10.1038/nphys703.

R. B. Horne, S. A. Glauert, N. P. Meredith, D. Boscher, V. Maget, D. Heynderickx, and D. Pitchford. Space weather impacts on satellites and forecasting the Earth's electron radiation belts with SPACECAST. *Space Weather*, 11(4):169–186, April 2013. ISSN 1542-7390. doi: 10.1002/swe.20023.

M. K. Hudson, V. A. Marchenko, I. Roth, M. Temerin, J. B. Blake, and M. S. Gussenhoven. Radiation belt formation during storm sudden commencements and loss during main phase. *Advances in Space Research*, 21:597–607, 1998. doi: 10.1016/S0273-1177(97)00969-1.

M. B. Kallenrode. *Space Physics*. Advanced Texts in Physics. Springer-Verlag Berlin Heidelberg, 2 edition, 2001. doi: 10.1007/978-3-662-04443-8.

M. G. Kivelson and C. T. Russell. *Introduction to Space Physics*. Cambridge University Press, United Kingdom, 1995. ISBN 9780521457149.

M. Kruglanski. Engineering tool for trapped proton flux anisotropy evaluation. *Radiation Measurements*, 26:953–958, November 1996. doi: 10.1016/S1350-4487(96)00097-2.

M. Kruglanski. TREND: Trapped Radiantion Environment Model Development. . Technical report, BIRA-IASB, 1998.

M. Kruglanski and J. Lemaire. Trapped Proton Modelling at Low Altitude, Technical note 6 for ESTEC contract no. 10725/94/JG(SC). 1996.

J. F. Lemaire. From the discovery of radiation belts to space weather perspectives. In I. A. Daglis, editor, *Space*

Storms and Space Weather Hazards, volume 38 of *NATO Science Series*, chapter 3. 2001. doi: https://doi.org/10.1007/978-94-010-0983-6_3.

J. F. Lemaire, D. Heynderickx, and D.N. Baker, editors. *Radiation Belts: Models and Standards*, volume 97. American Geophysical Union (AGU), 1996. ISBN 9780875900797. doi: 10.1029/GM097. URL https://agupubs.onlinelibrary.wiley.com/doi/book/10.1029/GM097.

X. Li, D. N. Baker, T. P. O'Brien, L. Xie, and Q. G. Zong. Correlation between the inner edge of outer radiation belt electrons and the innermost plasmapause location. *Geophysical Research Letters*, 33(14), 2006. doi: 10.1029/2006GL026294. URL https://agupubs.onlinelibrary.wiley.com/doi/abs/10.1029/2006GL026294.

X. Li, R. S. Selesnick, D. N. Baker, A. N. Jaynes, S. G. Kanekal, Q. Schiller, L. Blum, J. Fennell, and J. B. Blake. Upper limit on the inner radiation belt MeV electron intensity. *Journal of Geophysical Research: Space Physics*, 120(2):1215–1228, 2015. doi: 10.1002/2014JA020777. URL https://agupubs.onlinelibrary.wiley.com/doi/abs/10.1002/2014JA020777.

X. Li, R. Selesnick, Q. Schiller, K. Zhang, H. Zhao, D. Baker, and M. Temerin. Measurement of electrons from albedo neutron decay and neutron density in near-Earth space. *Nature*, 2017.

M. D. Looper, J. B. Blake, R. A. Mewaldt, J. R. Cummings, and D. N. Baker. Observations of the remnants of the ultrarelativistic electrons injected by the strong SSC of 24 March 1991. *Geophysical Research Letters*, 21(19):2079–2082, 1994. doi: 10.1029/94GL01586. URL https://agupubs.onlinelibrary.wiley.com/doi/abs/10.1029/94GL01586.

M. D. Looper, J. B. Blake, and R. A. Mewaldt. Response of the inner radiation belt to the violent sun-earth connection events

of october–november 2003. *Geophysical Research Letters*, 32(3), 2005. doi: 10.1029/2004GL021502. URL https://agupubs.onlinelibrary.wiley.com/doi/abs/10.1029/2004GL021502.

G. López Rosson and V. Pierrard. Analysis of proton and electron spectra observed by EPT/PROBA-V in the south atlantic anomaly. *Advances in Space Research*, 60(4):796 – 805, 2017. ISSN 0273-1177. doi: http://dx.doi.org/10.1016/j.asr.2017.03.022. URL http://www.sciencedirect.com/science/article/pii/S0273117717302107.

L. R. Lyons and R. M. Thorne. Equilibrium structure of radiation belt electrons. *Journal of Geophysical Research*, 78(13):2142–2149, 1973. doi: 10.1029/JA078i013p02142. URL https://agupubs.onlinelibrary.wiley.com/doi/abs/10.1029/JA078i013p02142.

L. R. Lyons, R. M. Thorne, and C. F. Kennel. Pitch-angle diffusion of radiation belt electrons within the plasmasphere. *Journal of Geophysical Research*, 77(19):3455–3474, 1972. doi: 10.1029/JA077i019p03455. URL https://agupubs.onlinelibrary.wiley.com/doi/abs/10.1029/JA077i019p03455.

C. E. McIlwain. Coordinates for Mapping the Distribution of Magnetically Trapped Particles. *Journal of Geophysical Research*, 66:3681–3691, November 1961. doi: 10.1029/JZ066i011p03681.

C. E. McIlwain. Magnetic Coordinates. *Space Science Reviews*, 5:585–598, August 1966. doi: 10.1007/BF00167327.

J. D. Meffert and M. S. Gussenhoven. CRRESPRO documentation, PL-TR-94-2218. *Environmental Research Papers*, 1158, 1994.

N. P. Meredith, R. B. Horne, S. A. Glauert, and R. R. Anderson. Slot region electron loss timescales due to plasmaspheric hiss and lightning-generated whistlers. *Journal of Geophysical Research: Space Physics*, 112(A8), 2007. doi: 10.1029/

2007JA012413. URL https://agupubs.onlinelibrary.wiley.com/doi/abs/10.1029/2007JA012413.

R. M. Millan and D. N. Baker. Acceleration of Particles to High Energies in Earth's Radiation Belts. *Space Science Review*, 173: 103–131, November 2012. doi: 10.1007/s11214-012-9941-x.

T. Murayama and J. A. Simpson. Electrons within the neutral sheet of the magnetospheric tail. *Journal of Geophysical Research*, 73(3):891–905, 1968. ISSN 2156-2202. doi: 10.1029/JA073i003p00891. URL http://dx.doi.org/10.1029/JA073i003p00891.

NASA. NOAA-N prime: the final TIROS mission. URL https://poes.gsfc.nasa.gov/images/298662main_NOAA-N%20Prime%20Booklet%2012-16-08.pdf.

NASA. Radiation Belt Storm Probes Launch press kit, August 2012. URL https://www.nasa.gov/pdf/677837main_rbsp_pk_final81712_lores.pdf.

T. G. Northrop. Adiabatic charged-particle motion. *Reviews of Geophysics*, 1(3):283–304, 1963. doi: 10.1029/RG001i003p00283. URL https://agupubs.onlinelibrary.wiley.com/doi/abs/10.1029/RG001i003p00283.

T. G. Northrop and E. Teller. Stability of the adiabatic motion of charged particles in the Earth's field. *Phys. Rev.*, 117:215–225, Jan 1960. doi: 10.1103/PhysRev.117.215. URL https://link.aps.org/doi/10.1103/PhysRev.117.215.

T. P. O'Brien and M. B. Moldwin. Empirical plasmapause models from magnetic indices. *Geophysical Research Letters*, 30(4), 2003. doi: 10.1029/2002GL016007. URL https://agupubs.onlinelibrary.wiley.com/doi/abs/10.1029/2002GL016007.

T. P. O'Brien, W. R. Johnston, S. L. Huston, C. J. Roth, T. B. Guild, Y. . Su, and R. A. Quinn. Changes in ae9/ap9-irene version 1.5. *IEEE Transactions on Nuclear Science*, 65(1):462–466, Jan 2018. ISSN 0018-9499. doi: 10.1109/TNS.2017.2771324.

W. P. Olson and K. A. Pfitzer. A quantitative model of the magnetospheric magnetic field. , 79:3739, 1974. doi: 10.1029/JA079i025p03739.

V. Pierrard. *L'environnement Spatial de la Terre*. Presses Universitaires de Louvain, 2009. ISBN 978-2-87463-195-5.

V. Pierrard and S. Benck. The dynamics of the terrestrial radiation belts and its links to the plasmasphere. *AIP Conference Proceedings*, 1500(1):216–221, 2012. doi: 10.1063/1.4768769. URL https://aip.scitation.org/doi/abs/10.1063/1.4768769.

V. Pierrard and K. Borremans. Fitting the AP-8 spectra to determine the proton momentum distribution functions in space radiations. *Radiation Measurements*, 47(6):401 – 405, 2012. ISSN 1350-4487. doi: https://doi.org/10.1016/j.radmeas.2012.04.002. URL http://www.sciencedirect.com/science/article/pii/S1350448712001114.

V. Pierrard and J. Lemaire. Fitting the AE-8 energy spectra with two maxwellian functions. *Radiation Measurements*, 26 (3):333 – 337, 1996. ISSN 1350-4487. doi: https://doi.org/10.1016/1350-4487(96)00057-1. URL http://www.sciencedirect.com/science/article/pii/1350448796000571. Space Radiation Environment: Empirical And Physical Models.

V. Pierrard and G. López Rosson. The effects of the big storm events in the first half of 2015 on the radiation belts observed by EPT/PROBA-V. *Annales Geophysicae*, 34(1):75–84, 2016. doi: 10.5194/angeo-34-75-2016. URL https://www.ann-geophys.net/34/75/2016/.

V. Pierrard, J. Lemaire, D. Heynderickx, M. Kruglanski, M. Looper, B. Blake, and D. Mewaldt. Statistical analysis of SAMPEX PET proton measurements. *Nuclear Instruments and Methods in Physics Research A*, 449:378–382, July 2000. doi: 10.1016/S0168-9002(99)01454-0.

V. Pierrard, G. López Rosson, K. Borremans, J. Lemaire, J. Maes, S. Bonnewijn, E. Van Ransbeeck, E. Neefs, M. Cyamukungu, S. Benck, L. Bonnet, S. Borisov, J. Cabrera, G. Grégoire, C. Semaille, G. Creve, J. De Saedeleer, B. Desoete, F. Preud'homme, M. Anciaux, A. Helderweirt, K. Litefti, N. Brun, D. Pauwels, C. Quevrin, D. Moreau, R. Punkkinen, E. Valtonen, W. Hajdas, and P. Nieminen. The Energetic Particle Telescope: First Results. , 184:87–106, November 2014. doi: 10.1007/s11214-014-0097-8.

G. D. Reeves, K. L. McAdams, R. H. W. Friedel, and T. P. O'Brien. Acceleration and loss of relativistic electrons during geomagnetic storms. *Geophysical Research Letters*, 30(10), 2003. doi: 10.1029/2002GL016513. URL `https://agupubs.onlinelibrary.wiley.com/doi/abs/10.1029/2002GL016513`.

J. F. Ripoll, Y. Chen, J. F. Fennell, and R. H. W. Friedel. On long decays of electrons in the vicinity of the slot region observed by HEO3. *Journal of Geophysical Research: Space Physics*, 120(1):460–478, 2014. doi: 10.1002/2014JA020449. URL `https://agupubs.onlinelibrary.wiley.com/doi/abs/10.1002/2014JA020449`.

J.-A. Sauvaud, R. Maggiolo, C. Jacquey, M. Parrot, J.-J. Berthelier, R. J. Gamble, and Craig J. Rodger. Radiation belt electron precipitation due to VLF transmitters: Satellite observations. *Geophysical Research Letters*, 35(9), 2008.

J.-A. Sauvaud, M. Walt, D. Delcourt, C. Benoist, E. Penou, Y. Chen, and C. T. Russell. Inner radiation belt particle acceleration and energy structuring by drift resonance with ULF

waves during geomagnetic storms. *Journal of Geophysical Research: Space Physics*, 2013.

D. Sawyer and J. I. Vette. AP-8 trapped proton environment for solar maximum and solar minimum. *National Space Science Data Center, Report 76-06*, 1976.

Y. Y. Shprits, S. R. Elkington, N. P. Meredith, and D. A. Subbotin. Review of modeling of losses and sources of relativistic electrons in the outer radiation belt I: Radial transport. *Journal of Atmospheric and Solar-Terrestrial Physics*, 70(14):1679 – 1693, 2008a. ISSN 1364-6826. doi: https://doi.org/10.1016/j.jastp.2008.06.008. URL http://www.sciencedirect.com/science/article/pii/S1364682608001648.

Y. Y. Shprits, D. A. Subbotin, N. P. Meredith, and S. R. Elkington. Review of modeling of losses and sources of relativistic electrons in the outer radiation belt II: Local acceleration and loss. *Journal of Atmospheric and Solar-Terrestrial Physics*, 70 (14):1694 – 1713, 2008b. ISSN 1364-6826. doi: https://doi.org/10.1016/j.jastp.2008.06.014. URL http://www.sciencedirect.com/science/article/pii/S1364682608001673.

Y. Y. Shprits, D. Subbotin, A. Drozdov, M. E. Usanova, A. Kellerman, K. Orlova, D. N. Baker, D. L. Turner, and K. C. Kim. Unusual stable trapping of the ultrarelativistic electrons in the Van Allen radiation belts. *Nature Physics*, 9:699–703, November 2013. doi: 10.1038/nphys2760.

W. N. Spjeldvik and P. L. Rothwell. The radiation belts. In A. Jursa, editor, *Handbook of Geophysics and the Space Environment*, chapter 5, pages 5–1– 5–55. Air Force Geophysics Laboratory, 1985.

R. M. Thorne. Radiation belt dynamics: The importance of wave-particle interactions. *Geophysical Research Letters*, 37(22),

2010. doi: 10.1029/2010GL044990. URL https://agupubs.onlinelibrary.wiley.com/doi/abs/10.1029/2010GL044990.

D. L. Turner, Y. Shprits, M. Hartinger, and V. Angelopoulos. Explaining sudden losses of outer radiation belt electrons during geomagnetic storms. *Nature Physics*, 8:208–212, March 2012. doi: 10.1038/nphys2185.

A. L. Vampola. VLF transmission induced slot electron precipitation. *Geophysical Research Letters*, 4(12): 569–572, 1977. doi: 10.1029/GL004i012p00569. URL https://agupubs.onlinelibrary.wiley.com/doi/abs/10.1029/GL004i012p00569.

A. L. Vampola and A. Korth. Electron drift echoes in the inner magnetosphere. *Geophysical Research Letters*, 19(6):625–628, 1992. doi: 10.1029/92GL00121. URL https://agupubs.onlinelibrary.wiley.com/doi/abs/10.1029/92GL00121.

J. I. Vette. The AE-8 trapped electron model environment. *NASA STI/Recon Technical Report N*, 92, November 1991.